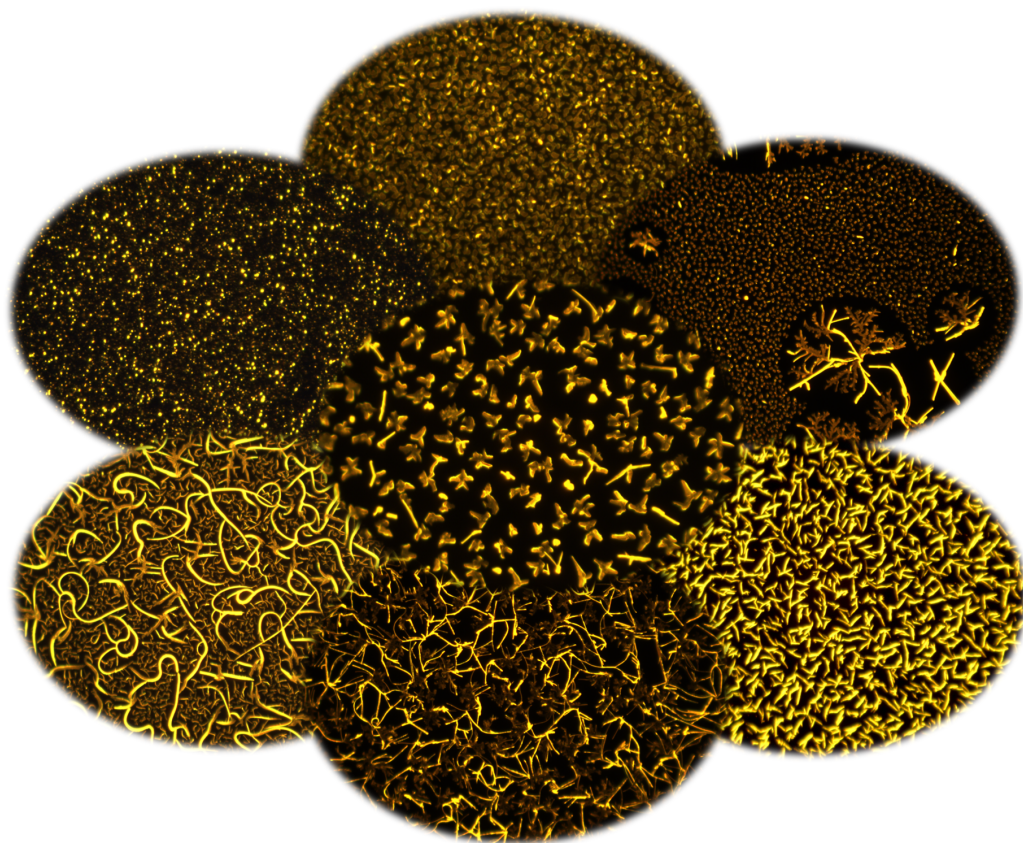


Nano Structured Devices for Energy Generation

Ph.D. Thesis
Mads Clausen Institute
University of Southern Denmark



Michał Jędrzej Radziwon

July 29. 2013

Preface

This thesis is submitted as a prerequisite for achieving a Ph.D. degree at the University of Southern Denmark. The majority of research described here was conducted at NanoSYD center of Mads Clausen Institute. The Ph.D. project was supervised by Professor Horst-Günter Rubahn as a main supervisor and Morten Madsen as project supervisor. Apart from this thesis, a number of other publications has also been made during the duration of this project, which are listed in chapter Publications on page 97.

I would like to acknowledge several people for their support during this project. First of all the special thanks goes to Professor Horst-Günter Rubahn, who invited me to NanoSYD group, shared his knowledge, and was the main supervisor, as well as to Morten Madsen the project supervisor. James Hoyland was always there to answer all questions, that is why I thank him for countless inspirations and discussions. Frank Balzer has helped me a lot in experiments, shared good advices, and had a patience for answering all my questions, especially those silly ones. The support and optics advices provided by Jacek Fiutowski were a great help during the project.

I would like to acknowledge also technical and administrative staff, especially Mogens Petersen, Reiner Hübel, Ian Wozniacki, and Zora Milde, who made my work a lot easier. Moreover, I thank my fellow PhD students for sharing good and bad times in the office, in the lab, and outside.

Besides my work done in NanoSYD group in Sønderborg, I have also had a pleasure to visit the Institute of Solid State Physics at Graz University of Technology to preform a part of the experiments. I would like to thank Roland Resel, and his team for fruitful collaboration. Moreover, I would like also to thank my teachers: Jan Masny, Marian

Bąk and Krzysztof Tchoń who have kindled and maintained my passion for science.

This thesis would not be completed without support, motivation and encouragement from my beloved wife Agnieszka Radziwon.

Michał Jędrzej Radziwon

Abstract

This work focuses on the enhancement of α -sexithiophene / buckminsterfullerene (α 6T / C_{60}) inverted bilayer organic solar cell efficiency by the introduction of crystalline nanostructures in the electron donor layer. In order to utilize the charge carrier mobility anisotropy in crystalline α -6T structures in solar cells, the orientation of the individual molecules should favor charge transport perpendicular to the substrate plane. Such orientation is realized from α -6T molecules lying on the substrate, which additionally infers the preferred orientation of the transition dipole for maximal light absorption.

In this work, an organic molecular beam deposition (OMBD) system was used for studies on growth of α -6T crystalline formations directly on C_{60} thin-films. For that, a dedicated, 3-source (α -6T, C_{60} , bathocuproine (BCP)), high vacuum OMBD system has been designed and assembled. The source temperatures and a shutter were controlled by the supervisory control and data acquisition (SCADA) system, which has been implemented in LabVIEW environment. The temperatures, process pressure, and deposition rate were stored for future analysis.

By variation of the substrate temperature during deposition, different structures have been obtained ranging from a rough film, through individual clusters, a dense mesh of elongated islands, fiber like- and dendritic structures, polygonal mono-crystallites, to long curly fibers. The molecular packing in those formations has been investigated with usage of epifluorescence polarimetry and X-ray diffractometry (XRD).

Layer thicknesses of inverted α -6T / C_{60} bilayer organic solar cells fabricated at room temperature were optimized to obtain the model device for the performance enhancement studies. By variation of the substrate temperature during deposition of α -6T, the structures identified in the preceding study were introduced into solar cell devices. Using power conversion efficiency as a figure of merit, a 100% performance enhancement has been reported for devices fabricated within 10°C substrate temperature window. The enhancement was due to peaks in short circuit current density

and fill factor, which were obtained when fiber-like structures consisting of lying α -6T molecules were present. Such molecular packing agrees with a favorable molecular orientation for maximal charge carrier mobility in solar cell applications.

A solar cell characterization station has been designed and build including a solution for reliable connection of an examined device to the measurement equipment. The measurement of the illumination beam profile has revealed a strong nonuniformity which led to the integration of a translational stage, which assures 1 sun illumination during device characterization. The characterization process was controlled by SCADA system implemented in LabVIEW.

Dansk Resume

I dette arbejde fokuseres der på at øge effektiviteten af α -6T / C₆₀ (alpha -sexithiophene / buckminsterfullerene) inverterede tolags organiske solceller ved at introducere krystallinske nanostrukturer i elektron donorlaget. For at udnytte den anisotropiske ladningsbærer-mobilitet i de krystallinske α -6T strukturer i solcellen skal orienteringen af de individuelle molekyler favorisere ladningstransport vinkelret på substratet. Denne orientering er realiseret når α -6T molekylerne ligger fladt på substratet, hvilket ydermere giver den foretrukne orientering af overgangs-dipolen for maksimal lysabsorption.

I dette arbejde bliver et "organisk molekylær stråle deponeringssystem" (OMBD) brugt til at studere væksten af krystallinske α -6T formationer direkte på C₆₀ tyndfilm. For at muliggøre dette er et dedikeret 3-kilde (α -6T, C₆₀, BCP), højvakuum system blevet designet og bygget. Fordampningstemperatur og mekanisk blænde kontrolleres af et overvågnings og dataopsamlings system (SCADA), som er blevet implementeret i LabVIEW. Temperatur, procestryk og deponeringsrate bliver gemt for yderligere analyse.

Ved at variere substrattemperaturen under fordampning kan forskellige strukturer opnås, fra en ru film, individuelle molekylære klynger, et tæt net af aflange øer, fibre- og dendritrisk-lignende strukturer, mangedannede mono-krystalitter, til lange bøjede fibre. Den molekylære pakning i disse formationer er blevet undersøgt ved brug af epifluorescens polarimetri og røntgen diffraktometri (XRD).

Lagtykkelsen af inverterede α -6T/C₆₀ tolags solceller fabrikeret ved stuetemperatur er blevet optimeret for at fremstille en model-celle som kan bruges til effektivitetsstudier. Ved at variere substrattemperaturen under deponering af α -6T, er de tidligere identificerede strukturer blevet introduceret i solceller. Ved at benytte nyttevirkningen som en målestandard er en 100% forøgelse blevet rapporteret for celler fremstillet indenfor et 10°C substrattemperatur-vindue. Forøgelsen skyldes toppunkter i kortslutningsstrømtætheden og fill-faktoren, som blev opnået når fiber-lignende strukturer bestående

af liggende α -6T molekyler var til stede. Pakningen af disse molekyler favoriserer en molekulær orientering som giver maksimal ladningsbærer-mobilitet i solcelle-applikationer.

En målestation til karakterisering af solceller er blevet designet og fremstillet og inkluderer en løsning til pålideligt at forbinde de undersøgte celler til måleudstyret. Undersøgelse af belysningsprofilen har afsløret betragtelige variationer, hvilket har resulteret i integration af en translationel platform, som sikrer ensformig solbelysning under karakteriseringen. Karakteriseringens-processen bliver også kontrolleret af et SCADA system implementeret i LabVIEW.

Contents

Preface	I
Abstract	III
Dansk resume	V
1 Introduction	1
1.1 Rationale	1
1.2 Organic Solar Cells	3
1.2.1 Organic vs. Inorganic Solar Cell	3
1.2.2 Organic materials	5
1.2.3 Basic processes in organic solar cell	9
Light absorption and exciton generation	10
Exciton diffusion	12
Charge separation	13
Charge transport	15
Charge collection	16
Loss mechanisms	16
1.2.4 Types of Organic Solar Cells	18
Single layer solar cells	18
Dye-sensitized solar cells	19
Planar heterojunction organic solar cells	20
Bulk heterojunction solar cells	21
1.2.5 Configurations of solar cells	22
1.3 Crystallinity influence on solar cell performance	23
1.3.1 Growth of organic nanostructures	23

1.4	Implementation of α -sexithiophene nanostructures in solar cells	26
1.5	Solar cell characterization	27
	J-V curve	27
	Open circuit voltage	29
	Short circuit current density	29
	Fill factor	30
	PCE	30
2	Experimental	33
2.1	Device layout design	33
	2.1.1 Electrodes	35
	2.1.2 Active layers	36
	2.1.3 Top electrode	36
	2.1.4 Encapsulation	38
2.2	Fabrication process	39
	2.2.1 Substrate preparation	39
	Photolithography	39
	Metal layers deposition	40
	Dicing	40
	Oxidation of titanium layer	40
	2.2.2 Organic molecular beam deposition	41
	Vacuum system	41
	Deposition process	45
	2.2.3 Spin-coating	46
	Defining device area	46
	Spin-coating of PEDOT:PSS blend	46
	Encapsulation	47
2.3	Characterization	48
	2.3.1 Photovoltaic measurement setup	48
	Solar simulator	48
	Source meter	50
	Test cradle	51
	Software	51

	Measurement	52
	Data processing	53
2.3.2	Epifluorescence imaging	53
2.3.3	Epifluorescence polarimetry	54
2.3.4	X-ray diffractometry	56
2.3.5	Atomic Force Microscopy	57
2.4	Experiments	58
2.4.1	Growth of α -sexithiophene nanostructures	58
	C_{60} temperature independence	59
	α -sexithiophene material validation	59
	α -sexithiophene nanostructures vs. temperature	59
2.4.2	Implementation of α -sexithiophene nanostructures in solar cells	60
	α -sexithiophene nanostructures integration with spin-coating	60
	Solar cell performance vs. deposition temperature	60
3	Results	61
3.1	Growth of α -sexithiophene nanostructures	61
3.1.1	C_{60} temperature independence	61
	Summary	62
3.1.2	α -sexithiophene material validation	62
3.1.3	Morphological studies	63
	30nm α -6T on C_{60} layers	64
	100nm α -6T on C_{60} layers	70
	Summary	77
3.1.4	Crystallography studies	77
	Fluorescence polarimetry.	78
	X-ray diffractometry	79
	Summary	80
3.2	Implementation of nanostructures	81
3.2.1	α -sexithiophene nanostructure integration with spin-coating	81
	Summary	82
3.2.2	Optimization of bilayer device	83
	C_{60} layer	83

	α -sexithiophene layer	84
	Summary	85
3.2.3	TiO _x photo conductivity	86
	Summary	87
3.2.4	Solar cell performance vs. deposition temperature	87
	Summary	90
4	Conclusions	91
4.1	Hardware	91
4.2	Growth of α -sexithiophene structures on C ₆₀	92
4.3	Crystal enhanced organic solar cells	92
5	Outlook	94
5.1	Improvements	94
5.1.1	Optimization of device at elevated temperature	94
5.1.2	OMBD system	94
5.1.3	Encapsulation	95
5.2	Further research	95
5.2.1	Multistage deposition	95
5.2.2	lamellar growth of α -sexithiophene	96
5.2.3	In-situ growth monitoring	96
	Publications	97
	Reviewed publications	97
	Oral presentations	97
	Conference abstracts	98
	Conference posters	98
	Authorship agreements	101
	Manuscripts of submitted publications	109
	Bibliography	127

1 Introduction

1.1 Rationale

Limited fossil fuel resources, together with anthropogenic climate changes underline the necessity for research in and use of renewable energies. It has been expressed, among others, by the number of projects launched in European Union countries which aim for renewables parity; e.g. Germany aims to obtain 25%-30% of electrical power production from renewables until 2020, the majority of which is to be photovoltaic[1]. Similar trends are observed globally, which induces substantial growth of photovoltaic market [2, 3]. Growth of the worldwide demand for electric power is a result of increase in consumption by single users, as well as of a developing industrialization in the rapidly expanding economies of the BRIC countries[4]. Various attempts have been made to estimate future trends of electric power consumption [5, 6, 7] which concluded that by year 2050, the total power of installed power plants worldwide needs to increase by 15-20TW[8].

The environmental impact of power generation is not to be overlooked, as is responsible for the major part of CO₂ emission[9]. Due to the strong influence of CO₂ over the climate, the studies have been made to predict the amount energy produced without greenhouse effect gasses emission required to maintain stable concentration of CO₂ in the atmosphere[10]. It yields to the requirement of 10-15TW of carbon-free power generation in 2050 in order to keep the CO₂ level below 750 ppm (today the concentration equals 396.80ppm[11]). That gives a rise to required growth factor of installed power in order of 1GW per day! It is a tremendous value, and scalability considerations need to be made to type the potential technologies which could withstand this demand.

Another two important factors include the abundance of the elements used in energy generation and energy payback time (EPBT) of energy generating devices. All of above mentioned requirements are clearly not met by hydroelectric (1.2TW available - not

scalable), geothermal (1.9TW), biomass (5-7TW), or wind (14TW - high EPBT and slow scalability), but it is also not easy for conventional photovoltaic technology, even if technically ca. 10 000 TW is accessible. Low abundance of the elements used in production of traditional solar cells - Ge, Se and Ga, together with processing requiring high temperatures leading to EPBT in the range of 1-2 years does not legitimate conventional photovoltaic technologies to solve the 1GW/day problem.

Even though hydro-power was a leading renewable energy source for the past century, wind turbines and photovoltaics have exhibited a strong increase in the last decade. Photovoltaics still provide only a small fraction of the world's energy, but due to governmental policies and technological advances, it has increased its capacity over 60 times since year 2000 and just surpassed 100GW of installed capacity in the end of 2012[12].

It is generally accepted that photovoltaic technology is the best way to convert the solar energy to electricity as it incorporates no moving parts, is silent, and requires little-, to no maintenance. However, due to the high price, large energy budget, slow production or employment of rare elements, only two technologies are able to address 1GW/day problem: silicon based solar cells and organic solar cells[13]. The organic solar cells have several advantages over the silicon ones: low thermal budget leading to short EPBT[13], manufacturing possibilities in high yield on flexible substrates, and due to the higher absorption of sunlight - active layers can be as thin as few tens of nanometers. This technology has also several drawbacks: conversion efficiencies are substantially lower (12% in best laboratory cells[14] and 1.5-2.5% in mass produced[15]), and lifetimes reach only few thousands of hours[16, 17]. Although, the organic photovoltaics cannot be considered as mature technology, it has the steepest learning curve of all photovoltaic technologies[18].

One class of the organic photovoltaic are small molecule solar cells. Those devices incorporate light (<800nm) organic molecules, which form strong conjugated systems [17, 8]. As NanoSYD center has a great expertise in growth and analysis of nanostructures from such compounds[19, 20, 21, 22, 23, 24], the project has been launched to investigate the influence of nanostructured morphology of donor-acceptor interface on the performance of solar cell.

1.2 Organic Solar Cells

The first solar cell was examined and presented to scientific audience by E. Becquerel as early as in 1839[25], but it took over 60 years to find scientifically pleasing explanation of this phenomenon[26], for which A. Einstein was honored with Nobel Prize in 1921. The first practical solar cell was invented in Bell Laboratories in 1954 by Daryl Chapin, Calvin Souther Fuller and Gerald Pearson, and was commercialized in 1960's for use in space programs. Since then, solar cells have been extensively studied for subsequent decades rising the efficiency of a triple junction device to 44.4% in world record cell developed in SHARP laboratories[27].

Organic photovoltaics is still novel and immature technology, which started to be extensively studied since the early 90's. This is one of the reasons why the performance of organic solar cells is not so spectacular yet, but not the sole one.

1.2.1 Organic vs. Inorganic Solar Cell

The fundamental difference between organic photovoltaic (OPV) and inorganic photovoltaic (IPV) lays in the physical processes which occur immediately after absorption of the photon. In IPV, a pair of free charges - hole and electron - is generated, while in OPV a strongly bound exciton is formed[28, 17]. An exciton in a semiconducting organic material can be considered as an excited, mobile, electrically neutral electron-hole pair tightly bound by Coulombic force.

The reason for this difference is principally due to the fact that, the dielectric constant is significantly lower in organic materials (typically $\epsilon = 4$) than in inorganic ($\epsilon = 13$ for silicon)[29]. Therefore, even though for inorganic materials the electron wave function, which can be approximated by the Bohr radius of an electron-hole pair r_b , extends beyond the frontier of a Coulombic potential well at the room temperature - r_c , for organic materials, an excited state is still localized within electrostatic potential well (see figure 1.1). Excited electron-hole pair can be described as Frenkel exciton in case it habitats one molecule, or as charge-transfer exciton if electron and hole are on separate molecules. In order to dissociate the Frenkel exciton into a pair of free charges, additional energy is needed to be applied to excess the coulomb binding energy.

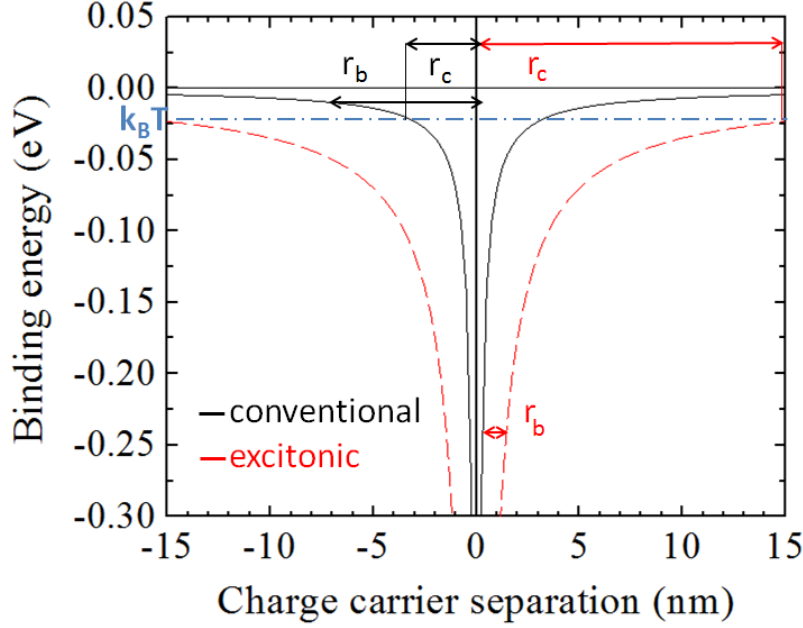


Figure 1.1: The Coulomb potential of an electron-hole pair for two dielectric constants: $\epsilon = 3$ (typical for organic semiconductors), and $\epsilon = 15$ (typical for inorganic semiconductors). For both cases, the values Bohr radius (r_b) and radius of Coulomb potential well at $k_B T$ (r_c) are shown. (adopted from [17])

Such an energy surplus can appear on the interface of two materials which differ in electron donating and accepting properties. If the band offset between the materials is greater than the binding energy of exciton, dissociation will occur resulting in a free electron in acceptor, and a free hole in donor material. The diagram of this process is presented in figure 1.9.

Such a process of separating hole - electron pair leads to the next major difference between IPV and OPV. In IPV solar cells free charges are generated in the whole bulk of the device, therefore both the majority and minority carrier appear at the same side of the interface. Contrary, in OPV devices, the free charges appear only at the respective sides of the interface of donor and acceptor materials. Taking into consideration commonly low carrier densities in organic materials, OPV solar cells are predominantly majority carrier devices, unlike most of IPV devices which are minority carrier devices[30].

Another remarkable difference is the fact, that in inorganic semiconductor with 3D crystal lattice, the valence and conduction levels of individual atoms form conduction and valence bands across the whole lattice, while in organic materials the intermolecular forces are too weak to form extensive 3D crystals and continuous bands are not being formed. Unlike in inorganic semiconductors, electrons are not concerned as orbiting the nuclei, but rather as occupying the whole molecular orbital. Therefore, the important energy levels are not defined as valence band, where all of electrons reside when matter is at 0K temperature, and conduction band, where electrons can move freely within atomic lattice, but as highest occupied molecular orbital (HOMO) and lowest unoccupied molecular orbital (LUMO) instead. Due to before mentioned weak interactions, the charge transport in organic semiconductors proceeds by hopping between localized sites rather than through continuous electronic band[31].

1.2.2 Organic materials

Natural photosynthesis is the primary model to follow in case of sunlight harvesting, where most commonly chlorophyl molecule absorbs photons which energy is converted into chemical energy. Despite its rather poor performance, chlorophyl pigments were indeed used to fabricate working solar cell[32]. But chlorophyl's function in plants is to stimulate a red-ox reaction rather than provide separate charges. Therefore, other materials are applied in organic solar cells. The materials which are to be considered in organic solar cells must provide three basic features:

- absorb incoming photons,
- convert photons into photo-generated free carriers,
- and be able to extract free carriers from the bulk of the active region to the electrodes.

Moreover, the implementation of the material is not of lesser importance, therefore chosen materials should be applicable to the substrate by commonly used techniques such as: organic molecular beam deposition (OMBD)[33], vacuum thermal evaporation (VTE)[33] and organic vapor phase deposition (OVPD)[34] for small molecule materials, while for soluble molecules and polymers: casting[35], roll-2-roll printing[36, 37] or screen printing[38].

Before mentioned properties are commonly found in materials with extended delocalized π systems. Most studied organic semiconductors can be considered as wide band gap (1.4eV - 3eV) semiconductors, with low intrinsic concentration of free carriers at dark conditions. Exemplary chemical compounds commonly used in organic photovoltaics are presented in figure 1.2. All of them are subject to synthesis chem-

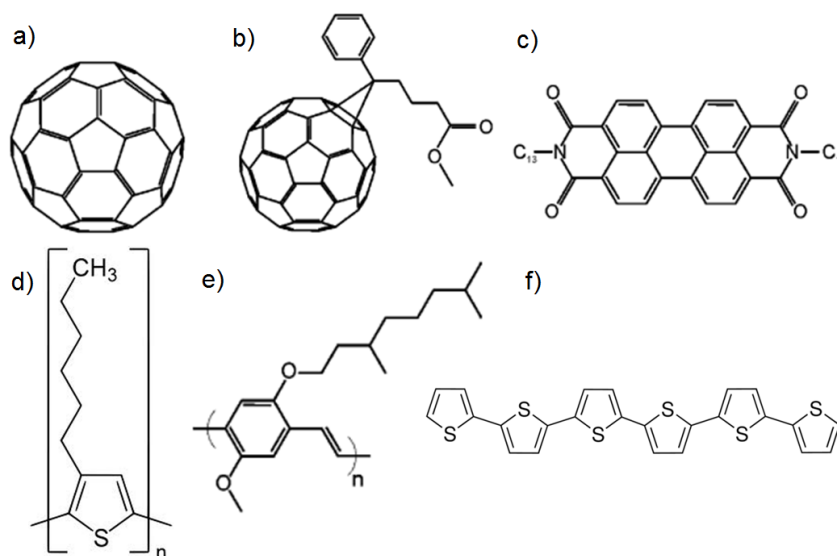


Figure 1.2: Exemplary organic semiconductors used in organic solar cells. Typical electron acceptors: a) C_{60} , b) PBCM, c) PTCDI; some electron donors: d) P3HT, e) MDMO-PPV, f) α -6T.

istry development which, by introduction of functionalized substitutes, can reach better properties for particular applications. Such a case is represented by C_{60} , which was common electron acceptor, but it was incompatible with wet processing procedures due to its poor solubility[39]. The introduction of functionalizing tail by Schinazi et al. led to C_{60} derivative called PBCM, which good solubility[40] made it a state-of-art electron acceptor used in organic solar cells[41]. Another example of chemical tuning utilization is PEDOT:PSS. Its work function can be tuned by means of chemical and electrochemical redox reactions[42], which allows for optimization of solar cell performance.

As previously explained, organic materials used in fabrication of solar cells need to satisfy few additional requirements like high carrier mobility and environmental

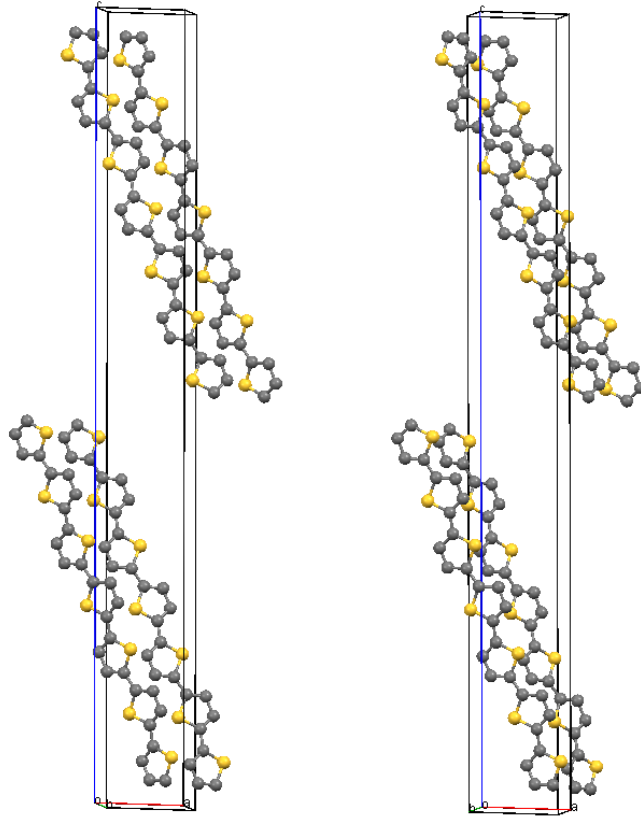


Figure 1.3: Stereoscopic (cross-view) diagram of α -sexithiophene unit cell

stability. Such a combination is well represented by α -6T - C_{60} model, where the first material serves as an electron donor, and the latter as electron acceptor.

α -sexithiophene is an oligomer formed out of six thiophene rings i.e. six aromatic rings consisting four carbon and one sulfur atom connected in α -trans manner. It became interesting in organic solar cell application due to its high hole mobility and inherent conjugated nature[43], that is why the growth of α -6T films were thoroughly studied [44, 20, 45, 46, 47, 48]. In crystal α -6T molecules are arranged in quasi parallel configuration, with long molecular axis lying approximately with (103) crystallographic direction. Stereoscopic (cross-view) diagram of α -sexithiophene unit cell is presented in figure 1.3. α -6T forms monoclinic crystal system which is characterized by three vectors of unequal length, which define a rectangular prism with a parallelogram as the base. Two pairs of vectors are perpendicular, while the third one does not form a straight

a [Å]	b [Å]	c [Å]	β [°]
45.4	7.85	6.03	99

Table 1.1: Crystal unit cell parameters of α -6T[49, 50].

angle. The values of α -6T unit cell parameters, which can be found in literature are presented in table 1.1. The molecules in this crystal exhibit herringbone-like packing with 35° tilt[51]. Described crystalline phase, which is obtained from vapor deposition of the molecule, is called low-temperature (LT) 6T, contrary to the high-temperature (HT), which is grown from the melt[52].

α -6T is commercially available from chemical compound vendors, in form of the powder of different purities. In this work the material purchased from Tokyo Chemical Industry Co., Ltd. and Sigma Aldrich were used. It has the form of coarse powder with number of flakes and bigger grounds. The photograph of the raw material, together with structural formula of the molecule itself are presented in figure 1.4.

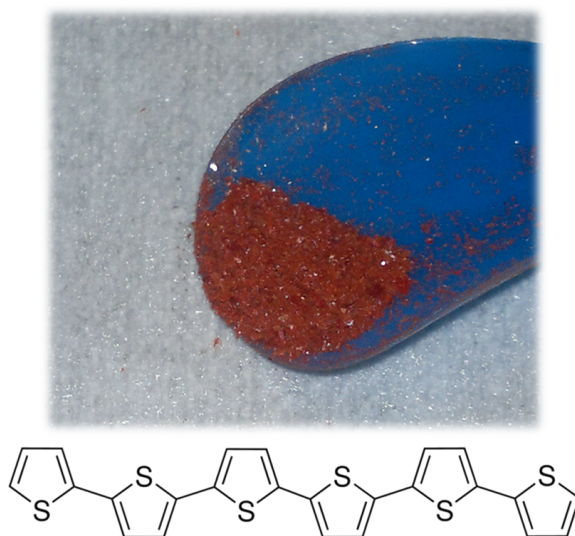


Figure 1.4: Image of α -sexithiophene powder used as a source material for organic solar cells described in this work (structural formula of α -sexithiophene is shown below).

Buckminsterfullerene C_{60} is a fullerene molecule discovered by Smalley *et al.* in 1985[53]. It consists of 60 carbon atoms arranged into truncated icosahedron formed

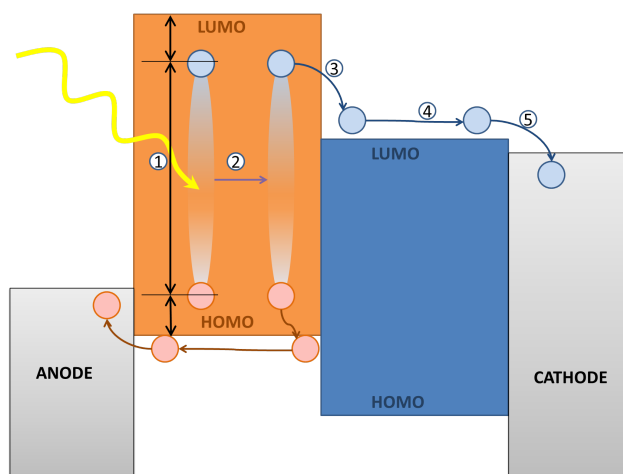


Figure 1.5: Photocurrent generation process in bilayer organic solar cell. The subsequent steps are: (1) absorption of incident photon and creation of an exciton; (2) diffusion of an exciton to the donor-acceptor interface; (3) dissociation of an exciton into free electron in electron acceptor material and free hole in electron donor; (4) charge transport through respective semiconductors; (5) charge collection at the electrodes.

from twenty hexagons and twelve pentagons. The phenomenon discovered by Sacriftci et al.[54] of electron transfer from conducting polymers to buckminsterfullerene has induced research of C_{60} application in solar cells[55].

1.2.3 Basic processes in organic solar cell

As it has already been explained in section 1.2.1, there are intrinsic differences between organic and inorganic devices, and the photovoltaic phenomenon in organic photovoltaic differs from the one observed in inorganic devices. The process of converting incident light into a photocurrent consists of 6 steps which are outlined in figure 1.5, where the energy diagram of an organic solar cell with a donor-acceptor interface is shown. The donor's HOMO and LUMO levels are lower - in comparison of the vacuum level - than of the acceptor. Therefore, the donor layer conducts holes, and forms an ohmic contact with the anode, whereas the acceptor layer conducts electrons, and contacts the cathode. When the donor and acceptor materials, which put into intimate

contact form a p-n junction, are sandwiched between two electrodes (of which one is transparent), a solar cell device is obtained.

Light absorption and exciton generation

As the solar cells are to use sunlight as their illumination source, special emphasis should be put on the properties of the radiation coming from our nearest star. The sun can be considered as a black body with a temperature equal to $\sim 5250^{\circ}\text{C}$, which spectral irradiance well matches experimental data of extraterrestrial measurements. Nevertheless, in order to reach the earth's surface, the sunlight need to pass the atmosphere, where it undergoes scattering and absorption due to constituent gases - primary O_3 , O_2 , H_2O and CO_2 . The comparison of before mentioned spectral irradiances is presented in figure 1.6. In order to take into account, that sun is not constantly

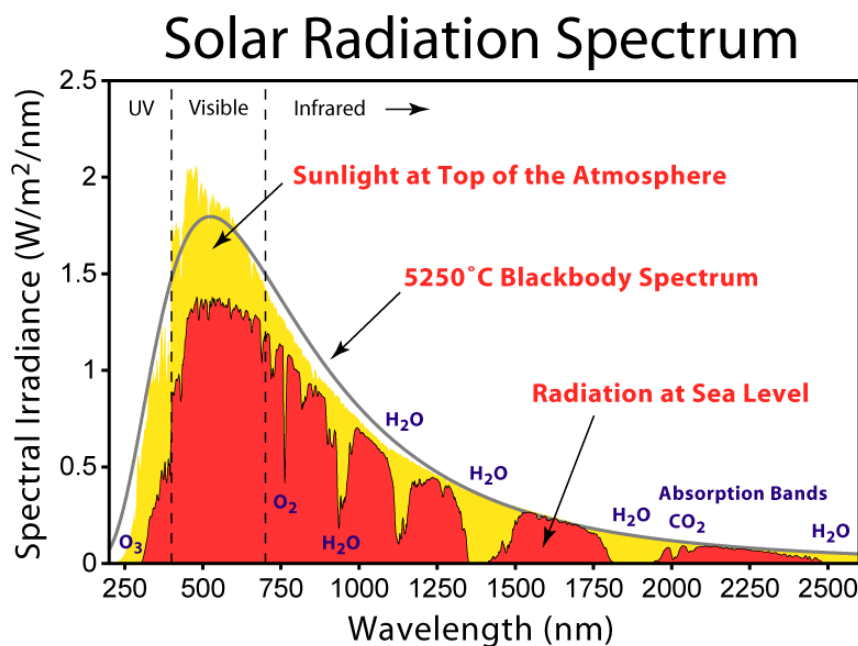


Figure 1.6: Solar radiation spectrum. Extraterrestrial irradiance (yellow) is compared with 5250°C black body radiation (black line), and the irradiance at the sea level (red). The principal absorption bands are labeled with causative molecules. (source: *wikimedia commons File:Solar_Spectrum.png*)

illuminating from the zenith, which implies variable length of the rays in atmosphere,

so called *air mass coefficient* (AM) is introduced. It is defined as:

$$AM = \frac{L}{L_0}$$

where L is the actual distance the light traveled through the atmosphere and L_0 is the atmosphere thickness. Defined as such, AM value varies with latitude, time and season. Nevertheless, for standardization purposes typical value of AM 1.5 is chosen as it covers the average AM values for overall yearly average for mid-latitudes ($40^\circ - 55^\circ$), where most of world's major population and industrial centers is located. The diagram presenting the origin of AM 1.5 spectra is presented in figure 1.7.

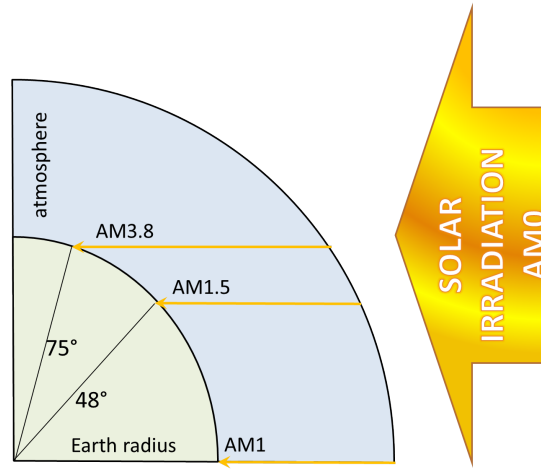


Figure 1.7: The differences in distances travelled by light rays at different latitudes resulting in AM1 spectra at 0° , AM1.5 at latitudes $40^\circ - 55^\circ$, and AM3.8 at 75° (image not to scale).

The photon absorption in organic solar cells instantaneously leads to the formation of an exciton[56]. The efficiency of absorption is predominantly determined by absorption spectra of used materials and thickness of the layers, but also by the device architecture. Due to the fact, that the absorption coefficient of organic materials tend to be much higher than of the poly- or monocrystalline silicon, the thickness of the active layers can be significantly lower. For number of organic photovoltaic materials, the layer sufficient to reduce the light intensity e^{-1} times the incident value does not exceed 100nm, while to obtain similar absorption, the layer of crystalline silicone ought to be two orders

of magnitude thicker[29]. This implies that minimal volumes of materials applied can effectively reduce not only the total cost of the device, but also it's mechanical stiffness.

Unlike inorganic materials, which absorb a continuous spectrum of photons with energy exceeding material's bandgap, organic materials exhibit well defined narrow transitions [57]. Moreover the transition of single molecule can be strongly affected by the presence of neighboring molecules and their orientation, leading to high sensitivity for crystallographic packing. It opens a variety of possibilities for chemical tuning of the absorption spectra to match the desired properties of particular device. It does not always need to be maximal absorption.

Such an approach is utilized in concept of *transparent* solar cells[58, 59, 60] which pass most of the visible spectra, while absorbing strongly in UV and IR bands. Application of those on windows will address one of the major contributors of non-industrial electric energy consumption - air conditioning - by limiting the total energy entering the building, hence lowering cooling demand, while generated electric energy can be utilized by already relieved air conditioners.

Another important factor regarding absorption lays purely in the wave nature of light. As the device consists of subsequent layers, a number of interfaces is being formed therefore reflection together with transmission at each of those will give a rise to standing wave patterns. Knowing the complex indices of refraction of incorporated materials, a generalized transfer matrix method[61] can be used to obtain the interference pattern for each wavelength. Careful choice of thicknesses, or even introduction of dedicated buffer layers[62, 63, 64], can lead to optimal design, where antinodes of most efficiently absorbed light lay in desired location within device[31].

Exciton diffusion

In ideal solar cell, each absorbed photon should lead to formation of a free electron-hole pair. So far, the exciton formation has only been mentioned in section 1.2.1. In order to dissociate, for an exciton it needs to relocate to the interface of the p and n materials. As excitons, consisting of excited electron-hole pair, are neutral species[30], they are unaffected by electric fields inside the device. As so, the only mean of transport for excitons is diffusion[57], which needs to transport the exciton to the interface before it will undergo radiative or non-radiative recombination to the ground state. The

recombination processes limiting the lifetime of an exciton, put a constraint on the total distance it can travel. This distance, known as diffusion length, implies that only those excitons which are formed within the volume within diffusion length from the p-n interface, have a chance to contribute to charge generation. Normally, the exciton diffusion length in typical organic semiconductors does not exceed 20nm[65]. To address this issue, the two main approaches have been considered: increasing the diffusion length, or altering the interface morphology to minimize bulk-to-interface average distance (see figure 1.8).

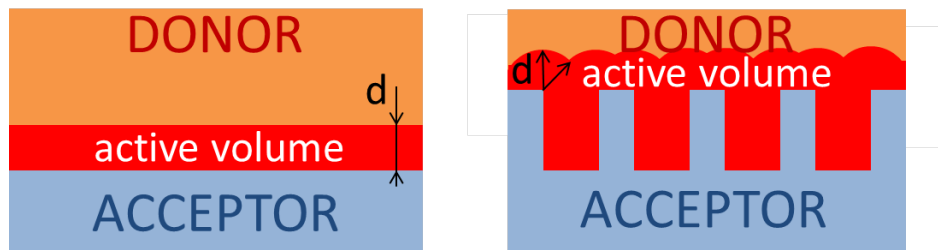


Figure 1.8: The increase of active volume (red) of an organic solar cell by structuring the interface. Only the excitons formed within a diffusion length distance (d) from the electron donor (orange) and electron acceptor (blue) interface will take part in generation of photocurrent. Interdigitated morphology of the interface is an optimal formation for organic solar cells.

Charge separation

Creation of the free electrons and holes is an essential part of solar cell operation. When randomly wandering exciton reaches the donor-acceptor interface, it is still bound by coulomb forces with the typical binding energy of 0.2-1eV[57, 66]. In order to dissociate the exciton, this energy needs to be externally supplied.

The essential concept supporting this process was introduced by T.Wang, who proposed the application of two organic materials with dissimilar electronic properties: donor - with low electron affinity, and acceptor - with high electron affinity, recognizing that the heterointerface between the organic materials allows for an easy charge separation[67]. The simplified condition for exciton dissociation to be energetically

favorable is the following:

$$LUMO_{donor} - LUMO_{acceptor} > E_{binding}$$

The process is depicted in figure 1.9. The charge separation in solid state organic

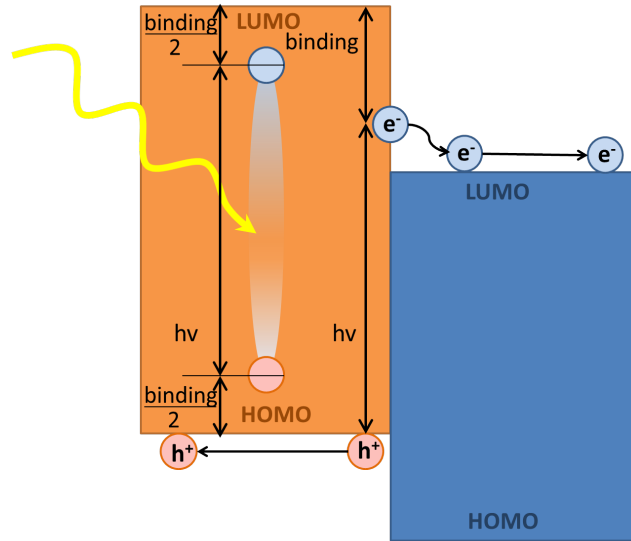


Figure 1.9: Exciton dissociation diagram.

solar cells is not fully understood[68], but it has been shown that it is a multi-step process, which depends on the energy configuration, and other factors[69]. It involves initial formation of polaron pair, that can be separated into free charges only with certain yield[70]. There is still an open debate on the surplus of energy required to effectively dissociate excitons[70].

The requirement for efficient charge separation is to assert, that the charge separation will be thermodynamically the most efficient process for an exciton, while the unwanted - loss - processes like fluorescence or non-radiative dissociation will be suppressed. The next immediate step requires that the charges will be spatially displaced in order to prevent electron and hole annihilation and allow the charges to reach their electrodes respectively[29].

Charge transport

Due to the fact, that in organic solar cells the free carriers occur in separate materials - contrary to inorganic devices - it leads to strong gradients in charge concentration leading to presence of appreciable diffusion currents in addition to drift currents[30, 71]. Because the transport of respective charge goes through pure p- and n-type layer, it is valid to assume that virtually no charges of opposite sign are present, hence the recombination probability during the transport is limited to defects in the device e.g. isolated islands or trapped charges. It implies another issue, that the efficiency of charge transport is mostly determined by carrier mobility and charge distribution inside the layer[72].

There is a number of charge transport models in organic semiconductors described in literature[73, 74, 75, 68, 71], which allow for more accurate prediction of open circuit voltage and resistances within the solar cell device. A simple diagram of charge transport in planar heterojunction is presented in figure 1.10. On the left hand side is

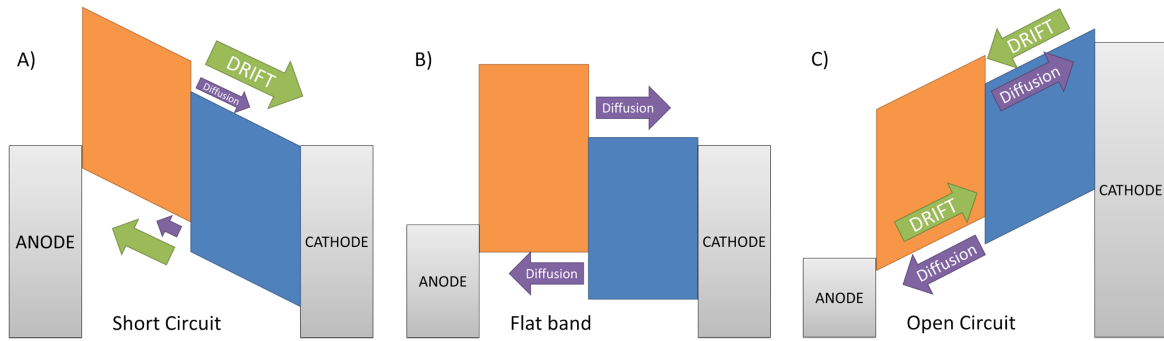


Figure 1.10: Diagram of charge transport in planar heterojunction device: a) short circuit condition; b) flat band condition; c) open circuit condition.(adopted from [71])

a device under short circuit current condition - Fermi levels of electrodes are aligned. The generated internal field will sweep all electrons which occur at the interface towards the cathode, and holes towards anode. Right hand side diagram represents the device under open circuit condition - the drift current compensates the diffusion current, resulting in zero net charge transport. The drift current, to equalize with diffusion current, requires a build up of internal electric field higher than one required for flat band condition.

Charge collection

Electrodes serve the purpose to collect the charge from the device and pass it to external circuitry. As organic solar cells are planar devices, one of the electrodes - depending on device configuration anode or cathode - is required to be transparent. Two main approaches is application of ultra-thin metal electrode which is semitransparent, or transparent conductive oxide, of which ITO (indium-tin oxide) and SnO_2 are the most popular. Special consideration needs to be taken with the choice of the electrodes in order to obtain an ohmic contact with active materials. This is often accomplished by introducing dedicated contact layers; among the others, commonly used contact layer materials are MoO_3 , LiF , TiO_2 , or PEDOT:PSS. They often serve also as efficient blocking layers for opposite charges. The latter one, which is a transparent conductive polymer, can be used as an electrode too.

Loss mechanisms

There is a number of loss mechanisms, which are responsible for deviation of real organic solar cells, from ideal devices[76]. Organic solar cells, contrary to inorganic equivalents, do not absorb continuous spectra, but can utilize the photons only from energy ranges surrounding HOMO-LUMO transition. Hence, way smaller quantity of photons can be efficiently transformed into free carriers at electrodes. Even though it is not a loss mechanism *per se*, it strongly affects organic devices' external quantum efficiency.

Another loss is caused by excitonic nature of organic solar cells, where exciton needs to diffuse from the point of photon absorption to donor-acceptor interface. As previously mentioned, excitons are electrically neutral, therefore they traverse the material by random wandering. Due to their limited lifetime, in case the exciton will fail to reach the donor-acceptor interface, it will decay in fluorescent or other non-radiative dissociation. Real lifetime of excitons is additionally limited by the presence of defect sites and impurities within the active layers, which can trigger dissociation resulting in formation of a phonon.

In case of reaching the electrode rather than donor-acceptor interface, excitons are lost due to quenching on the metal electrode[77]. This issue is commonly addressed by application of exciton blocking layer between n type material and cathode. Typ-

ically bathocuproine (BCP) or 4,7-diphenyl-1,10-phenanthroline (BPhen) is used as thin ($<10\text{nm}$) layer. Both of those materials have a wide band gap, which offsets HOMO, as well as LUMO levels of the acceptor. As a result, excitons are reflected from the interface of acceptor and exciton blocking layer, and are given a chance to reach donor-acceptor interface. What is more, BCP and BPhen layers tend to prevent damages within active materials during deposition of cathode, and can be used as buffer material to optimize optical interference pattern in the device[78].

After dissociation of exciton, formed electron-hole pair is still bound and it can still decay to the ground state with interface dependent rate. Even if the bond will be broken and free charges will be created, the pair can be captured back to form bound pair[70]. This incomplete dissociation of generated bound pairs is responsible for the fact that only about 50% of excitons reaching the interface are converted into free charges[74]. Nevertheless, the charge mobility difference in donor and acceptor [79], as well as the dipole layer at the interface [80] prevents back transfer of freed charges and reduces the probability of recombination of the hole-electron pair.

When the separated charges traverse the device, the series resistance loss is to be expected, which will increase together with the layer thickness. Taking into account that fabricated devices are macroscopic, the fluctuations in material thickness will occur, and there is a possibility that there will be regions with very thin layers or even pinholes which will be seen as low equivalent shunt resistance.

Yet another loss process can be expected at the interface of semiconducting materials with respective electrodes. There, the injection barrier can be formed, which depends on HOMO or LUMO level and the work function of respective electrode. Even educated choice of electrode material can fail, as oxidation, impurities and surface contamination on the contact can lead to significant change in the interface energetics like electrode work functions and carrier injection barriers[81, 72].

Identification of the major loss mechanism in given cell is not a trivial task. number of different methods and techniques are used - from analyzing I-V curves, through impedance spectroscopy [76], to destructive time of flight - secondary mass spectrometry (TOF-SIMS)[82] or X-ray photoelectron spectroscopy (XPS)[83]

1.2.4 Types of Organic Solar Cells

Organic photovoltaics is relatively young branch in science, which first steps established at the beggung of 80's[84]. The research started from exploring the single-single layer configuration[28], but further development of single layer devices led to the conclusion, that effective exciton splitting requires application of two materials with dissimilar electronic properties. Prompt discoveries by Tang[67] and Grätzel[85] caused a split of organic solar cell research into two different approaches namely the dye-sensitized and the heterojunction solar cells.

Single layer solar cells

The first generation of organic solar cells consisted of single organic semiconductor layer sandwiched between two metal electrodes with different work functions[84][28], which operational principle was based on asymmetry in hole and electron injection into molecule's π^* and π orbitals[86], and formation of Schottky-barrier between electron donor and the metal with lower work function[87]. The Schottky-barrier acts here as a sink for minority carriers and a barrier for majority carriers. The reported power conversion efficiencies were generally as low as 0.001% – 0.01%, but introduction of metal-insulator-semiconductor enhancing the Schottky barrier effect, led to remarkable 0.7% result[88]. The energy diagram of the single layer device proposed by Morel *et al.* is presented in figure 1.11.

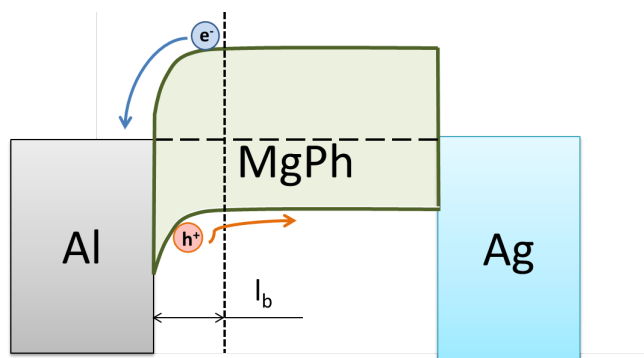


Figure 1.11: The energy diagram of the single layer Al/MgPh/Ag device proposed by Morel *et al.* The energy barrier is formed at Al/MgPh interface.

Dye-sensitized solar cells

Dye-sensitized solar cells were invented in 1988 by Brian O'Regan and Michael Grätzel at UC Berkeley[89]. The construction of the cell incorporates transparent anode on which self-interconnected mesh of TiO_2 particles covered with monolayer of sensitizer dye is deployed. Cathode, which typically is also transparent, is not in direct contact with the mesh, but the whole device is immersed in liquid electrolyte – iodine – which fills the gap between the mesh and cathode, as well as voids between TiO_2 nanoparticles. Schematic diagram of the dye-sensitized solar cell is presented in figure 1.12.

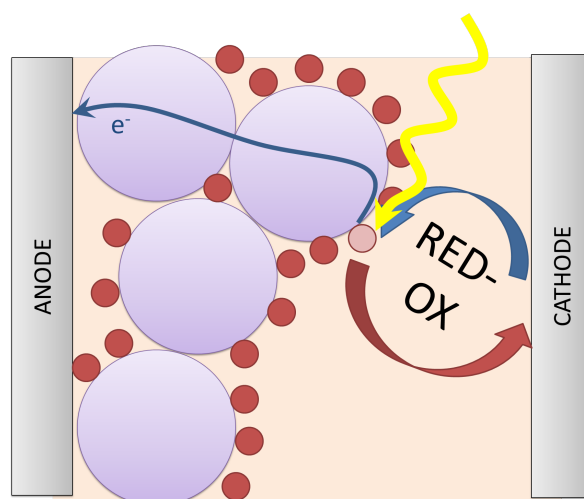


Figure 1.12: Schematic diagram of dye-sensitized organic solar cell operation.

In this kind of device, the light is absorbed by the dye molecules, which turn to excited state and donate the electron to TiO_2 . From there, through interconnected network of nanoparticles, the electron reaches the cathode. Because the dye molecule donated one of its electrons, it will remain inactive, unless it will receive another electron from the electrolyte. Oxidized iodine forms triiodine, which will float around until reaching the anode. There, triiodine gains electrons and is reduced back to iodine. The schematic diagram of dye-sensitized solar cell operating principle is shown in figure 1.12.

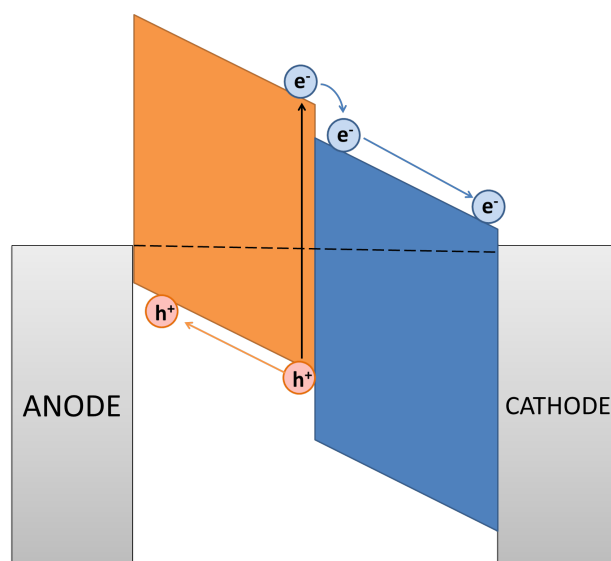


Figure 1.13: The schematic energy diagram of planar heterojunction device.

Planar heterojunction organic solar cells

The major contribution in the development of planar heterojunction solar cell was to recognize the necessity of interface stimulated exciton dissociation proposed by Tang and others in 1986[67], who, with utilization of phtalocyanine derivative as p-type semiconductor and perylene derivative as n-type semiconductor, has beat the 1% power conversion efficiency barrier. The developments in the field of conjugated polymers, together with discoveries of interesting optoelectronic properties of fullerene-conjugated polymers mixtures led to the development of polymmer-fullerene bilayer heterojunction[90], and further - to the bulk heterojunction[91]. The energy diagram of planar heterojunction is presented in figure 1.13.

As previously described in section 1.2.3, efficient photoconversion occurs only in thin layer of active material restricted to tens of nanometers by exciton diffusion length. This puts a strong constraint on the light absorption, as such thin layer will not collect the photons effectively enough. This fact led to the conclusion, that highly corrugated interface will significantly improve the organic devices.

Bulk heterojunction solar cells

An initial step towards bulk heterojunction was made by research of Hiramoto, who investigated application of p-i-n junction in organic solar cell, where *intrinsic* layer consisted of coevaporated p- and n-type materials[92]. Then, with rise of fullerene - conjugated polymer devices, concept of blending together p-, and n-type materials emerged[91].

The limitation of exciton diffusion length governs in all organic solar cell devices, but in bulk heterojunction approach, the materials are fabricated in a way, which assert that the distance from any point in the bulk to the interface will be in range of tens of nanometers. The schematic illustration of bulk heterojunction structure is presented in figure 1.14.

Solving one problem, bulk heterojunction structure has introduced new challenges, of which major ones are the trap sites and path continuity, and selective charge collection at the electrodes. Diagram depicting those issues is presented in figure 1.14. As

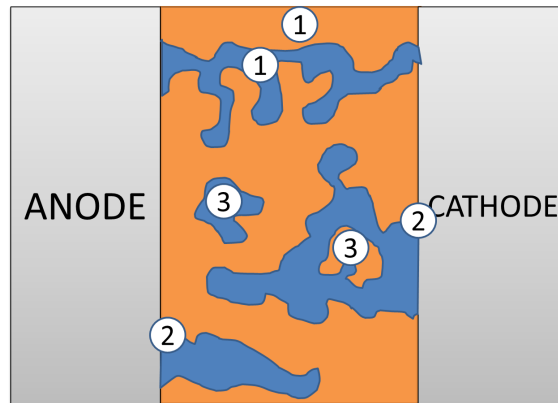


Figure 1.14: BDiagram of bulk heterojunction solar cell with limiting factors depicted:
 (1) interconnection of both electrodes by the same type of semiconductor;
 (2) connection of both types of semiconductor to one electrode; (3) trap sites not connected to either electrode.

the principle of operation is exactly the same as in bilayer heterojunction system: after photon absorption, exciton diffuses towards the interface and dissociates into free charges. The charges, in order to be collected, need to have continuous path to their respective electrodes. In case of trap sites or islands presence, charge buildup can occur, which will negatively alter the device performance. Moreover the application

of solely hole- or electron-transport layer is required between the electrodes and the blend in order to prevent recombination of separated carriers as both p- and n-type semiconducting materials are in contact with each electrode.

1.2.5 Configurations of solar cells

There are four basic configurations of solar cells separated by the direction of the photogenerated charges conduction with respect to the substrate and on the direction from which the solar cell is being illuminated. The devices, where the electrons are traversing the structure in the direction outwards from the substrate are said to be of normal geometry, while the ones, where the electrons move towards the substrate are of inverted geometry. The devices, which are illuminated through the transparent substrate, are called front illuminated, while the ones illuminated from the other side are called back illuminated. The four configurations are presented in figure 1.15. The

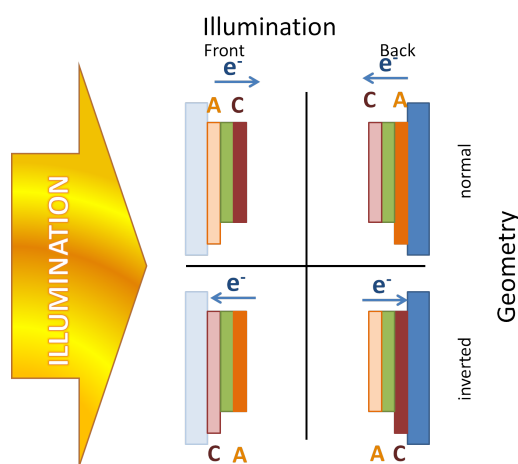


Figure 1.15: Basic configurations of solar cells. Top row: normal geometry, bottom row: inverted geometry. Left column: front illuminated, right column: back illuminated. A-anode (orange), C-cathode (red); arrows indicate the flow of electrons in active layer (green).

current work focuses on the device which has non-transparent cathode deposited on the substrate, and it is illuminated through transparent anode. Such a configuration is defined as inverted geometry back illuminated solar cell.

1.3 Crystallinity influence on solar cell performance

There are various strategies for improving efficiency of organic solar cells targeting at different aspects in power generation process such as: enhancing the electronic properties of the materials by doping[57], applying gratings to elongate the light path within device or other metallic structures for electric field enhancement [93], dimensioning the device to harvest light interference effects or minimizing average bulk to interface distance by application of interdigitated P-N materials[94]. Number of those strategies can be realized by control of the crystallinity of the donor material. Therefore, the present work aims at study of the influence of α -sexithiophene morphology and crystalline properties over the performance of solar cells where it serves as donor material.

Crystalline structure of the material determines the mutual alignment of the molecules which constitute the crystal, which have several implications on the performance of the solar cell.

The enhancement in crystallinity improves the $\pi - \pi$ stacking, hence results in better defined bands formed by HOMO and LUMO levels of individual molecules[95]. It improves overall electrical and optical properties of crystalline structures in contrast with amorphous or polycrystalline materials[96]. As the exciton diffuses by sequence of Förster transfer processes, the diffusion length will be increased when optical transitions will encounter less defects, and when the overlap between emission and absorption will be large[57]. Because the α -6T exhibits anisotropy of carrier mobility[97], the case of crystals consisting of the laying molecules exhibit the increased carrier transport in the direction perpendicular to the substrate, which is favored for solar cell applications[98]. Fortunately, such orientation of crystalline sites results also in optical transition dipole being parallel to the surface improving the absorption of light by α -6T molecules.

All of above mentioned reasons support the pursue to investigate the influence of crystallinity on the performance of organic solar cells.

1.3.1 Growth of organic nanostructures

The growth of α -6T nanostructures has been already observed on many substrates like muscovite and phlogopite mica[20, 99], ITO, polyvinylpyrrolidone [100], polyte-

trafluoroethylene [101], SiO₂[44], as well as on Au [102, 103], for which the temperature dependence of the obtained structures morphology was also observed. There are three basic growth modes of material acquired via adsorption: Volmer-Webber island formation, Frank-van der Merwe layer-by-layer growth, and Stranski-Krastanov layer-plus-island growth. In the simple approach, the mode of growth depends on the interplay between intermolecular and surface adhesive forces. Intermolecular cohesive force stronger than surface adhesive force leads to Volmer-Webber growth, while surface adhesive force stronger than intermolecular cohesive force leads to Frank-van der Merwe growth.

The Stranski-Krastanov growth mode occurs when the balance between the forces changes with the film thickness from initially dominating surface adhesive forces to the predominance of intermolecular cohesive forces after exceeding the critical thickness resulting in drop of the surface energy.

Studies of the ultra-thin sexithiophene and other thiophene oligomer films have revealed that structure formation can, on some substrates, follow Stranski-Krastanov growth mode[48, 103, 24]. Stranski and Krastanov describe the growth of the structures to occur in three major steps. Initially a wetting layer of adsorbed molecules is formed. The wetting layer can consist of few monolayers, which in case of α -6T molecules will mean 0.6nm-1.5nm of nominal film thickness. With increase of nominal thickness, the 3-dimmmensional crystallites are being randomly formed on the surface. When the crystallite density will exceed the critical value, the crystallites can spontaneously rearrange into 1-dimmmensional chains - nanofibers - as seen on muscovite mica[20, 99] or gold[102, 103]. From this moment the nanofibers and crystallites co-exist, with remarkable crystalline depleted zone around the nanofibers. The process is depicted in figure 1.16. All steps of the Stranski-Krastanov growth mode are significantly affected by the substrate on which the molecules are being deposited, as well as its temperature resulting in formation of variety of structures in vast range of dimensions[104]. Temperature increases the surface mobility of the molecules, therefore it is possible for them to traverse the substrate's surface in order to find a local energetic minimum, before it will be buried under upcoming molecules. Therefore, the slow deposition rate is very crucial to obtain crystals of good quality - the individual molecules will have enough time to find their place in the crystal structure of the formation.

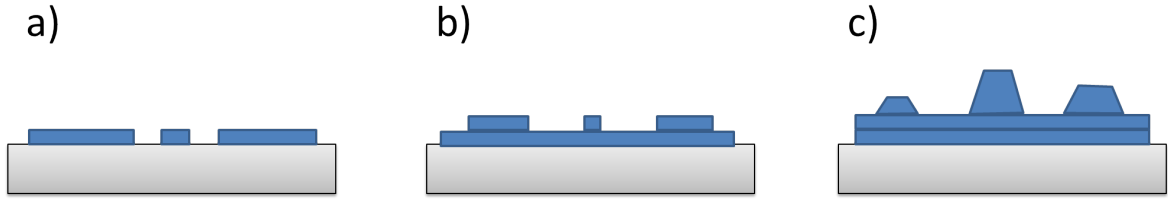


Figure 1.16: Cross view of structures formed in Stranski-Krastanov growth mode with submonolayer thickness (a), before reaching critical layer thickness (b), after exceeding critical layer thickness(c).

The studies of growth of oligomer nanostructures on mica have shown that with further deposition of the material, the nanofibers mostly increase their length (up to hundreds of micrometers), while width and height does not exceed few hundreds of nanometers[104]. The growth anisotropy is a result of anisotropy of the constituent molecule itself. Works of Kankate et al.[20] have shown that the individual α -sexithiophene molecules' long axes can be skewed with respect to the long needle axis by 90° , 65° and 75° for (-401) or (-411) , (020) and (-421) contact faces, respectively. Those crystalline orientations in fibers are presented in figure 1.17.

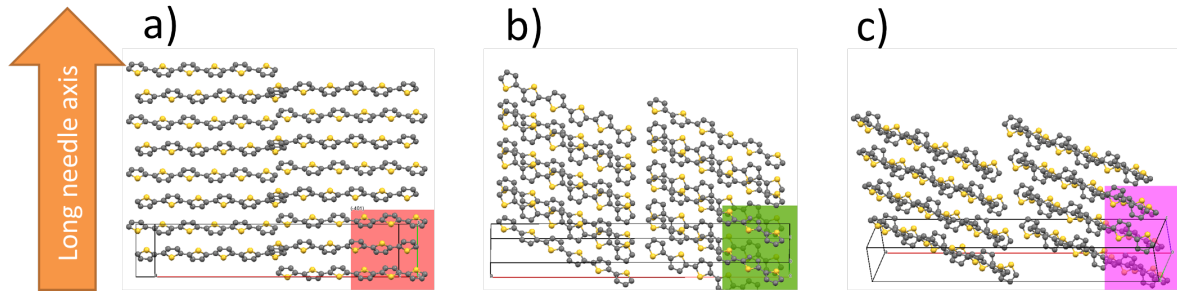


Figure 1.17: Molecular packing of α -6T fibres with contact faces: a) (-401) ; b) (020) ; c) (-421) , resulting in long molecular axis tilt with respect to the long fibre axis equal to 90° , 65° and 75° , respectively.

1.4 Implementation of α -sexithiophene nanostructures in solar cells

In this project, the α -6T – C_{60} material combination was investigated. In the past, a deep understanding has been gained of the materials separately[105, 106, 44, 103, 107, 108], as well as combined in electronic devices[109, 110, 111, 112, 113, 114].

Especially the mutual alignment of the energy levels of C_{60} and α -sexithiophene have been studied by Ge et al.[111]. Which led to investigations of α -6T / C_{60} solar cells [110, 113, 112, 115]. Model device which will be used in this work is an inverted solar cell with structure presented in figure1.18. The α -sexithiophene electron donor layer

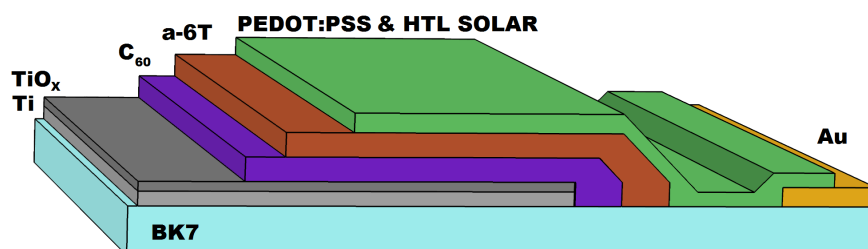


Figure 1.18: Layer diagram of inverted, back illuminated organic small molecule solar cell used in this work.

is to be grown directly on the layer of buckminsterfullerene, which serves as electron acceptor. Thin layer of C_{60} has not exhibited any crystallinity, therefore it is considered amorphous.

Based on previous works, where the growth of crystalline nanostructures on selected substrates was shown, the growth of structures on buckminsterfullerene thin film was be investigated. Moreover, this work presents the processes and techniques which allow for implementation of α -sexithiophene nanostructures on the C_{60} layer into functional organic solar cell.

To realize this, a dedicated growth study of α -sexithiophene thin-film on the C_{60} layers was conducted. The key points of interests here were the presence of various forms of α -6T nanostructures which can be obtained on C_{60} interface, as well as the internal structure of those formations. Four main techniques were used: atomic force microscopy (AFM) and epifluorescence microscopy, to investigate the morphology of the obtained structures, as well as the epifluorescence polarimetry and X-ray diffractome-

try to gain an insight into internal structures of the crystalline formations. Keeping in mind the aim of application of nanostructures in organic solar cells, the expected nominal thicknesses of α -sexithiophene layers are about 30nm, while the XRD technique's recommended nominal thickness of investigated material is 100nm. In order to be able to include X-ray diffractometry data in conclusions about structure of thinner samples, two parallel series of experiments were conducted: one with 30nm nominal thickness of α -6T, and other with 100nm. The coherency in the morphological investigations allowed for correlation of the crystallographic properties between the thin and thick samples.

Furthermore, the next step is to implement those various structures into solar cells and measure their performance. Epifluorescence measurements after the electrical characterization will provide a link to the previous experiments which will allow to conclude about morphological and crystalline structure influence on the performance of organic solar cells.

1.5 Solar cell characterization

The principal aim of the organic solar cell is to convert the energy of light striking the device into electrical energy which can be easily utilized. Therefore, the need exists to measure the performance of fabricated devices which will be repeatable and standardized in order to monitor the progress of device development, as well as to compare different devices. Standardized illumination conditions are asserted by usage of solar simulators, while photogeneration of current under various loads is investigated with the help of source meters.

There is number of parameters: open circuit voltage (V_{OC}) in volts, shorts circuit current density (J_{SC}) in mA/cm², and fill factor, which, together with current density - voltage chart (J-V curve), provide a basic characteristics of a solar cell.

J-V curve

is a plot obtained from measuring the current density flowing through a device at range of bias voltages - typically the measurement range starts at 0V and ends just right after the point, when measured current turns negative. In practice, it is realized

1.5. SOLAR CELL CHARACTERIZATION

as a voltage step-sweep, with simultaneous current measurement. Due to the fact, that solar cell is an active device (it produces the energy), the convention of positive photogenerated current is used for convenience. The J-V curve of the ideal solar cell is the superposition of the J-V curve of the solar cell diode in the dark, with the photogenerated current[116]. In case of the real solar cell, the resistive effects reduce the efficiency of solar cell by dissipating power in the resistances. The first order approximation includes equivalent series- and shunt resistance resulting in equivalent circuit presented in figure 1.19, where the current is governed by modified Shockley ideal diode equation:

$$I(V) = I_L - I_0 \exp \left[\frac{q(V + I(V) \cdot R_S)}{nkT} \right] - \frac{V + I(V) \cdot R_S}{R_{SH}}$$

where $I(V)$ is the current flowing through device, I_L is photogenerated current, I_0 is the solar cell diode reverse bias saturation current, V is the voltage across the device, q is the electron charge, n is the solar cell diode ideality factor, k is the Boltzmann constant, T is the absolute temperature, R_S is the value of the series resistance, and R_{SH} is the value of the shunt resistance.

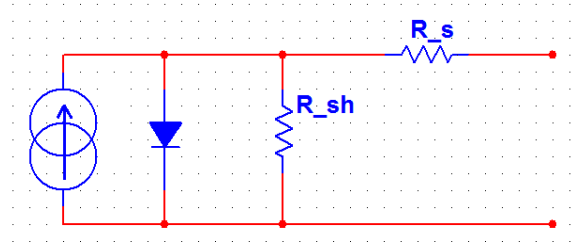


Figure 1.19: Equivalent circuit of solar cell.

The equivalent series resistance is a result of the carrier movement in donor and acceptor layers, interfacial barrier at the electrodes, and the electrode intrinsic resistance. It has a major impact of the fill factor, but excessively large values can alter short circuit current as well. The equivalent shunt resistance emerges from ohmic leakage through the device usually caused by fabrication faults. It reduces the efficiency by providing the alternative current path for photogenerated current. The parasitic resistances manifests themselves on the I-V curve by introducing linear slopes in low

and high voltage regimes for shunt and series resistance, respectively. This impact of parasitic resistances on I-V curve is presented in figure 1.20.

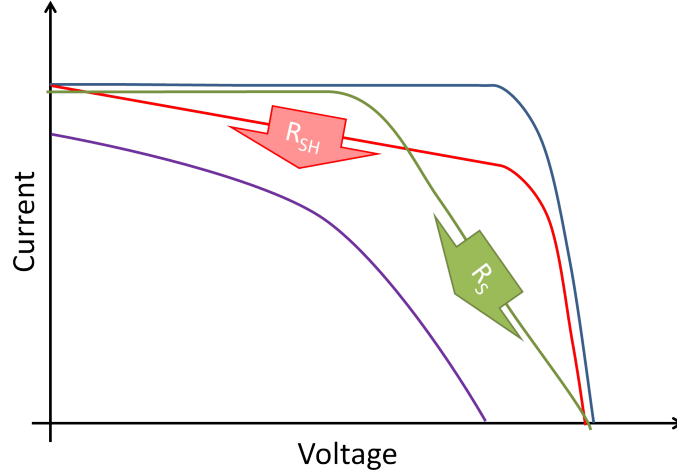


Figure 1.20: Effect of parasitic resistances on I-V curve: ideal I-V curve ($R_s = 0$, $R_{sh} = \infty$)(blue); increasing equivalent series resistance (green); decreasing equivalent shunt resistance (red); effect of high equivalent series resistance and low equivalent shunt resistance (violet).

Open circuit voltage

is the value of the voltage at which J-V curve reaches the value of 0 mA cm^{-2} . Alternatively, it is the voltage which can be measured at the device's electrodes under the open circuit condition. Measuring voltage in fully open circuit is difficult, but measurement across sufficiently high resistance approximates open circuit voltage accurately. The input resistance of the voltage meter used in experiments typically exceeds $10 \text{ M}\Omega$.

Short circuit current density

is the value of the current density, at which the J-V curve crosses the 0 V axis. Alternatively, it is the current density value under the short circuit condition. Unlike many other energy sources like mains, batteries, or generators, solar cells exhibit number of phenomena strongly limiting the short circuit current, therefore short circuiting a solar cell typically does not harm its internal structure.

1.5. SOLAR CELL CHARACTERIZATION

Special care needs to be taken in order not to bury the small values of measured current with measurement error which should be introduced by contact- , or connection wires resistance. The most common way to compensate for those errors, is the application of 4-terminal sensing, also known as Kelvin sensing.

Fill factor

is defined as a ratio of the maximal power density obtainable from tested solar cell under standard illumination conditions to the product of V_{OC} and J_{SC} .

$$FF = \frac{V_{MPP} \cdot J_{MPP}}{V_{OC} \cdot J_{SC}}$$

It is a key description parameter, as it is directly influenced by equivalent series and shunt resistances, hence it gives an immediate insight on quality of the solar cell.

PCE

The power conversion efficiency (PCE) can be derived from above mentioned parameters. It is a performance parameter defined as the ratio of power density at maximum power point, to the irradiance from solar simulator.

$$\eta_{PC} = \frac{(V \cdot J)|_{MPP}}{I} = \frac{V_{OC} \cdot J_{SC} \cdot FF}{I}$$

Therefore, it describes the total efficiency of a photovoltaic system, from the incident light (of standardized intensity and spectrum), to the device terminals. Even though this figure of merit gives very important information which allow to predict device's behavior while deployed in field, it lacks the information about actual processes in solar cell.

Solar cell is a quantum device in terms that converts a single photon into single pair of free charges with various efficiencies for different photon energies. There are two types of quantum efficiency, namely: external quantum efficiency and internal quantum efficiency. The first one is defined as a ratio of number of generated free charge pairs, to the number of photons striking the device. As this measurement is done for a range of incident light wavelengths (typically 300nm-1200nm), the external quantum efficiency

is presented as a spectral chart. As it still includes reflectivity and transmissivity of the device, in order to characterize the efficiency of active layer solely, the internal quantum efficiency is used. Internal quantum efficiency is defined as a ratio of number of generated free charge pairs to the number of photons which are absorbed (in contrary to external quantum efficiency, which took into account all incident photons).

Above mentioned efficiency measures exhibit respective increase of the insight into the solar cell performance, but also in the difficulty of the measurement. Therefore, in this work only the power conversion efficiency will be considered. As its value strongly depends on surface and back electrode reflectivity and transmissivity, comparison of absolute values with the results obtained by other research groups is not trivial and should not be performed carelessly.

Yet another efficiency measure is energy payback time (EPBT), also called the energy amortization. It is defined as an operational interval in which the device will generate the energy equal to the total energetic cost of the device fabrication. It is an important figure for sustainable energy, and organic solar cells, due to low energy requirement during fabrication, can exhibit energy payback time as short as days [13]. Nevertheless, as present study focuses on basic processes in the solar cell, the energy payback time will not be considered in current work.

2 Experimental

As the fabrication and characterization of photovoltaic devices lays in the core of this thesis, I will introduce the considerations undertaken during the design of the device itself, as well as the whole process within which it was fabricated. The main drivers for the device design were full in-house fabrication and characterization. In-house processing allowed for rapid optimization of the devices and prevented third-party caused delays. Moreover, it was decided to fabricate a number of individual devices onto one substrate, which gave the possibility for simple statistical processing of obtained results, as well as easy detection of outliers. Fabrication was performed with usage of in-house made triple source OMBD system under high vacuum conditions, and in N₂ filled glove box. Devices were characterized in the test station constituent of commercially available instrumentation, custom made fixtures, and LabVIEW acquisition and control software.

2.1 Device layout design

Even though there is not any standard yet, the typical active areas of organic solar cells reported by researchers can be divided small $<2\text{mm}^2$ and bigger ones. As the consideration of the size of solar cell is of great importance[16], we have decided for most commonly found value of 1mm^2 .

The device layout design was developed taking into consideration its applicability to standard and inverted solar cell configurations, as both are investigated at NanoSYD[93][117]. Therefore the solution with displaced top electrode was chosen (see figure 2.1). Such a configuration provides a convenient solution, where all external connections can be accessed from one edge of the sample.

Connecting the devices to external equipment is a widely known challenge and one can choose from number of different approaches each with their pros and cons. The

2.1. DEVICE LAYOUT DESIGN

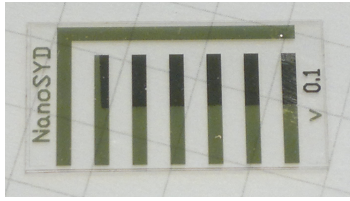


Figure 2.1: Image of the substrate used in experiments. L-shaped common electrode on the left hand side is accompanied by six individual device electrodes.

most straightforward solution is to use a probe station. However, it requires repositioning of the measurement probes for measurement of each device from one substrate; for 4-wire measurement it can be a tedious and error prone task. The solution addressing this issue is the simultaneous application of multiple test probes. Such a probing setup, build for initial tests is presented in figure 2.2. Nonetheless, this solution still suffers

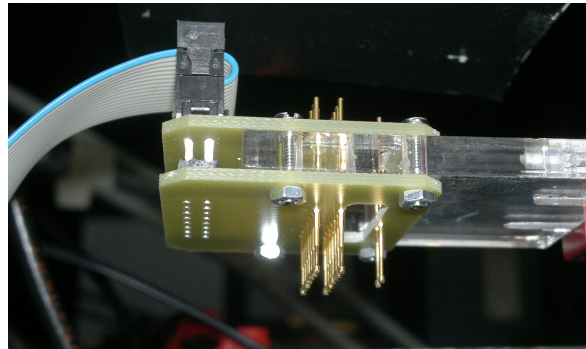


Figure 2.2: 16-pin probe used to establish electrical contact to all devices simultaneously.

from the fact, that, in such a system, the sample needs to be fixed with respect to the measurement table. It has been observed, that for devices distributed spatially on the substrate, the mutual alignment between light source and device under test (DUT) needs to be asserted, as the light intensity distribution exceeds 20% at 20mm distance. The approach taken during this project involved application of zero-insertion-force (ZIF) connector of dense pitch, which provided two contact points to each electrode - required for 4-wire measurements - as well as easy manipulation of the substrate fixed with respect to printed circuit board (PCB).

The choice of $300\mu m$ thick substrate allowed to use standardized flexible flat cables ZIF sockets to connect fabricated devices to the measurement equipment. Standard 2.5mm pitch between devices has been chosen in order to comply with the industrial standard, and 6 devices were fit on one substrate. This, together with concerns about convenient manipulation yield to usage of 20mm x 10.5mm substrates. To facilitate easy wafer dicing, alignment marks were introduced to get cross-hair markers at individual substrate's corners.

Organic semiconductor materials used in contemporary organic electronic devices are known to degrade rapidly due to oxygen, water, and UV exposure[118]. Even though the study of those factors is not in the scope of present dissertation, it needs to be taken into consideration. In order to minimize their influence, the fabrication process followed strict time plan which ensured that the duration of exposures to degrading factors were minimal and equal for all samples.

2.1.1 Electrodes

The electrodes provided two main features on their two ends: on one, a electrical contact of proper work function to the solar cell device, while on the other, a robust, low resistance connection to the external equipment. The gold was chosen as the base material, over which Ti, later oxidized to TiO_x , was deposited within device areas. The suitable way to obtain such configuration is the usage of the photolithography process to create a pattern in photoresist, followed by e-beam evaporation of metals.

As the critical dimensions are relatively high ($\sim 50\mu m$), and number of design iterations was expected, masks printed on transparencies were initially considered. Unfortunately, due to low contrast (1:100), high pinhole content, and poor edge quality of printed masks, the external provider (Microlithography services Ltd.) has been chosen to supply commercial mylar 4' micrograph masks (see figure 2.3). Optimized negative photolithography process, on $300\mu m$ BK7 double polished wafer, lead to definition of resist-free metalization areas.

Au was deposited in an e-beam evaporation system over the entire wafer, while the following Ti layer was deposited through a shadow mask(see figure 2.3). The mask was aligned with the wafer to obtain Ti coverage only on cathodes area. The electrode fabrication process is illustrated in figure 2.4.

2.1. DEVICE LAYOUT DESIGN

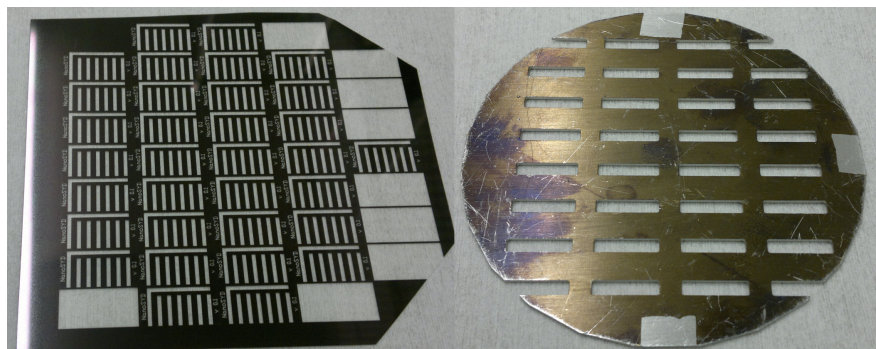


Figure 2.3: The masks used for fabrication of electrodes. Left hand side: mylar mask for photolithography process; right hand side: aluminum shadow mask for deposition of Ti only in the active area of the cathodes.

2.1.2 Active layers

Two layers of active materials are involved in operation of devices described in present dissertation: electron acceptor - C_{60} and electron donor - α -6T; both compatible with OMBD process. In bi-layer configuration, those layers are deposited subsequently (first acceptor, and then donor), and both should fully cover the designated areas in order to prevent internal short-circuits and pinholes. Moreover, it should be ensured that the bottom electrode will be in contact with the acceptor only, while top electrode only with the donor. Such a formation can be obtained by taking into advantage the spatial displacement of molecule sources in the OMBD setup and the finite distance between the sample and the shadow mask which is used to restrict the deposition to the desired area. Illustration of such a ledge-layer formation is presented in figure 2.5. The opening of the shadow mask needs to be positioned with respect to the substrate and the sources in a way, which will ensure that the first layer will exceed the tip of the electrode, while the second layer should overlap enough with the first one and the electrode to provide desired active area - 1mm^2 .

2.1.3 Top electrode

In order to obtain a functional device from already described structures, the top electrode is needed. As the designed device is to be front-illuminated, it is desirable to apply transparent electrode. Thin (20nm-30nm) metal layer would serve the purpose[119],

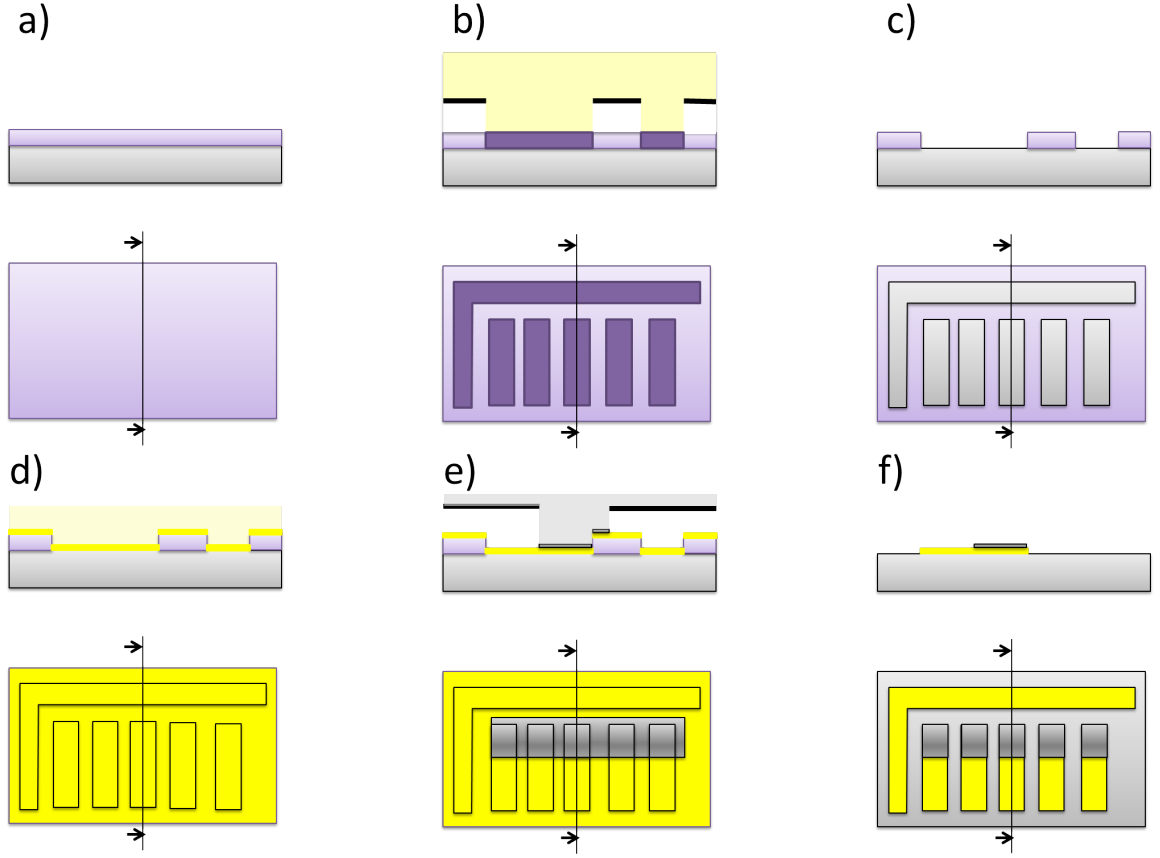


Figure 2.4: Cross section and top view of fabrication process steps of a solar cell substrate: a) spin coating photoresist; b) photolithography through mylar mask; c) development; d) Au deposition on whole wafer; e) Ti deposition through shadow mask; f) photoresist lift-off.

but its deposition would require thermal or e-beam evaporation process, which produce only semitransparent layers, and the latter both are known to be harmful for unprotected organic layers. Applied solution involves a transparent conductive polymers mixture: PEDOT:PSS, which is widely used in solar cell research [120]. Moreover, it exhibits strong electron blocking properties [121], which are favorable in designed device stack. It has also a big advantage of easily applicable spin-coating deposition. The active area of the device is restricted to the region in which all the conductive layers overlap. Therefore, in order to define the device area, weakly adhesive masking

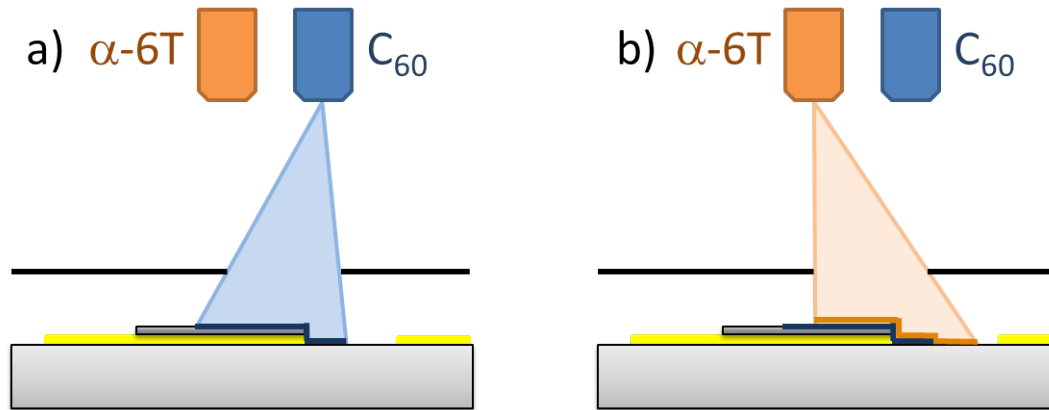


Figure 2.5: Ledge layer formation by subsequent depositions of: a) C_{60} ; b) α -6T

tape can be used. Such deposition complies with ledge layer configuration, which is presented in figure 2.6.

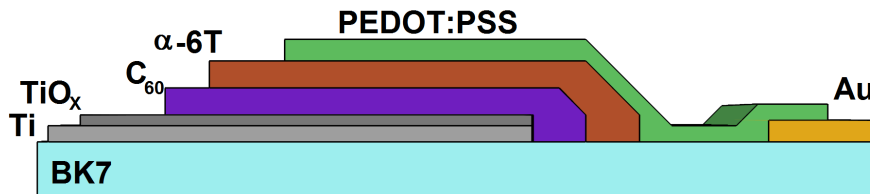


Figure 2.6: Layer stack of a device after PEDOT:PSS spin-coating process.

Because the transparent top electrode serves not only as hole transport layer, but also needs to pass the current to the displaced electrical contact – the compromise between blocking electrons and conductivity was achieved by mixing commercially available PEDOT:PSS solutions: HTL - exhibiting strong electron blocking properties, and PPP - the conductive one. The blend was prepared with 1:1 ratio and sonicated for 30 min[93]. After preparation it was kept in dark at 4°C.

2.1.4 Encapsulation

Due to already mentioned degrading impact of O_2 , H_2O , and UV the device requires appropriate protection. Among many solutions[122, 123, 124], commercially available UV curable epoxy encapsulants stand out by their easy application by spin coating -

which is already employed in fabrication process. DELO katiobond LPVE was chosen due to its fast delivery time and possibility to order in small (nonindustrial) quantity.

It has been found, that it does not have sufficient O_2 and H_2O permeability to prevent the long-term degradation of fabricated devices, but allows for repeatable measurements of shortly stored devices. It was expected that during curing it will not fully protect the devices (drop in short circuit current density was observed), but it has been found that vast majority of fabricated devices exhibit the maximum power conversion efficiency after 15 min of light soaking under 1sun 1.5AM conditions.

The cross section of the device with all layers is presented in figure 2.7.

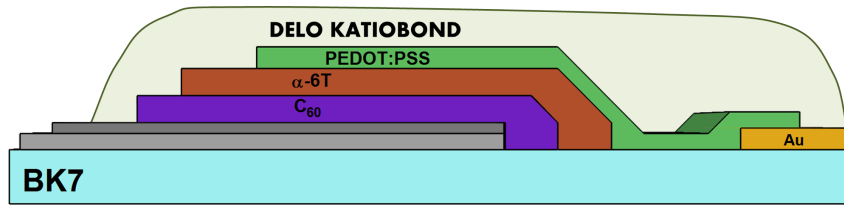


Figure 2.7: Layer stack of fully fabricated device with encapsulation

2.2 Fabrication process

2.2.1 Substrate preparation

Prior to processing the $300\mu m$ thick BK7 double polished wafers (UniversityWafer Inc.) were sonicated in 5 min in acetone, rinsed with deionized water and blow dried with N_2 . Hexamethyldisilazane (HMDS) was applied as photoresist adhesion promoter in HMDS oven system (Yield engineering systems LP-III), by vapor exposure for 5min at $120^\circ C$. After this step, the wafers were let to cool down at the room temperature for 15 min.

Photolithography

AZ 5214E photoresist was spun over the wafers with usage of spincoater (Rein Raum Technik LANZ EBS 11.04) with 5s dispensing time, 5s acceleration at 800 rpmps, and 30s spinning at 4000rpm, which resulted in $1.5\mu m$ thick photoresist layer. Subsequently, the wafers were pre-baked on a hot-plate for 60s at $90^\circ C$.

2.2. FABRICATION PROCESS

Exposure was performed in mask aligner (Karl Suss MA150ML) using 254nm Hg line. Blank quartz mask was loaded into mask holder, while the mylar mask was placed directly on the wafer. The wafers were exposed through the mask for 40s, inversion baked at 140°C for 120s and flood exposed (without mylar mask, but with the blank quartz mask) for 120s.

Photoresist was developed in AZ 351B developer for 60s at 21°C; during the development manual agitation was performed.

Wafers with developed photoresist were cleaned in two subsequent deionized water baths and spin-dried in wafer washer system (Semitool PCM328).

Metal layers deposition

All metalization steps were performed in Cryofox 600 Explorer system, under the pressure of 10^{-5} mbar. Initially, 3nm adhesive layer of Ti was evaporated at and 5Å/s deposition rate, 30nm of Au at 5Å/s (in some samples substituted with 80nm of Al at 5Å/s). Then, after fixing of the shadow mask, 20nm of Ti was deposited at the same deposition rate as the adhesive layer.

After metal deposition steps wafers were stripped-off from photoresist residuals in acetone bath, where they were sonicated for 10 min. Next, the wafers were cleaned in two subsequent deionized water baths, and spin dried.

Dicing

The wafers with metal structures were diced to 20mm x 10.5mm substrates with usage of semiautomatic Disco DAD-2H5 dicing saw using diamond spin blades with 3mm/s cutting speed. The cutting depth was set to 200 μ m leaving 100 μ m support. The substrates were rinsed with deionized water and stored in custom designed racks for future use (see figure 2.8).

Oxidation of titanium layer

Prior to deposition of organic layers, substrates were pre-cleaned by ultrasonic bath in acetone for 5 min, rinsed with isopropyl alcohol and deionized water, blow-dried with N₂, and exposed to 130W RF glow discharge oxygen plasma for 90s in 120 Barrel Plasma System (LFE Plasma Systems) with 75 sccm/s oxygen flow. The treatment

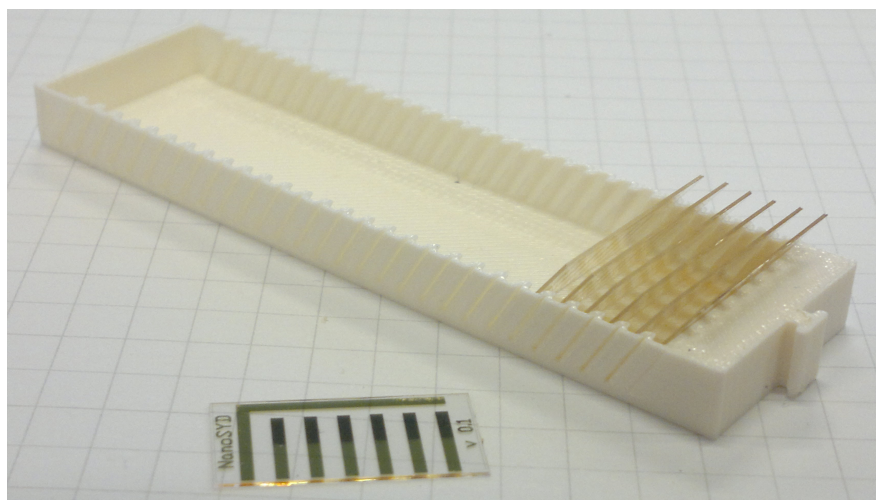


Figure 2.8: Image of dedicated substrate storage system fabricated with 3D printer.

forms a thin layer of TiO_x on the surface, which has been demonstrated to work as a cathode interfacial layer in organic solar cells[125].

2.2.2 Organic molecular beam deposition

Vacuum system

The diagram representing OBMD setup, which was built with Arkadiusz Goszczak for the purpose of this project, is presented in figure on the next page. It consists of three Knudsen cells separated with heat shields, heated substrate holder shutter, and measurement instrumentation: ionization pressure gauge (with Varioan Multgauge L385 controller) together with quartz crystal water cooled micro balance controlled by Maxtek TM-350 deposition monitor. Due to the fact, that deposition rates involved in fabrication processes described in the present work are in order of a tenth of an ångstrom per second, default device display was not sufficient to provide relevant information because the slowest deposition rate it could indicate was 0.1 Å/s . Monitoring the analog output signal (in 0-5V standard) was just a virtual improvement, as it was generated in 10mV increments which corresponded to 0.02 Å/s , and a noisy electrical environment did not allow for reliable measurements of such small increments. Therefore, the deposition monitor was repeatedly queried for actual frequency of microbalance

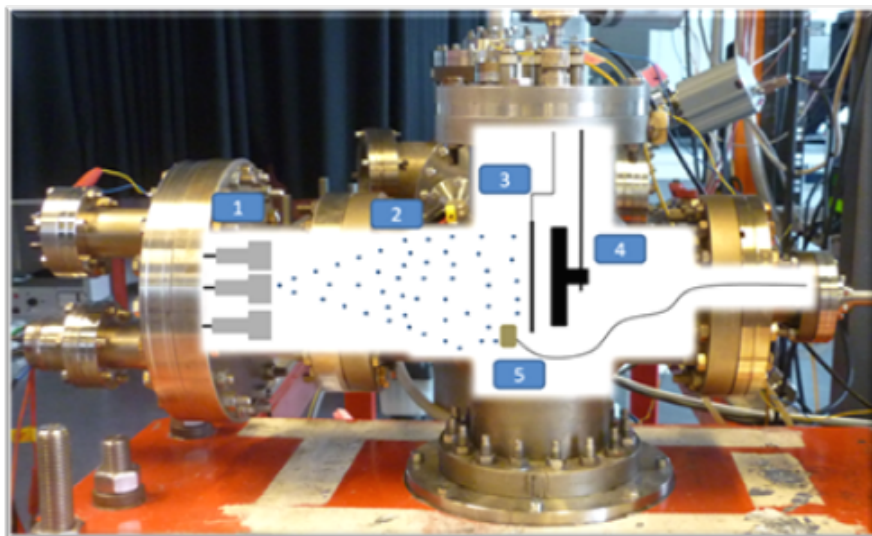


Figure 2.9: Schematic diagram of the OMBD setup: (1) Knudsen cells; (2) formed beam; (3) shutter; (4) heated substrate holder; (5) microbalance crystal holder.(Image by Arkadiusz Goszczak)

quartz crystal by the LabVIEW software module, which calculated the thickness and deposition rate.

Basing on previous design of Knudsen cells fabricated in-house at NanoSYD, the new cells were designed to overcome the limitations of the previous. The interchangeable, 500mm³ vessel is closed with standard swagelock system cap with orifice of desired diameter, and is mounted on hollow threaded rod of low thermal conductivity. Thermocouple temperature sensor is placed at the end of the threaded rod, so the minimal distance from the sensor to vessel interior assures minimal measurement inaccuracy. 40cm of 0,5Ωcm⁻¹ thermocoax cable was wind around vessel to provide up to 50W of heating power required for reaching sufficient temperatures of α-6T and C₆₀ sublimation [126, 127]. Additionally, the compact size of devices was required, as the mounting space is limited to 6' flange, and three cells were designed to occupy the system: buckminsterfullerene, α-sexithiophene, and bathocuproine. The design drawing and image of mounted cells can be found in figure2.10. The four electrical terminals of each cell (two for powering the thermocoax and two for the thermocouple sensor) were connected to manual selector switch, which facilitated the connection of chosen cell with temperature sensing circuit (500x J-type thermocouple amplifier) and programmable power

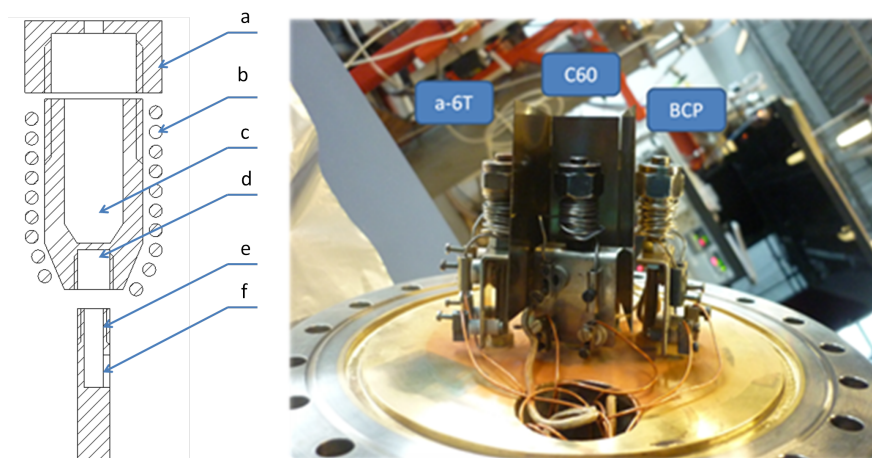


Figure 2.10: The design sketch and the image of three mounted in-house built Knudsen cells. a) Swagelock cap with drilled nozzle; b) thermocoax heating wire spiral; c) material vessel; d) placement of thermocouple sensor; e) hollow threaded rod for holding the cell and providing an access for thermocouple wire; f) opening for thermocouple wire (image by Arkadiusz Goszczak).

supply (Delta Electronica ES075). Electrical diagram of OMBD setup is presented in figure 2.11.

The sample holder was made of 2.5mm thick copper sheets, as one of the main requirements for the holder, was high heat conductivity in order to assert uniform temperature distribution across the whole area. 30cm of $0,05\Omega cm^{-1}$ thermocoax cable was sandwiched between two 85mm x 35mm copper plates to provide 30W of heating power, while supplied with 2A DC current. Thermocouple temperature sensor was attached on the surface of the bottom plate, which, with assumption of symmetric heat distribution, assured that the measured temperature was very close to the actual temperature at the holder surface facing Knudsen cells. The finite element method simulations were conducted in order to validate the heat distribution over a sample, as well as the temperature correlation between actual measurement point and the point of interest. The results of the simulation performed in COMSOL software is presented in figure 2.12. As the deposition of active layers needed to be restricted to well defined region, construction of sample cradle and a mask was required. Sample cradle's purpose was to fix the sample in place and align it with holder. Then, applied shadow mask was exposing precisely defined area to the molecular beam. The shutter

2.2. FABRICATION PROCESS

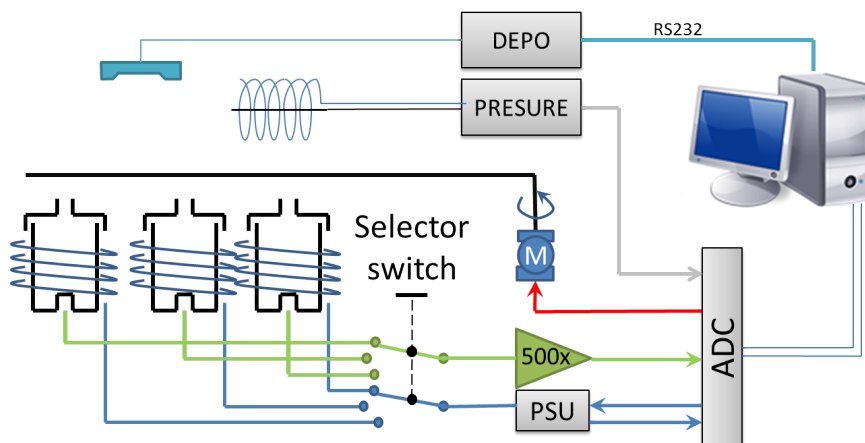


Figure 2.11: Electrical connection diagram of the OMBD setup

was actuated by servomotor on the atmospheric side through the rotational feedthrough. The sample holder and shutter were mounted on detachable flange which allows for easy replacement of the substrates. The image of detachable flange is presented in figure 2.13.

The shutter was placed in the system, so, while shut, it shadows the sample holder from incident molecular beam and still exposing the microbalance crystal. It is mounted on the shaft of o-ring sealed rotary motion feedthrough, which was actuated by a servomotor on the atmospheric pressure side.

The system is evacuated with turbo- (Pfeiffer Vacuum TMU 261 P) in series with rough-pump (Edwards RV12), and vented with Ar class 5.0 through an automatic valve controlled by turbo pump control unit, which opens it when angular frequency of the turbine drops below the set value (500Hz). The nominal frequency of the turbo pump is set to 1000Hz.

In order to provide convenient monitoring and logging of deposition processes, a dedicated software was designed in LabVIEW environment. The software displayed time charts of following parameters: layer thickness, deposition rate, deposition pressure, Knudsen cell temperature and supply current, which were stored for later revision. It also featured control of the power applied to the Knudsen cell heating thermocouple, by communication with programmable power supply, as well as was able to shut the shutter, when desired layer thickness was reached. Screen dump of the software is presented in figure 2.14.

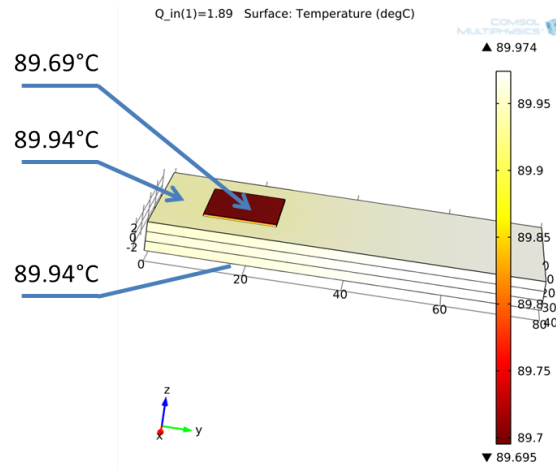


Figure 2.12: The result of FEM analysis comparing the temperature at the bottom of the sample holder (sensor placement), the temperature at the surface of the holder, and the temperature at the surface of the sample.

Deposition process

The cleaned substrates were fixed to the sample cradle and loaded into the chamber ensuring the shutter was in closed position. After introducing rough vacuum (10^{-3} mbar), the turbo pump was engaged to evacuate the system to pressures under ca. 10^{-7} mbar. When desired pressure was achieved, heating of C_{60} cell was turned on. After approximately 45min, the material in cell reached its sublimation temperature which was observed as the increase in deposition rate. When the deposition rate stabilized at desired level, the thickness monitor was reset and the shutter was opened to allow the material to reach the substrate. After reaching desired nominal thickness of deposited material, the shutter was automatically shut, and the power was switched off. Oven selector switch was set to the α -sexithiophene, and the heating of Knudsen cell and substrate holder were turned on. The substrate holder temperature was kept constant in 30°C - 170°C range by a thermostat. After ca. 30min, the sublimation temperature of α -6T was reached, the thickness monitor was reset and the shutter was opened. After reaching desired nominal thickness of deposited material, the shutter was automatically shut, and the power was switched off.

After the deposition processes, vacuum chamber was vented with class 5.0 Ar, and the substrate was let to cool down below 45°C without exposing to the ambient air.

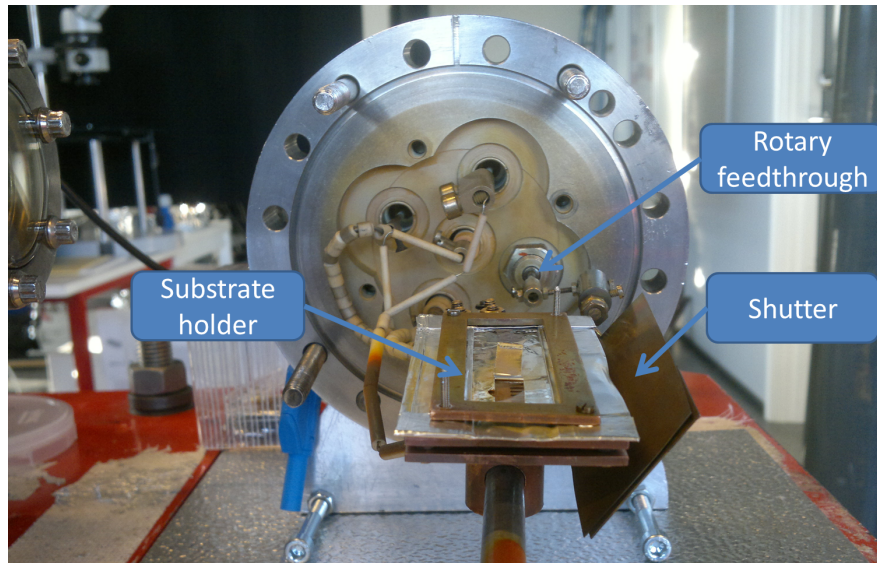


Figure 2.13: The image of detachable flange with substrate holder.

2.2.3 Spin-coating

Defining device area

Weakly adhesive masking tape was used to restrict area where PEDOT:PSS blend was to be spin in order to obtain 1mm^2 solar cell area. The substrate was positioned on the smooth surface with lines of 1mm pitch, so the top of the electrodes coincide with one of the marker lines. 7mm x 30mm stripe of masking tape was stretched on the fixture which kept it 1mm above the surface, and the fixture was positioned to collocate the edge of tape with 1mm marker. Then, the tape was firmly pressed against the sample with the rubber stamp. Such prepared substrate was moved into N_2 filled dry glove box.

Spin-coating of PEDOT:PSS blend

Laurell WS-400-6NPP-Lite spin processor operating in N_2 dry glovebox was used to apply uniform layer of PEDOT:PSS onto the exposed area of the substrate. The sample was positioned centrally on the chuck and immobilized by vacuum holder. $25\mu\text{l}$ of PEDOT:PSS blend was applied and spun at 1000rpm for 45s which result in 150nm

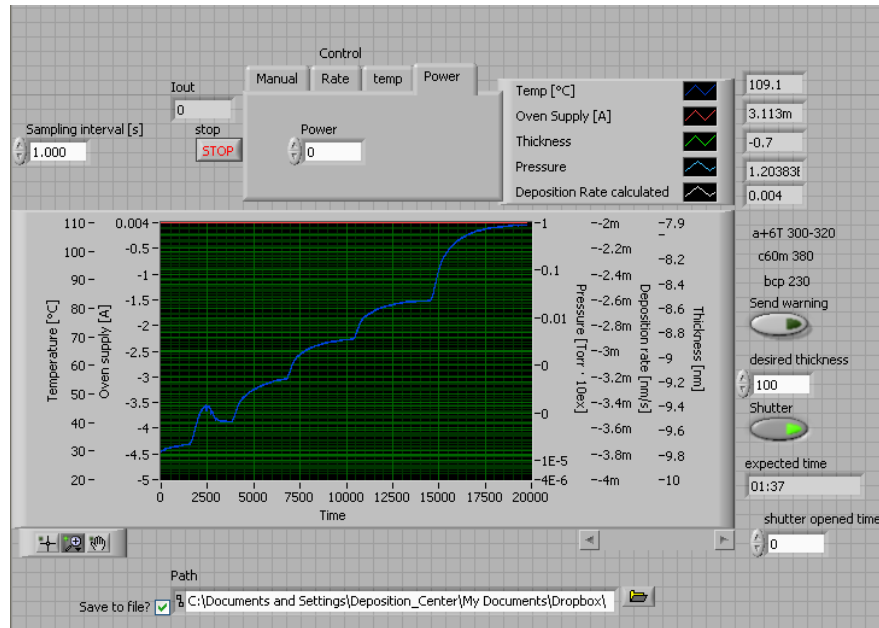


Figure 2.14: The screen dump of OMBD deposition setup control software written in LabVIEW

thick layer. Directly after spinning, the masking tape was removed and the sample was annealed on hotplate at 90°C for 30 min.

Encapsulation

The sample was let to cool down for 5 min, and new masking tape stripe was applied to cover approx. last 4 mm of the electrodes, to protect the contact areas of the device. When the substrate was fixed on the spin processor chuck, a layer of DELO katiobond LPVE UV curable encapsulant was uniformly dispensed over the exposed area of the device and spun at 4000rpm for 45s. The masking tape was removed instantly after spinning and the substrate was immediately transported from the glove box to the characterization station. There, it was light soaked for 15 min with illumination of 1 sun intensity and 1.5AM spectrum to cure the encapsulant.

2.3 Characterization

2.3.1 Photovoltaic measurement setup

Solar simulator

The choice of the illumination source used for device characterization is crucial for the possibility to compare the fabricated devices' characteristics with the results of the other research groups. Due to the fact, that majority of solar cells are designed to operate under solar illumination, it seems reasonable to apply sun-like source to standardize the measurements. The extraterrestrial luminance - the amount of sunlight reaching the top of the Earth's atmosphere can be easily obtained from approximation of the sun as a black body with $\sim 5600\text{K}$ surface temperature. Nevertheless, this radiation need to pass through the atmosphere in which various compounds absorb distinct bands e.g. N_2 (10nm to 100nm) O_3 (200 nm to 310 nm) or H_2O (various bands). Due to the differences in the light path length through atmosphere for rays reaching different latitudes, the standard has emerged to assume average of 1.5 atmosphere thickness. Taking into consideration total atmospheric absorption over this distance, the spectrum of resulting light is referred to as 1.5 AM (atmospheric mass). Hence, most of reported measurements are conducted under illumination of 1 sun (1000Wm^{-2}) and 1.5AM spectrum.

In order to obtain light of such characteristics, so called light simulators are used. To produce a semi-continuous spectrum resembling the spectrum of the sun, most commonly the high pressure Xe arc bulbs are being used. Those, with dedicated filters can produce required intensity and spectrum. To assure the temporal stability of the light output, such lamps need to be powered by a radiometric power supply.

Newport 9600 solar simulator was chosen as the light source which has been used to illuminate the devices examined in this work. It is capable of providing 1 sun illumination over 2.5' diameter disc. Unfortunately, it has been observed, that it was impossible to obtain uniform light distribution over 20mm area, which was required for consistent measurements of our devices. Noticed non-uniformity will result in variation of the devices illumination, hence increasing the measurement error. In order to determine whenever before mentioned non-uniformity is acceptable or not, light distribution measurements have been performed.

Light distribution Newport 9660 reference cell was a basic tool used to determine the illumination provided by the solar simulator. Its limiting factor comes from the fact, that it had 20mm x 20mm sensing area with averaging output, while the resolution of interest was in order of 1mm. In order to overcome this issue, the reference cell was mounted on robotic arm and raster scanned 80mm x 85mm area with 1mm x 1mm mesh. It has been assumed that reference cell output is linear to a non-weighted average illumination intensity over whole (400mm²) measurement area, so the measured signal was of form:

$$U(u, v) = I(u, v) \otimes H(i, j)$$

where $U(u, v)$ is measurement matrix, $I(u, v)$ is illumination at point (u, v) , and $H(i, j)$ is 20 x 20 matrix with all elements equal to 400^{-1} .

This equation represents the mean filtering, therefore, to retrieve the original signal, the deconvolution operation needs to be performed. With help of Matlab's image processing toolbox, the original intensity distribution was restored and presented together with measured one as an overlay in the figure 2.15. Extracting the cross section from

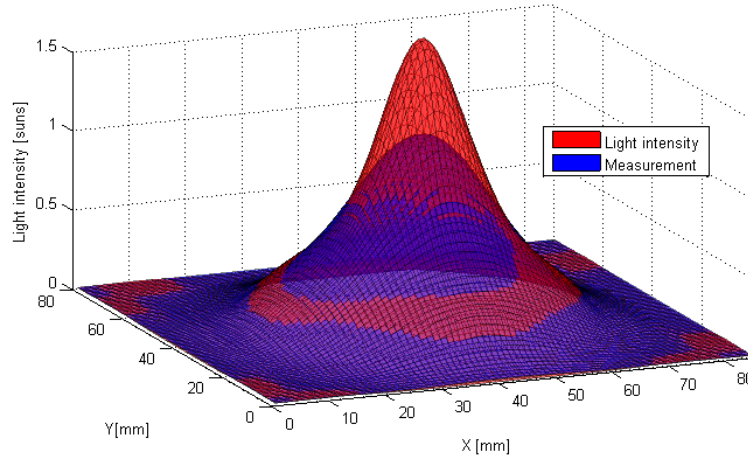


Figure 2.15: Irradiation distributions over measurement area 85mm x 80mm. The measured values are presented in blue, while the values obtained by deconvolution in red.

this data set it can be easily found that light intensity variations in order of 50% can be expected over 20mm distance (see figure 2.16), hence the measurements of solar cell devices measured on static substrate are unacceptable. Moreover non-rigid fixture

2.3. CHARACTERIZATION

between measured sample and solar simulator could result in position drift leading to even bigger errors.

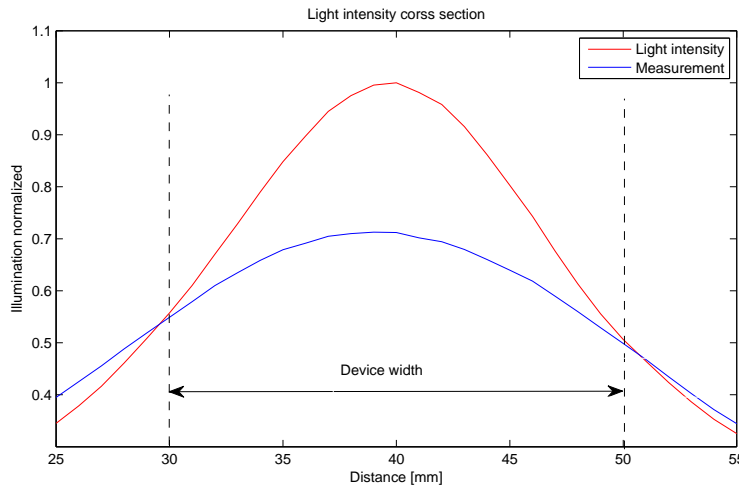


Figure 2.16: The cross section of the intensities presented in figure 2.15 through the center of the beam normalized to 1 sun for deconvoluted values.

Conclusions It has been derived from the light distribution measurements, that when the reference cell is positioned in the center of the beam, its averaging output of 0.7 sun corresponds to actual 1 sun in the beam axis.

In order to assure that all the measurements will be performed under the same illumination, the translational stage has been introduced. First, the stage was aligned with the beam in order to place it exactly in its center. The sample was fixed in the holder and the electrical connections to all devices were established simultaneously by means of ZIF connector. Then, prior to any measurement, the stage was moved in order to locate the device to be measured in the axis of the beam emerging from the solar simulator.

Source meter

In order to measure the basic electrical properties of fabricated devices, I-V characteristics have to be taken. Keithley 2400 source meter has been used as a basic tool for all characterizations conducted within this project. All measurements were performed

in 4-terminal configuration in order to minimize the influence of contact resistances, as well as to suppress noise in measurements of low currents. The source meter was connected to the device under test (DUT) via 4-channel, 7-way reed relay multiplexer, which was controlled through Keithley 2400 digital outputs. One of those outputs has also controlled a servo driver, which was responsible for shutter operation. The driver could be also set in manual mode to open and close shutter without control signal from the source meter. The schematic diagram of test station electrical connections is presented in figure 2.17.

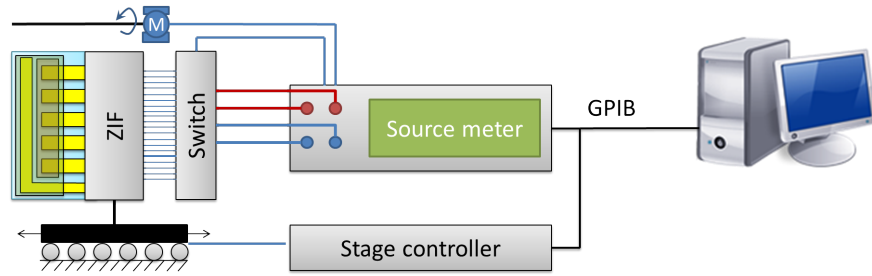


Figure 2.17: Connection diagram of the test station

Test cradle

In order to facilitate before mentioned requirements for valid measurement such as positioning DUT in the light beam axis and stable electrical connection, the test cradle has been designed and assembled. It consists of three parts: the base which allowed proper orientation of cradle with respect to light beam, the translational stage (Melles Griot Nanostep 1) which aligned individual DUTs, and the substrate fixture, which provided electrical connections between DUTs and multiplexer. The fixture consist of 40 way 0.5mm pitch ZIF flat ribbon cable and 14 way gold-pin connector mounted on PCB with interconnections diagram presented in figure 2.18. Such a design asserted, that there will always be at least two points of electrical contact to each electrode, and each of them will be connected to separate channel in 4-terminal configuration.

Software

The I-V measurement was performed from the level of LabVIEW software. The application directly controlled the translational stage as well as the source meter, while

2.3. CHARACTERIZATION

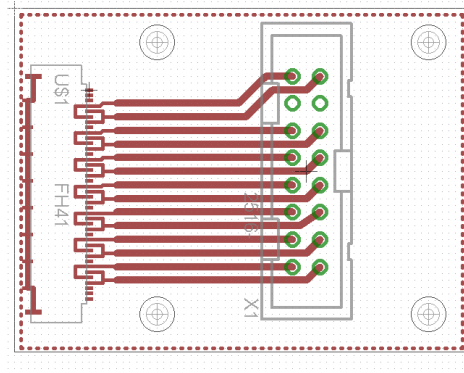


Figure 2.18: PCB design for ZIF connector.

the multiplexer and shutter were operated through the source meter's digital outputs. Measurement was performed sequentially for each DUT selected for characterization, and each cycle consisted of five phases: alignment of selected DUT to the optical axis of solar simulator, I-V measurement under dark conditions, I-V measurement under light conditions (both measurements conditional, and with tunable scan range and number of intermediate steps), V_{OC} measurement, and I_{SC} measurement. After each measurement, the raw data consisting measured currents was converted into current density by dividing its value by provided area of the cell – by default 1mm^2 . Then the separate measurement file was written in desired storage location. The measurements could be looped in order to perform long term measurements in light soaking, as well as in darkness conditions in between the cycles. The screen dump of the application is presented in figure2.19.

Measurement

The voltage bias range for the measurements was set to 0V-0.5V, as none of fabricated devices have exhibited V_{OC} higher than 0.45V. As soon as the substrate with devices was mounted in the fixture, the repeatable measurement was started in order to obtain uniform illumination of all devices while curing the encapsulant (due to movement of stage). Even though the preceding, as well as following measurements were stored for possible temporal evolution examination, only the measurements performed after 15 minutes from the start of light soaking were taken into consideration for the sake of

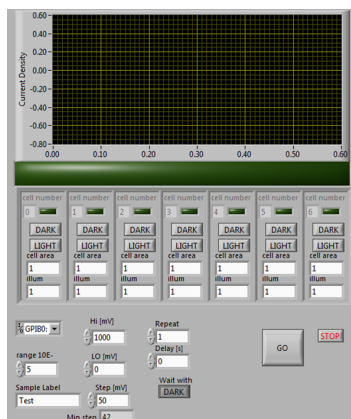


Figure 2.19: Screen dump of solar station measurement software.

this dissertation. After the measurement the substrate was removed from the fixture, and stored in sample box in dark and dry conditions for possible further inspection.

Data processing

In order to present the measurement data, the fill factor and power conversion efficiency were calculated using VBA script for each of chosen measurement files. Chosen data sets were also plotted in separate figures, as well as in one common plot; average values of V_{OC} , J_{SC} , FF, PCE and their standard deviations were presented in summery table together with parameter values obtained from individual devices. The exemplary output of data processing scripts is shown in figure 2.20. The reported values of the parameters are the arithmetic averages of the values obtained from all six devices on one substrate if no outliers were identified.

2.3.2 Epifluorescence imaging

Fabricated structures were examined with epifluorescence imaging at various stages during fabrication, but mostly directly after α -6T deposition. Nikon Eclipse ME-600 microscope with Hg lamp (peak wavelength around 365nm), 50x 0.75NA, or 100x 0.9NA objectives, and CCD camera (Infinity 2) was used to obtain the micrographs. 330nm-380nm excitation, 400 dichroic, and 420 longpass detection filters were normally used, but, in cases when fully fabricated devices were examined, FITC system (460nm-

2.3. CHARACTERIZATION

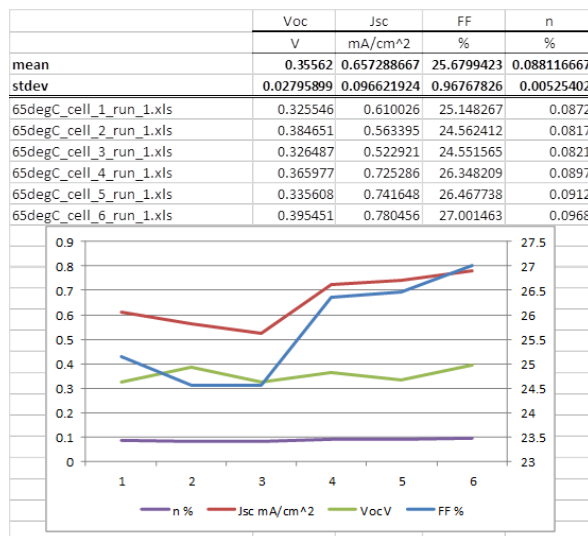


Figure 2.20: Exemplary output of data processing scripts.

495nm excitation 505 dichroic, and 515nm-555nm detection) was used to filter out intense blue fluorescence from the encapsulant excited under UV exposure.

Epifluorescence microscopy utilizes the phenomenon of fluorescence, which is exhibited by many materials. Fluorescence occurs, when excited molecule relaxes to the ground state by an emission of a photon. Usually, the molecule emits the photon of lower energy, then one used to its excitation, due to thermal losses in the time interval between photon absorption and emission. The energetic diagram of this phenomenon, together with microscopic setup is presented in figure 2.21. Hg I line (365.4nm) light is produced in high pressure arc bulb, and is collimated by a lens. After passing the bank of neutral density filters the excitation line is selected by 330-380nm bandpass excitation filter and is reflected by the dichroic (400nm) mirror towards the investigated specimen. Fluorescent light emitted by specimen is Stokes shifted, therefore it is passed through the dichroic mirror, and is subsequently filtered by 420nm long pass detection filter.

2.3.3 Epifluorescence polarimetry

Together with introduction of analyzer and rotational sample stage to epifluorescence setup, the fluorescence polarimetry could be performed.

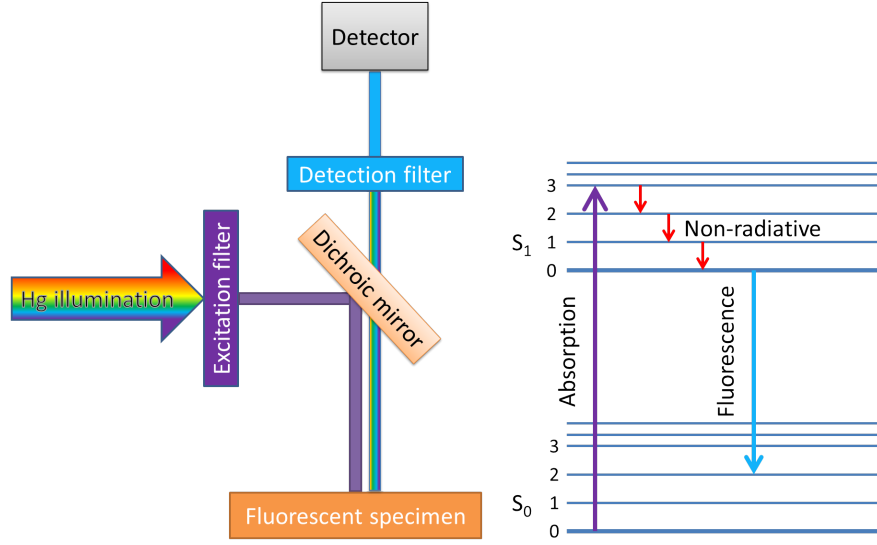


Figure 2.21: Schematic diagram of epifluorescence imaging, together with Jablonski diagram of fluorescence process.

Four epifluorescence images of the sample being rotated by 0° , 45° , 90° and 135° with respect to the analyzer axis at a magnification of 50X were taken. The images were digitally rotated to a common orientation and the region present on all images was selected, resulting in a stack of images having their corresponding pixels aligned.

For each pixel, the Maul's law is used to interpolate the intensity values for each corresponding pixel throughout taken images. Comparing the second harmonic of the Furrier transform of each pixel intensity versus angle, with the threshold value, provides an easy way to detect the areas of the image from which the polarized light is emitted which is believed to originate from fiber structures[128]. For each pixel belonging to a fiber, the angle of maximum fluorescence φ_0 was calculated[129], and the local structure tensor angle ϑ was identified[130]. Since for 6T the transition dipole overlays the long molecular axis within 3° [20, 131], the angle φ_0 indicates the orientation of the long molecular axis, while ϑ indicates the local orientation of the nanofiber. Then, the $\vartheta - \varphi_0$ difference represents the local orientation of the long molecular axis with respect to the long fiber axis $-\beta_{\text{mol}}$. Dedicated software written by dr Frank Balzer automatically conducts the image operations and returns the histogram of β_{mol} across area, where the fibers were detected.

2.3.4 X-ray diffractometry

α -6T films, together with underlying system were investigated with Phillips X'pert X-ray diffractometry (XRD) setup, with Cr K_α source ($\lambda = 2.291\text{\AA}$) monochromatised at the secondary side with a flat graphite monochromator, in Bragg-Brentano $\theta - 2\theta$ configuration. $\theta - 2\theta$ scans were taken from $4^\circ - 62^\circ$ range, while rocking curves were measured in $\pm 16^\circ$ neighborhood of strongest peak. In Bragg-Brentano $\theta - 2\theta$ configuration the x-ray source, analyzed sample and detector are kept positioned according to specular reflection condition with varying incident angle (see figure on this page). In case of ordered layers will occur in the sample, there will exist an constructive

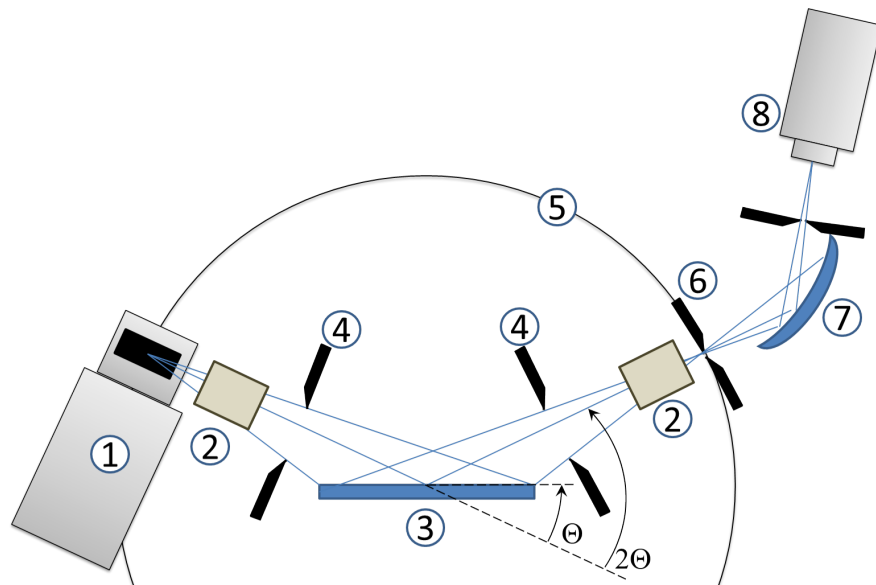


Figure 2.22: Bragg-Brentano diffractometry configuration: (1) X-ray source; (2) Soller slits; (3) analyzed sample; (4) apertures; (5) goniometer circle; (6) receiving slit; (7) monochromator; (8) detector.

interference at particular angles which is described by Bragg's law:

$$n\lambda = 2d \sin \frac{2\theta}{2}$$

where n is an integer, λ is incident light wavelength, and θ is incidence angle. The principle of Bragg's law and diffractometer schematics are illustrated in 2.23.

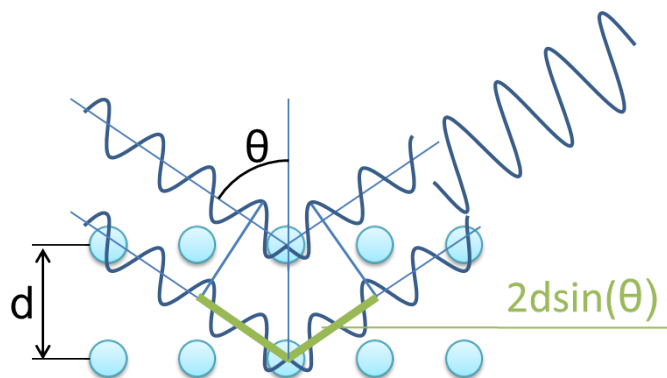


Figure 2.23: Illustration of Bragg's law. If a difference in light paths reflected from subsequent crystalline layers is equal to $n\lambda$, a constructive interference occurs and the Bragg peak is observed.

Scanning of reflection angle while recording the intensity of the x-rays reaching the detector results in diffraction pattern. Each crystalline configuration has its unique pattern, which depends on the unit cell dimensions, therefore it is a powerful method for material characterization and crystallography.

Another scanning mode results in so called rocking curves. When the source of the X-rays, the sample, and the detector are positioned in specular reflection configuration, and the maximum of the intensity peak of interest is reached, the sample can be rotated around the axis defined by the crossing of ray plane and sample surface. Rocking curve provides

an information about the mosaicity of the sample i.e. the mutual misalignment of the crystalline sites with respect to each other. The smaller full-width-at-half-maximum (FWHM) of obtained peak, the individual crystalline sites are better aligned - the mosaicity is low.

The XRD measurements were performed at Institute of Solid State Physics of Graz University of Technology under supervision of Roland Resel.

2.3.5 Atomic Force Microscopy

Atomic force microscopy is an imaging technique, which exploits the phenomenon of interplay of attractive and repulsive forces in the vicinity of the surface. The cantilever equipped with sharp tip at the end is excited in oscillation and approached to the

surface until desired amplitude damping (caused by the force repulsing the tip from the surface) will be reached. The deflection, and by the same means the amplitude of the vibration, is measured by the optical method. The laser beam is directed at the cantilever tip, from which it is reflected. The reflected beam hit the center of the quadrature sensor consisting of four photo elements. Even though the beam size is smaller than individual sensors, the difference between the responses of the higher and the lower sensors, divided by their sum provides accurate information about the position of the light spot on the sensor.

If then the amplitude of cantilever oscillations will be controlled by the closed loop PID feedback system, the driving signal value will be corresponding to the height deviation from the equilibrium position. Therefore, when the tip is scanned across textured surface and the feedback loop keeps the tip oscillation amplitude constant, the driving signal is directly coupled with the height of the sample.

AFM scans were performed over areas of hundreds of nanometers (in case of high resolution scans) to few square micrometers, and the quality of the measurement depends strongly only on the measurement parameters like scan size, tip velocity (below $1\mu\text{ms}^{-1}$) and number of lines in scan (256 or 512), but also on the settings of the closed loop PID controller gains. AFM measurements performed in this work were done with usage of Veeco Dimension 3100 system.

2.4 Experiments

The main topic of this dissertation is to investigate the variety of structures, which α -6T deposited on C_{60} can take in slow deposition rate OMBD process, with variable substrate temperature during deposition, and the effect of application of those structures in solar cell on its performance parameters. Therefore two series of experiments were conducted.

2.4.1 Growth of α -sexithiophene nanostructures

In order to ensure that the temperature dependent growth of α -6T is not caused by the changes in the underlying layer, the preliminary experiments were conducted to determine the morphological changes of C_{60} film at elevated temperatures. Next, the α -6T

material used for depositions was validated, and investigation of α -6T nanostructures formation was conducted.

C₆₀ temperature independence

The substrates were prepared according to recipe described in section 2.2.1, with Al as an electrode metal. Subsequently 30nm of C₆₀ was deposited as presented in section 2.2.2. One sample was first *in-situ* annealed at 150°C for 120min (which corresponds to deposition time and conditions of α -6T) and then withdrawn from OMBD setup, while the other was removed immediately after the deposition. Both samples were analyzed with AFM (Veeco Dimension 3100).

α -sexithiophene material validation

In order to check if the purchased material was indeed the α -6T, its photo-luminescence spectra has been validated against reported in literature. Blank BK7 glass substrates were pre-cleaned by ultrasonic bath in acetone for 5 min, rinsed with isopropyl alcohol and deionized water, blow-dried with N₂, and exposed to 130W RF glow discharge oxygen plasma for 90s. 50nm layer of α -6T was deposited at room temperature substrate in the OMBD system under pressure below $5 \cdot 10^{-7}$ mbar, at 0.1 Å/s deposition rate. The sample was investigated by epifluorescence microscopy system with fiber coupled spectroscopy (Maya2000) mounted instead of the camera.

α -sexithiophene nanostructures vs. temperature

Due to the fact, that analyzed structures are going to be implemented in solar cell devices, the required nominal thickness of the α -sexithiophene should, according to device optimization experiments, be close to 30nm. Contrary, for the crystallinity studies, thickness of the deposited layer should not be thinner than 100nm. In order to address this contradiction two series of samples were prepared with two different nominal thicknesses of α -6T: 30nm for direct analysis of structures to be employed in organic solar cells, and 100nm for XRD measurements.

For the morphological studies, substrates were prepared as in previous case (section 2.2.1) and both organic layers were deposited (section 2.2.2) with a constant temperature of the substrate during the deposition of α -6T ranging between 30°C-170°C and

2.4. EXPERIMENTS

α -6T nominal thickness equal to 30nm. Devices were analyzed with AFM, as well as with epifluorescence microscopy imaging and epifluorescence polarimetry.

For sake of XRD measurements, thicker layers of α -6T were required. Devices were prepared with the same recipe as previously, changing only α -6T thickness to 100nm. Besides the XRD, the AFM, the epifluorescence microscopy imaging and epifluorescence polarimetry analysis have been performed in order to characterize the morphology, as well as the internal structure.

2.4.2 Implementation of α -sexithiophene nanostructures in solar cells

Implementation of the α -6T films in solar cells requires a deposition of the subsequent layers on the active materials. Therefore, preliminary experiments are needed in order to determine if the top electrode as well as the encapsulant spin-coating does not influence the morphology of underlying layer.

α -sexithiophene nanostructures integration with spin-coating

The substrates were prepared according to recipe described in section 2.2.1, with Au as electrode metal, both organic layers were deposited (section 2.2.2) and top electrode and encapsulant were applied by spin-coating (section 2.2.3). Epifluorescence microscopy images were taken before and after spinning process.

Impact of the substrate temperature during α -6T deposition on performance of solar cell

The substrates were prepared as in previous case (section 2.2.1) and both organic layers were deposited (section 2.2.2) with a constant temperature of the substrate during the deposition of α -6T ranging between 300°C-170°C. The top electrode and encapsulant were applied by spin-coating (section 2.2.3). Devices were characterized with photovoltaic measurement setup (section 2.3.1) and then epifluorescence microscopy images were taken afterward.

3 Results

3.1 Growth of α -sexithiophene nanostructures

3.1.1 C₆₀ temperature independence

The thermal stability of the C₆₀ layer is of crucial importance for the generated interface and the morphological analysis of the subsequent layers, as their deposition involves heating of the sample to temperatures in order of 150°C for periods in order of one hour. To perform a comparative study, two C₆₀ thin-film samples were prepared: one was withdrawn from the OMBD setup just after the deposition process, while the other was post annealed in the chamber at 150°C for 1h without breaking the vacuum. The 3D representation of the 5 μ m x 5 μ m AFM scans of the 30nm C₆₀ layers on top of the electrode for as deposited and post annealed samples, are presented in figure 3.1 a) and b) respectively. As the AFM scans indicate, there is no significant difference

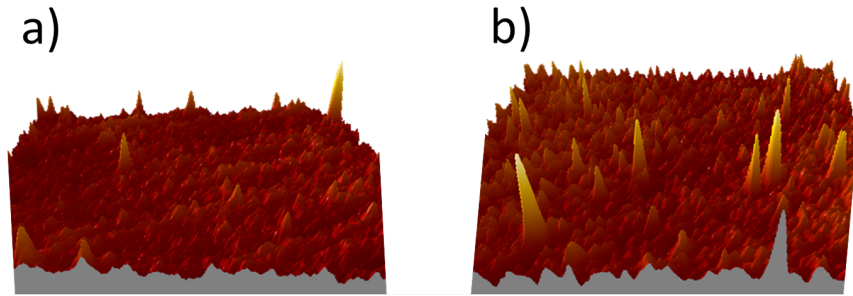


Figure 3.1: 3D representations of thin-film (30nm) C₆₀ layers: a) as deposited; b) post annealed at 150° for 1h. (z-scale magnified)

in the surface of both samples. In order to compare the quality of the surface morphology, the roughness analysis was performed by SPIP software and summarized in table 3.1 , where S_a is the average roughness, S_q is the root mean square roughness,

3.1. GROWTH OF α -SEXITHIOPHENE NANOSTRUCTURES

	S_a [nm]	S_q [nm]	S_y [nm]	S_z [nm]
as deposited	1,09	1,47	16,20	21,44
post annealed	1,21	1,63	24,90	20,60

Table 3.1: Roughness comparison of C_{60} film as deposited and post annealed at 150°C

S_y is peak-to peak value, and S_z is ten point height. The numerical values of the parameters increased only slightly - below 20%. the only significant increase is in the value of peak-to-peak value, but the AFM image shows the presence of high features only in few spots, therefore it can be considered as negligible. This conclusion is even strengthened by the observation of the fall in ten point height which is defined as the average height of the five highest local maximums plus the average height of the five lowest local minimums, which indicates that average outliers lay closer to the mean level in the annealed sample.

The ellipsometry measurements were performed to identify the nature of the fabricated C_{60} layers. The measurements, despite being performed according to the methods used for measurements of C_{60} crystals found in the literature[132, 133], did not converged even when the thickness of the C_{60} layer was known from measurements of step height scans by AFM or profilometer (Veeco Dektak 150).

Summary

It can be concluded, that C_{60} forms highly polycrystalline film on TiO_x , which morphology is not significantly affected by annealing. It complies with other works, which describe remarkable effort required to obtain large domains of crystalline buckminsterfullerene films[134, 135]. The surface roughness of both as deposited, and post annealed layers of C_{60} is in order of 1nm and can be considered smooth for subsequent layers base. The individual defects are not higher than the thickness of subsequent layers.

3.1.2 α -sexithiophene material validation

The fluorescence spectra of the examined sample is presented in figure 3.2. Four Gaussian peaks have been fit to the spectra, which had following peak positions: 1.75eV, 1.94eV, 2.09eV, and 2.2 eV. As the identified values are close to found in literature:

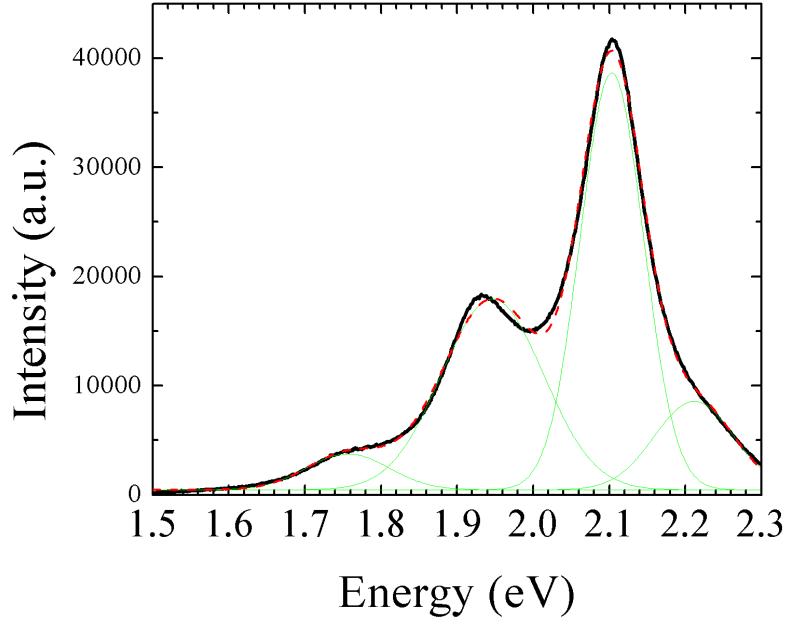


Figure 3.2: Photo luminescence spectra of deposited α -6T with fitted Gaussian peaks (1.74eV, 1.91eV, 2.09eV and 2.17eV).

1.74eV, 1.91eV, 2.09eV and 2.17eV[136, 137], the material was validated as sexithiophene.

3.1.3 Morphological studies

In order to be able to include X-ray diffractometry data to draw conclusions about the impact of substrate temperature during deposition on the crystallinity of obtained nanostructures, two parallel experiments were conducted. One, where the nominal thickness of the deposited α -sexithiophene was 100nm, which was indicated as minimal recommended thickness to perform X-ray diffractometry measurements, and the second one with nominal thickness equal to 30nm, which was the thickness of material to be used in solar cells devices according to calibration measurements (see section 3.2.2).

In both cases, the series of samples were prepared as described in section 2.4.1, and then the epifluorescence micrographs, as well as AFM scans were taken. The resulting series of epifluorescence images, together with AFM micrographs are presented in

3.1. GROWTH OF α -SEXITHIOPHENE NANOSTRUCTURES

figures 3.3 and 3.10 for the thin, and thick samples, respectively. The results of each series will be discussed separately.

30nm α -6T on C_{60} layers

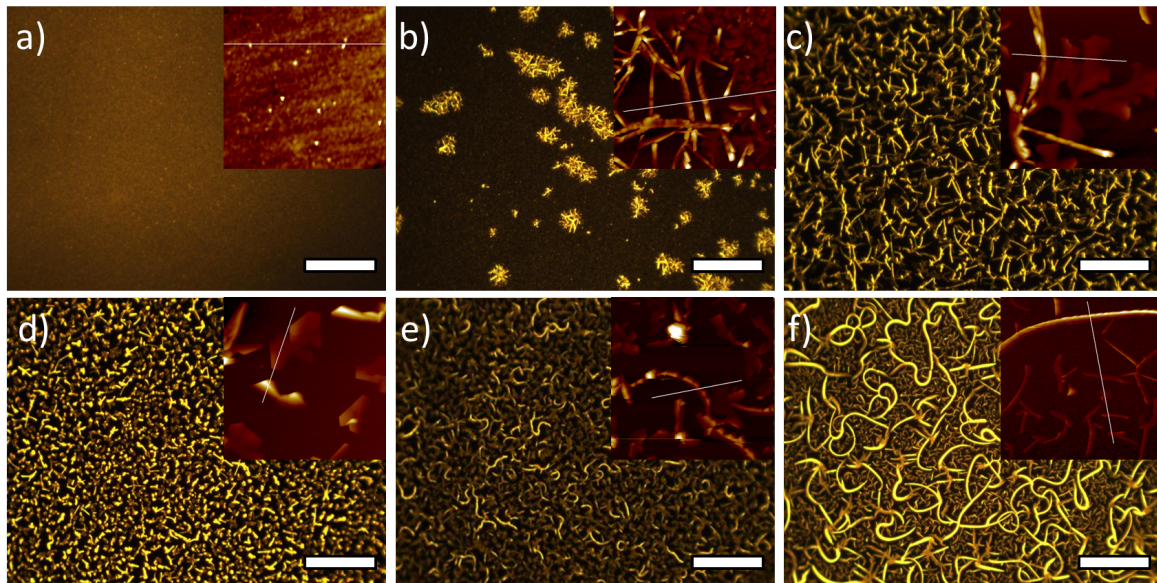


Figure 3.3: Epifluorescence micrographs of 30nm α -6T thin-films on Buckminsterfullerene fabricated at different substrate temperatures during deposition: room temperature, 90°C, 110°C, 120°C 150°C, 170°C, a) to f), respectively. The insets present 5 μ m x 5 μ m AFM scans of the respective samples with height ranges of 35nm, 270nm, 360nm, 600nm, 800nm, 700nm, respectively. The scale bar is 20 μ m

30nm thin-films fabricated at room temperature

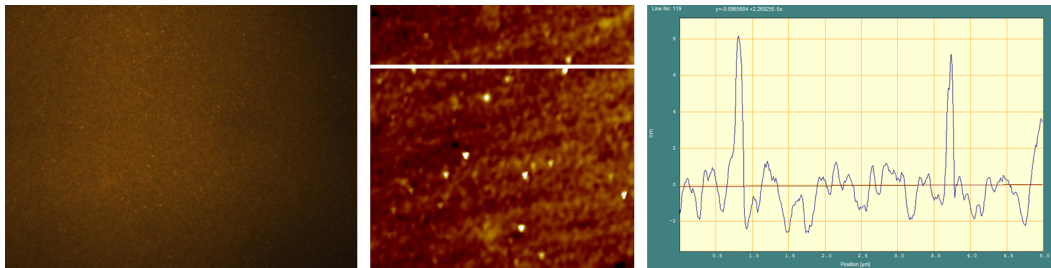


Figure 3.4: Epifluorescence ($130\mu\text{m} \times 97\mu\text{m}$) and AFM ($5\mu\text{m} \times 5\mu\text{m}$) micrographs of sample fabricated at room temperature. White line in AFM micrograph indicate the $5\mu\text{m}$ line scan area with height range of 9nm.

When substrate was kept at room temperature during deposition of α -sexithiophene, rough continuous film with sparse nanoscale clusters are observed in AFM scan. The clusters, which do not exceed 10nm in height, are uniformly distributed and the roughness of the film was measured as $S_q=1.8\text{nm}$. It indicates predominant layer by layer growth, where only small clusters are formed. The epifluorescence micrograph presents uniform film with very small grains, and when the polarization analyzer is introduced into microscopy system, its rotation results in subtle flickering of the image indicating that the film is polycrystalline, where the crystalline sites are too small to be resolved by an optical method.

30nm thin-films fabricated at 90°C

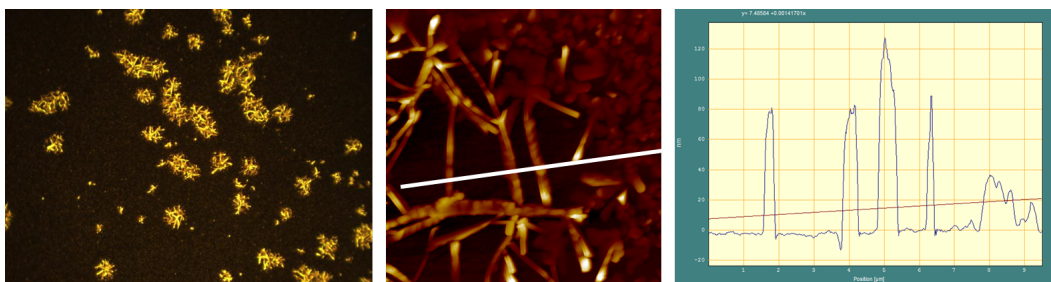


Figure 3.5: Epifluorescence ($130\mu\text{m} \times 97\mu\text{m}$) and AFM ($10\mu\text{m} \times 10\mu\text{m}$) micrographs of sample fabricated at 90°C . White line in AFM micrograph indicate the $95\mu\text{m}$ line scan area with height range of 140nm.

3.1. GROWTH OF α -SEXITHIOPHENE NANOSTRUCTURES

Substrate holder temperature set to 90°C during the deposition of α -sexithiophene results in formation of 1-20 μm regions consisting of a mesh of needle like structures at number of nucleation points, which are surrounded by a rough film. Once again, the rotation of a polarization analyzer reveals the crystalline nature of observed formations, while the amplitude of intensity variation, in comparison to the surrounding areas, can indicate that they consist of lying molecules rather than standing. This phenomenon is caused mostly by the orientation of the transition dipole in the α -sexithiophene molecule, which is tilted just 3° from the long molecular axis[20, 131]. Therefore, lying molecules not only can easily absorb the incoming light, but also the emitted light will be predominantly directed perpendicular to the substrate. It stays in contrast to formations consisting of standing molecules, which will not only absorb significantly less light due to nearly right angle between transition dipole and incoming electric field, but also emission occurs mostly in directions coplanar with the substrate. The structures seem to emerge from the nucleation centers and cover virtually circular areas. There exist a depletion zone in the vicinity of fiber-like structures, where significantly lower intensity of fluorescent light is observed. Such behavior is expected in Stranski-Krastanov growth mode. AFM scans reveal the heights of the fibers to be in range of 60-130nm.

30nm thin-films fabricated at 110°C

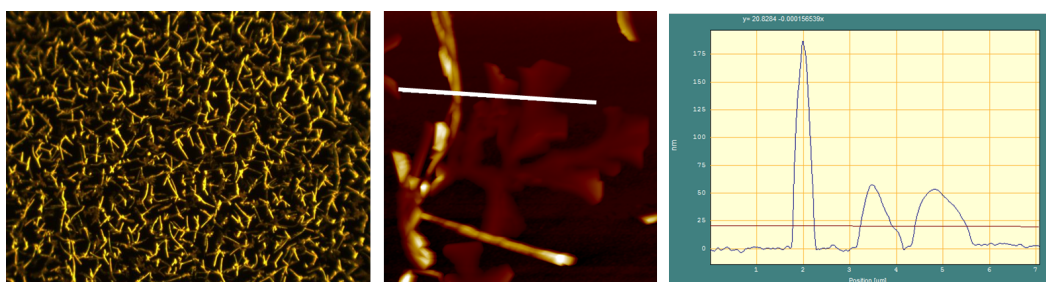


Figure 3.6: Epifluorescence (130 μm x 97 μm) and AFM (10 μm x 10 μm) micrographs of sample fabricated at 110°C. White line in AFM micrograph indicate the 75 μm line scan area with the height range of 200nm.

If the temperature of the substrate holder during the deposition of α -sexithiophene will be kept at 110°C, the whole surface is uniformly covered with dense mesh of mixed fibers

and dendritic structures. Significant difference in the observed fluorescence intensity of fiber like and dendritic structures implies, that fibers consist of lying molecules[99], while dendritic structures consist of standing ones[108]. Nevertheless, the observed amplitude of fluorescence from dendritic formations is higher than expected. However, this can be explained by the fact, that mostly the dendritic shapes are adjacent to the fibers, so injection of light from highly absorbing and fluorescent fibers to the dendritic structures may occur. Moreover, while rotating the polarization analyzer, one can identify few domains within one dendritic structure, for which the fluorescence intensities are phase shifted. It indicates that dendritic formations consist of few crystalline domains.

AFM scans of the structures show that fiber like structures height and width are in range of 200nm, while the dendritic structures grow just until 50-60nm and form smooth slopes.

30nm thin-films fabricated at 120°C

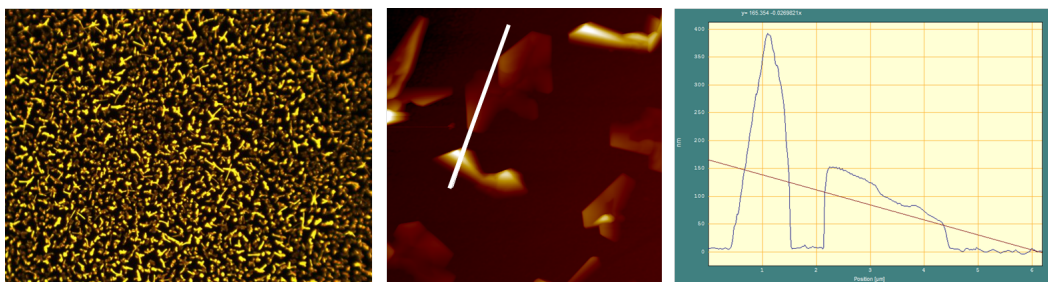


Figure 3.7: Epifluorescence ($130\mu\text{m} \times 97\mu\text{m}$) and AFM ($10\mu\text{m} \times 10\mu\text{m}$) micrographs of sample fabricated at 120°C. White line in AFM micrograph indicate the $6\mu\text{m}$ line scan area with the height range of 400nm.

At 120°C of the substrate holder temperature during the deposition of α -sexithiophene, the new structures emerge. The area is covered by individual formations of mostly polygonal shape, but also significant number of elongated, and fiber like structures are present. Even though all structures exhibit fluorescence and Malus law governed intensity variations while polarization analyzer is rotated, there is remarkable intensity difference between bright elongated and fiber like structures, and dim polygons. Though, there are numerous polygon like structures with areas of strong fluorescence.

3.1. GROWTH OF α -SEXITHIOPHENE NANOSTRUCTURES

AFM scans of the sample reveals that polygon like structures usually consist of single slope crystal face which terminates abruptly. Similar structures formed by α -sexithiophene were also recently found by Simbrunner et al.[51], where it was shown, that such crystals can grow as tilted lamellar plate with defined tilt angle with void space underneath. Even though only 67° tilt angle of lamellar structure with respect to the substrate was identified, the reason that number of different tilt angles (21.3° , 24.5° , 32.5° , 36° , 43°) observed here can lay in the fact, that Simbrunner performs epitaxial experiments by deposition over para-hexaphenylene (p6P) crystals, while here the substrate is amorphous buckminsterfullerene.

30nm thin-films fabricated at 150°C

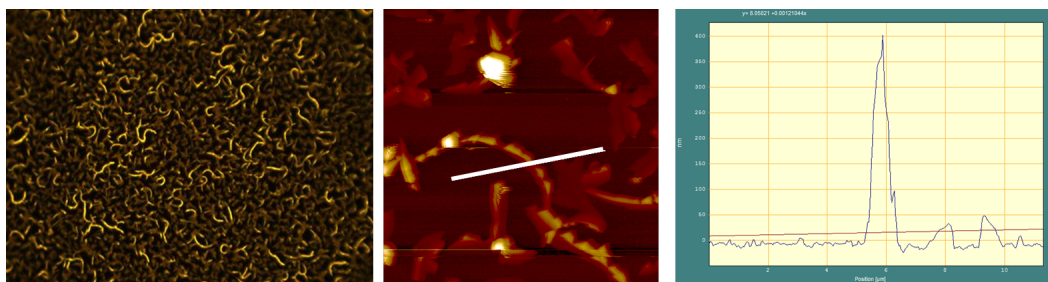


Figure 3.8: Epifluorescence ($130\mu\text{m} \times 97\mu\text{m}$) and AFM ($20\mu\text{m} \times 20\mu\text{m}$) micrographs of sample fabricated at 150°C . White line in AFM micrograph indicate the $11\mu\text{m}$ line scan area with the height range of 400nm.

Substrate holder temperature set to 150°C during the deposition of α -sexithiophene leads to formation of yet another structures. Epifluorescence images show lack of geometrical polygons, but highly irregular structures emerge. Yet again, there are clearly two types of structures which significantly differ in the intensity of fluorescent light, but both exhibit Malus variations when polarization analyzer is rotated. The dimmer structures which occupy majority of the surface are rather compact, but have very ragged or fringed shapes, while the bright ones are elongated fiber like structures but, contrary to fibers obtained at lower temperatures which were mostly straight, those are curled and curved. Such richness in obtained shapes can be explained by the increase of the molecules surface mobility, which could result in frequent and progressive

3.1. GROWTH OF α -SEXITHIOPHENE NANOSTRUCTURES

defect formation leading to curved shapes in case of lying molecules, and fringed shapes of formations consisting of molecules which stand.

AFM analysis reveals that curled structures have ca. 600nm height, while the fringed ones do not exceed 100nm. Scan of the area between the bright and dull structures show presence of clusters with diameter of 100-200nm and the height up to about 50nm.

30nm thin-films fabricated at 170°C

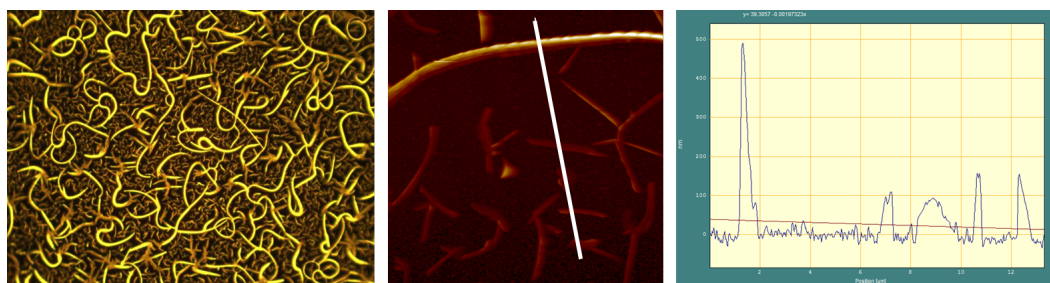


Figure 3.9: Epifluorescence ($130\mu\text{m} \times 97\mu\text{m}$) and AFM ($15\mu\text{m} \times 15\mu\text{m}$) micrographs of sample fabricated at 170°C. White line in AFM micrograph indicate the $14\mu\text{m}$ line scan area with the height range of 600nm.

When the substrate was heated up to 170°C during the deposition of α -sexithiophene the division for dimmer and brighter structures remained, but weakened. The bright structures form several hundreds of micrometers long curled and tangled fibers, while the dimmer ones fill the remaining space and form fiber like structures of diameters below $10\mu\text{m}$. No dendritic, or other irregular structures are observed, so it could be suspected, that the structures consist solely from lying molecules.

AFM scans reveal significant height difference in those two types of formations - fiber like structures are up to 200nm high, while the curled ones reach 800nm, which explains the difference in fluorescence intensity. Moreover, the dimmer structures resemble very much the structures obtained at 90°C, which were identified as consistent of lying molecules. Investigation of the area between the structures show similar clusters as in case of deposition at 150°C.

3.1. GROWTH OF α -SEXITHIOPHENE NANOSTRUCTURES

100nm α -6T on C₆₀ layers

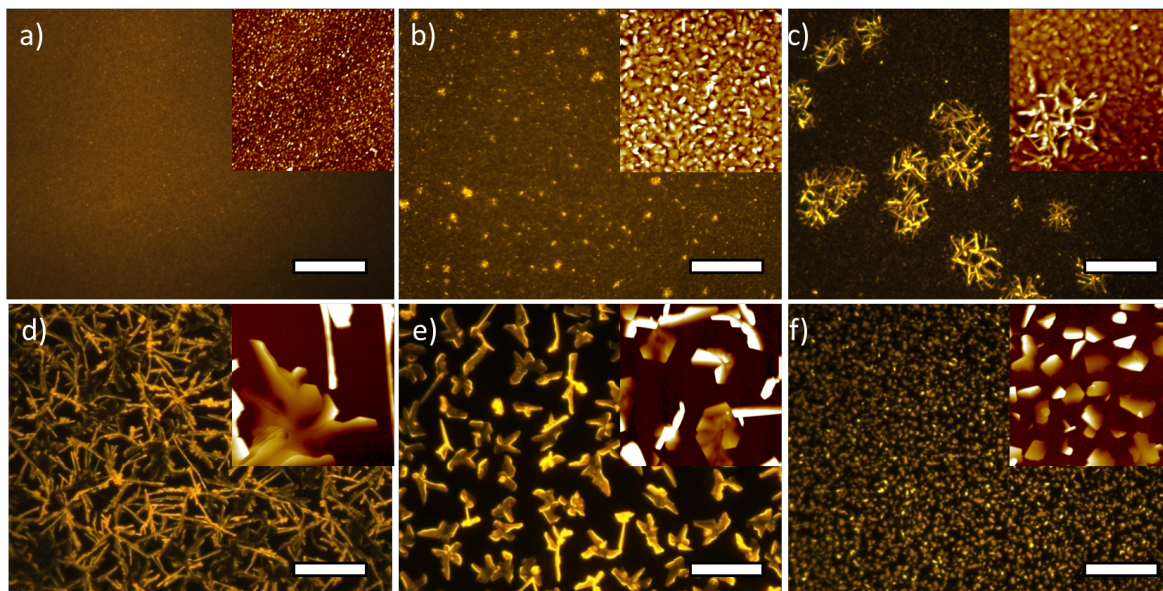


Figure 3.10: Epifluorescence micrographs of 100nm α -6T thin-films on Buckminsterfullerene fabricated at different substrate temperatures during deposition: room temperature, 70°, 90°C, 120°C 150°C, 170°C, a) to f), respectively. The insets present 5 μ m x 5 μ m AFM scans of the respective samples with height ranges of 30nm, 300nm, 300nm, 700nm, 700nm, 600nm, respectively. The scale bar is 20 μ m

100nm thin-films fabricated at room temperature

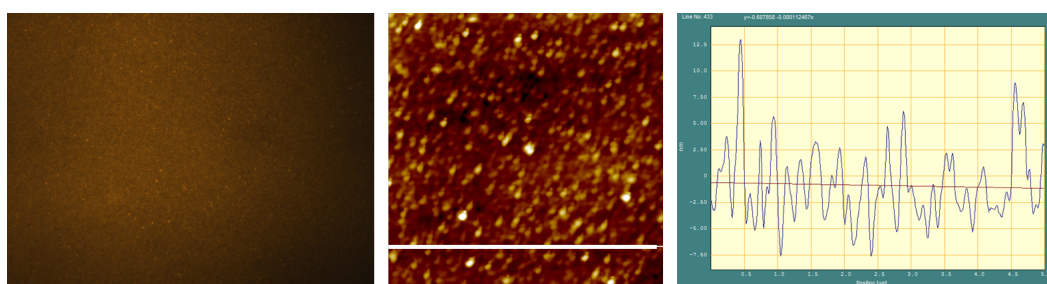


Figure 3.11: Epifluorescence (130 μ m x 97 μ m) and AFM (5 μ m x 5 μ m) micrographs of 100nm thin film of α -6T fabricated at room temperature. White line in AFM micrograph indicate the 5 μ m line scan area with the height range of 13nm.

3.1. GROWTH OF α -SEXITHIOPHENE NANOSTRUCTURES

When the substrate was kept at room temperature during deposition of α -sexithiophene, the resulting film is similar to the thinner film obtained at the same temperature in previous experiment. Similar intensity of fluorescent light appears, and faint flicker is present when polarization analyzer in the microscope is rotated. The roughness measurement performed with AFM system resulted in $S_q=4.1\text{nm}$.

100nm thin-films fabricated at 70°C

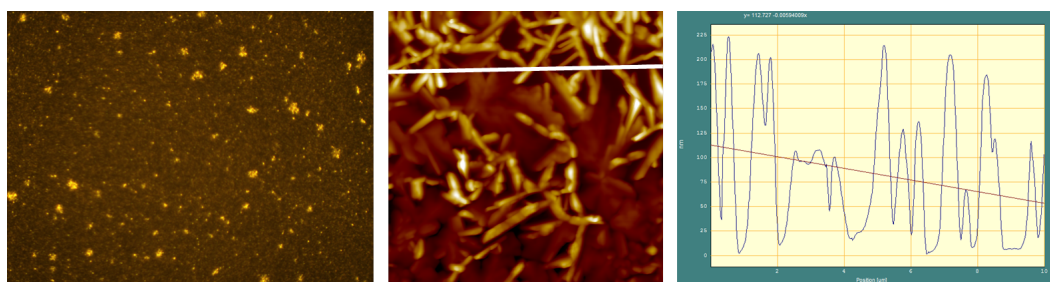


Figure 3.12: Epifluorescence ($130\mu\text{m} \times 97\mu\text{m}$) and AFM ($10\mu\text{m} \times 10\mu\text{m}$) micrographs of 100nm thin film of α -6T fabricated at 70°C. White line in AFM micrograph indicate the $105\mu\text{m}$ line scan area with the range of 230nm.

At 70°C of the substrate holder temperature during the deposition of α -sexithiophene, regions with larger fiber like structures start to emerge at various nucleation points. Their heights were about 200nm and lengths in order of few micrometers. The regions, which maximal size was in range of $5\mu\text{m}$, were uniformly dispersed and surrounded by a rough film similar to one obtained at room temperature.

3.1. GROWTH OF α -SEXITHIOPHENE NANOSTRUCTURES

100nm thin-films fabricated at 90°C

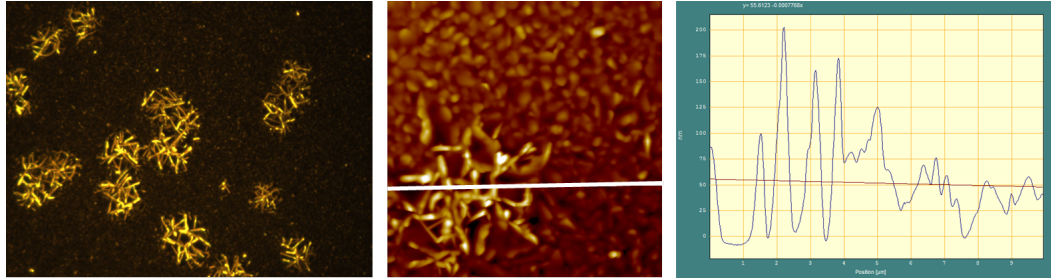


Figure 3.13: Epifluorescence ($130\mu\text{m} \times 97\mu\text{m}$) and AFM ($10\mu\text{m} \times 10\mu\text{m}$) micrographs of 100nm thin film of α -6T fabricated at 90°C. White line in AFM micrograph indicate the $10\mu\text{m}$ line scan area with the height range of 210nm.

Structures formed at 90°C of the substrate temperature during deposition of α -sexithiophene again formed very similar structures as the obtained at the same temperature during the experiment with thinner nominal layer of α -6T, but the the sizes of the biggest regions increased to over $50\mu\text{m}$ and the height of the fiber-like structures were reaching about 200nm.

100nm thin-films fabricated at 120°C

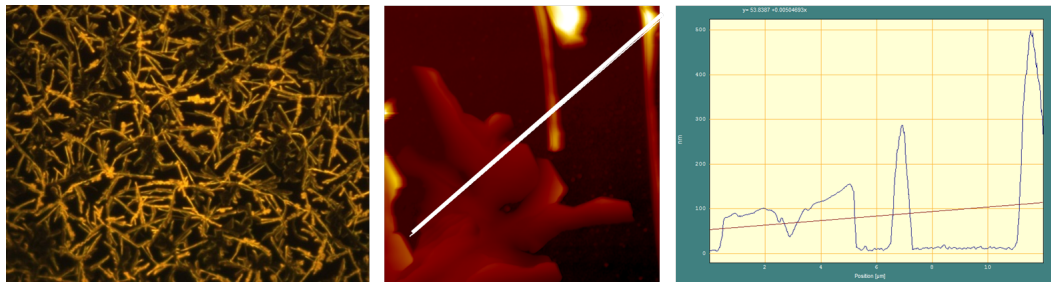


Figure 3.14: Epifluorescence ($130\mu\text{m} \times 97\mu\text{m}$) and AFM ($10\mu\text{m} \times 10\mu\text{m}$) micrographs of 100nm thin film of α -6T fabricated at 120°C. White line in AFM micrograph indicate the $12\mu\text{m}$ line scan area with the height range of 500nm.

On the samples with 120°C of the substrate holder temperature during the deposition of α -sexithiophene, the whole surface is uniformly covered with dense mesh of mixed fibers and dendritic structures, but also some polygon shape structures are identified.

The structures resemble very much the formations obtained during experiment with thin layer of α -6T at 110°C, but the obtained shapes are less regular. Epifluorescence image reveals bigger share of dendritic structures which seem spreading from the sides of the fiber like structures. Nevertheless it may occur due to aforementioned light injection effect, and only those dendritic formations which are structurally bound to the fibers emit bright enough fluorescence to distinguish them.

AFM scans show that the dendritic structures seem to be formed from polygonal formations with different and uncorrelated growth directions, which height is in order of 150nm, while the mean height of fibers was around 200nm, reaching 500nm in some areas. High resolution scan of the dendritic structure (see figure 3.15) has revealed clearly, that those structures contain monomolecular α -sexithiophene steps with terrace step height of approximately 2.2nm, which corresponds to standing α -6T molecules (2.24nm). Moreover, such steps could not be observed for needle like structures, what supports the statement that dendritic structures are composed of standing, while needle like - from lying molecules.

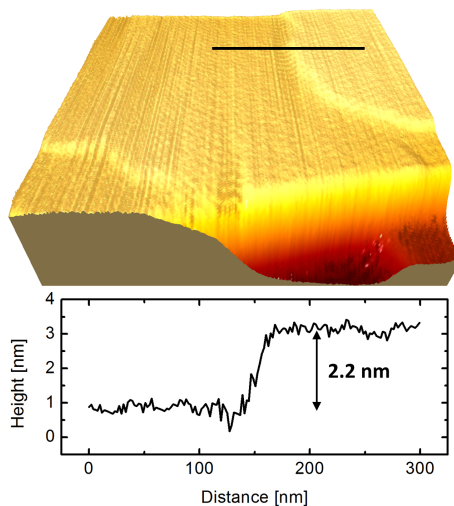


Figure 3.15: High resolution (500nm x 500nm) AFM scan of the dendritic α -6T structure formed at a surface temperature of 120° during growth. The black line indicates the position of the below height scan, revealing a 2.2 nm step height, fitting to the monomolecular height of (100) standing α -6T LT unit cell.

3.1. GROWTH OF α -SEXITHIOPHENE NANOSTRUCTURES

100nm thin-films fabricated at 150°C

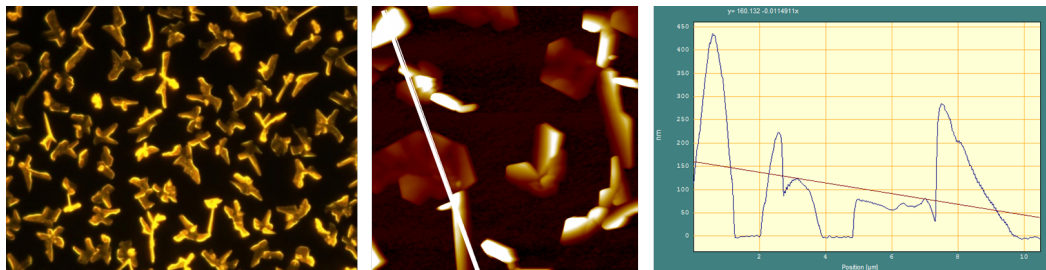


Figure 3.16: Epifluorescence ($130\mu\text{m} \times 97\mu\text{m}$) and AFM ($10\mu\text{m} \times 10\mu\text{m}$) micrographs of 100nm thin film of α -6T fabricated at 150°C. White line in AFM micrograph indicate the $10\mu\text{m}$ line scan area with the height range of 450nm.

Substrate temperature set to 150°C during the deposition of α -sexithiophene leads to formation of polygonal structures, which substantially resemble the lamellar formations obtained during low thickness deposition at 120°C. Obtained formations are of similar horizontal dimensions and are dispersed in similar manner as the ones obtained from previous experiment, but the needle like structures occur significantly less frequent. Nevertheless, still the formations adjacent to needle like structures exhibit stronger fluorescence. Rotating polarization analyzer reveals that intensity of fluorescent light varies accordingly in the whole structure indicating that lamellas are single crystalline structures. The AFM scans show, that the heights of lamellas and fiber like structures vary a lot from 50nm to over 400nm.

100nm thin-films fabricated at 170°C

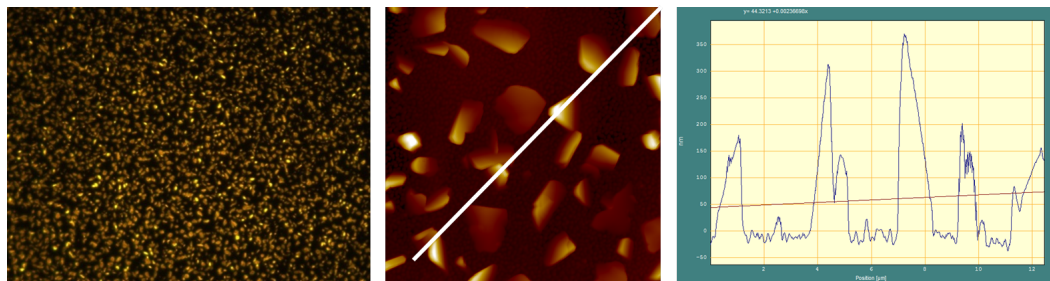


Figure 3.17: Epifluorescence ($130\mu\text{m} \times 97\mu\text{m}$) and AFM ($10\mu\text{m} \times 10\mu\text{m}$) micrographs of 100nm thin film of α -6T fabricated at 170°C. White line in AFM micrograph indicate the $12\mu\text{m}$ line scan area with the height range of 400nm.

When the substrate was heated up to 170°C during the deposition of α -sexithiophene new formation appears of rather small ($1\text{-}3\mu\text{m}$) crystallites of uniform fluorescence intensity. AFM scans reveal yet another time polygonal shape structures, which are tilted with constant slope throughout one crystalline site. Abrupt terminations of the facets which are recognized by AFM as nearly 90° steps can again indicate that the obtained structures are lamellar planes. The height of the crystallites is found in 100nm-400nm 200nm range.

Conclusion

Even though there are few differences in the evolution of structures constituting the thin (30nm) and thick (100nm) α -sexithiophene layers, until moderate temperatures (100°C-110°C) the same roadmap is followed in both cases.

In both series of experiments clear evolution of structures can be identified. Starting from low temperatures, regardless of nominal thickness of deposited material, obtained films are uniform, as the molecules are not mobile enough to form larger structures and the location of individual molecules is mostly determined by the locus of adsorption. With the increase in the substrate temperature, increase in diffusion occurs, and small structures start to appear in individual locations. Those can be the locations of debris or defects on the surface, or random.

If the temperature is further increased to 90°C, the number of the nucleation points rise, and also the star like branching starts from the nucleation points. Due to round en-

3.1. GROWTH OF α -SEXITHIOPHENE NANOSTRUCTURES

velopes of those formations and branching roughly from the center, it can be concluded, that the structures grow from the nucleation point outwards. From the difference in the fluorescence intensity, and the amplitude of fluctuations while the polarization analyzer is rotated it can be deduced, that the fiber like structures consist of lying molecules, contrary to the surroundings which are formed from standing ones. However, more detailed polarimetry analysis is described in section 3.1.4.

At higher substrate temperatures during deposition, the results of thin and thick film start to differ, but still some similarities can be observed. 110°C for the thin films results in very similar structures as 120°C for the thick ones. Resultant film can be described as further evolution of star like structures which grew far away from the nucleation points, finally merging together in dense mesh of long needle or fiber like structures, with high number of dendritic formations adjacent to them. The growth of larger nanofibers at increasing substrate temperatures on mica surfaces has previously been reported[20, 104]. It has been also shown by Simbrunner et al., that such coexisting formations of needles and dendritic formations can occur due to the fact, that the 67° tilt angle of the lying molecules crystal formed in ($\bar{4}11$) orientation (found in needle like structures) is equal to the tilt angle formed by standing (100) molecules (found in dendritic structures). It infers, that the nucleation of the crystallites consisting of standing molecules is favored at the sidewalls of already existing needles[99] as so called ledge-directed epitaxy[138].

The next common structure for the thin and thick films appear at 120°C and 150°C of substrate temperature, respectively. Those are the polygon shaped lamellar structures, which indicate well defined crystal faces with various tilt angles with respect to the substrate. Unfortunately, due to the top-projection imaging techniques involved, the presence of the possible void volume under the plates was not proven as it was demonstrated by Simbrunner[51]. Implementation of lamellar plates in organic solar cells can be a very interesting study in the standard configuration of the solar cell, where the interface could be formed around them leading to very short average bulk-to-interface distance. Nevertheless it is beyond the scope of this work to investigate it.

Above those temperatures, both films start to behave differently. As the three fold thickness increase changes significantly the surface energy and the interplay between intermolecular and surface adhesive forces result in formation of different struc-

tures. Above 120°C of the substrate temperature during the deposition of 30nm of α -sexithiophene, curly fibers consisting of lying molecules start to be formed. The space between them is loosely filled with fringed structures of standing molecules. Further increase in temperature results in formation of curly fibers with length in range of 100 μ m, between which straight short needles occur. Contrary, in case the 100nm thick film is deposited with substrate temperature of 170°, previously seen lamellas seem to decompose into smaller clusters of uniform sizes and thickness. The structures are sparser and film clearly appear discontinuous. This is likely due to the lower sticking probability of the incoming α -sexithiophene molecules at high surface temperatures.

Summary

Four temperature ranges have been recognized, where the obtained structures exhibit different morphological properties. At lower substrate temperatures, deposition of α 6T on C₆₀ results in rough continuous film and nanoscale clusters of highly polycrystalline nature. Increasing the temperature of the substrate during the deposition increases the molecular kinetics resulting in formation of regions consisting of fiber like structures. Reaching 120°C leads to saturation of the surface with the regions resulting in the dense mixed mesh of needle and dendritic like structures. Further increase of temperature induces a rapid transition to sparse, relatively large and compact flakes exhibiting distinct crystal faces and probably the lamellar structure. Increasing the temperature over 150°C overcomes the next critical point where high molecular kinetics and surface energy result in various structures depending on the thickness of the deposited material. Curly fibers are seen at low film thicknesses and individual clusters at high.

The presence of structures consisting of lying molecules could be expected in 70°C-150°C range where needle like structures are present.

3.1.4 Crystallography studies

In order to gain an insight into the crystalline structure of the films, they were investigated with fluorescence polarimetry and X-ray diffractometry. The first technique allowed to determine the angular orientation of the transition dipoles of α -sexithiophene molecules with respect to the long needle axis, therefore it was applied only to the sample where distinct needles were identified by epifluorescence imaging, namely the

3.1. GROWTH OF α -SEXITHIOPHENE NANOSTRUCTURES

sample with 100nm of α -6T deposited where the temperature of the sample holder was 110°C.

Fluorescence polarimetry.

The result of fluorescence polarimetry performed on a 100nm thin-film of α -6T fabricated at 120° is presented in the figure 3.18. The colors indicate local angles between long molecular axis and long needle axis - β_{mol} . A histogram of the image from figure 3.18, together with fitted Gaussians is presented in figure 3.19. This is the final data derived from the measurements which shows the distribution of different molecular packings in fibers.

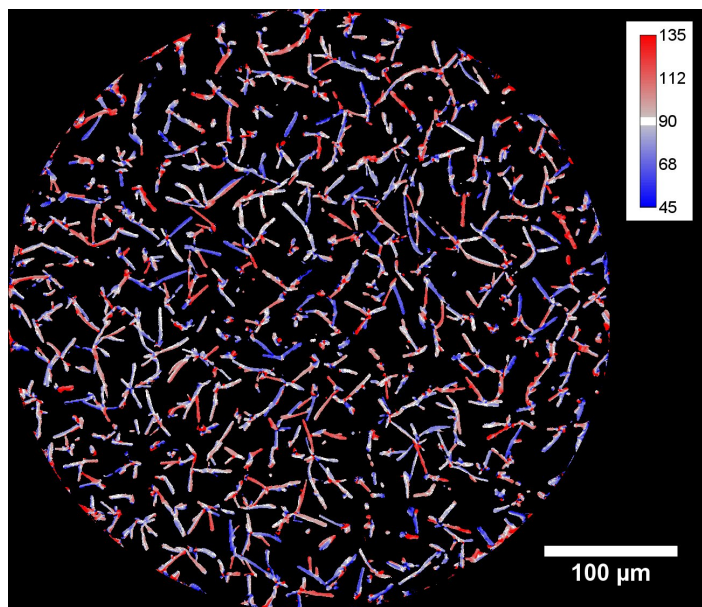


Figure 3.18: The epifluorescence polarimetry image presenting local angles between long molecular axis and long needle axis - β_{mol} .

The mean values of β_{mol} angle distributions identified in this experiment are equal to 74°, 90°, and 107°, the latter being a symmetric reflection of the first one over the long needle axis. The found values match with previously reported β_{mol} angles for herringbone packed lying molecules with $(\pm h, 0, 1)$ and $(\pm h, \pm 1, \pm 1)$ being contact faces [20, 101], which predominantly occur in needle like structures. The measurements and data processing was done by Frank Balzer.

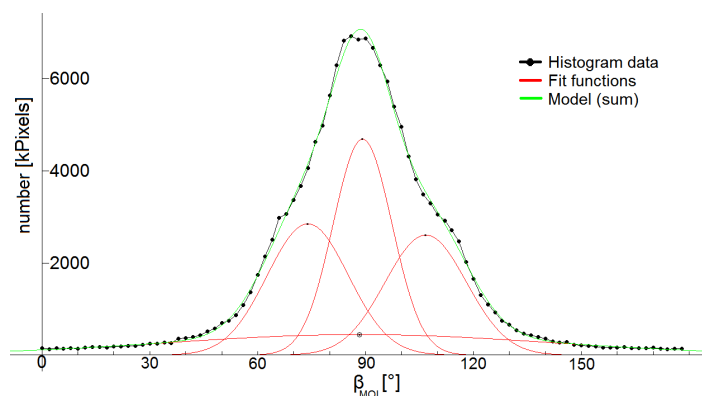


Figure 3.19: The histogram of the image presented in figure on the facing page with fitted Gaussian distributions.

X-ray diffractometry

θ -2 θ scans Diffraction patterns of measured samples, are presented in figure3.20.

The most visible aspect are the regular peaks indicating the presence of only one crystalline phase and its higher order harmonics. Their coincidence with the simulated locations of α -sexithiophene (200) (standing molecules) and higher orders peaks (marked by dotted lines), together with the match of relative peak heights (Cambridge Crystallographic Data Centre), legitimates to confirm the presence of (200) crystalline structures, i.e. consisting of standing molecules, in most of the prepared samples. Only the sample fabricated at 30°C does not show the presence of α -6T characteristic pattern, while the other samples exhibit increasing of the signal together with increase in substrate temperature. This is an indicator of the increasing amount of (200) oriented crystals up to temperature of 170°C, where clear drop occurs. However, it could be explained by before mentioned desorption of material from the sample at high substrate temperatures. There is lack of any other pattern matching with another crystalline orientation of the α -sexithiophene[139] nor the buckminsterfullerene[140], but all of the samples exhibit similarly sized peak at 2.7\AA^{-1} which corresponds to aluminum (111), on which C_{60} and α -6T layers were deposited.

The rocking curves taken at the most intense (1200) peak showed a significant narrowing of the FWHM for films grown at temperatures higher than 90°C. This indicates that the mosaicity, i.e. mutual misalignment of crystalline sites with respect to the

3.1. GROWTH OF α -SEXITHIOPHENE NANOSTRUCTURES

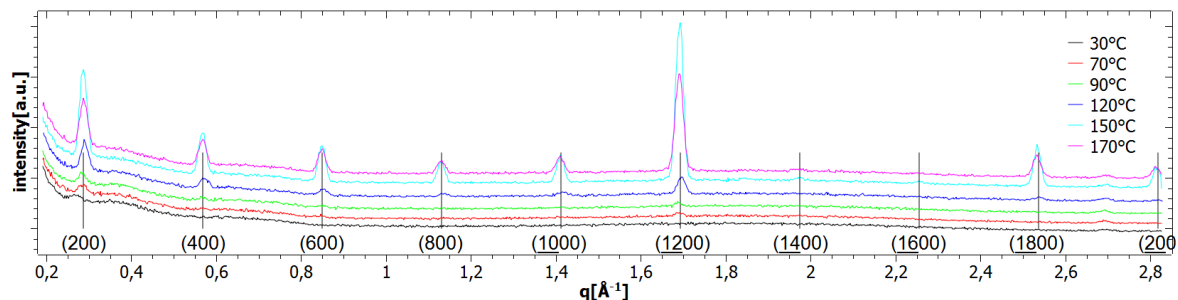


Figure 3.20: X-ray diffraction patterns vs. scattering vector obtained from α -6T samples prepared at different substrate temperatures during deposition exhibiting the presence of α -6T (h00) orientations (vertical lines indicate positions of simulated α -6T h00 peaks), with dominant 1200 peak.

substrate, falls for samples prepared at elevated temperatures, reaching its minimum for substrate deposition temperature equal 170°C.

Summary

Only the presence of standing molecules (200) has been proven by X-ray diffractometry methods. The observation that the XRD investigations did not reveal these orientations can be explained by the fact that the nanofibers represent only a minimal volumetric fraction of the total material that gives rise to X-ray scattering, while dendritic structures and clusters are vast spread. Films obtained at lower temperatures of the substrate during α -sexithiophene deposition exhibit high polycrystallinity, as well as high mosaicity. Increase in temperature induces the growth of bigger and better oriented crystals.

3.2 Implementation of α -sexithiophene nanostructures in solar cells

3.2.1 α -sexithiophene nanostructure integration with spin-coating

As the previous study in this work has shown, the structures grown from α -sexithiophene on thin film of C_{60} can reach unity aspect ratio, therefore the fibers could potentially be mechanically torn away during spin coating of the transparent electrode and encapsulant, which are the next steps in fabrication of solar cell. To investigate this, epifluorescence images of the same region of the substrate were taken before and after spin coating steps. The images are presented in figure 3.21. Green coloring of the fin-

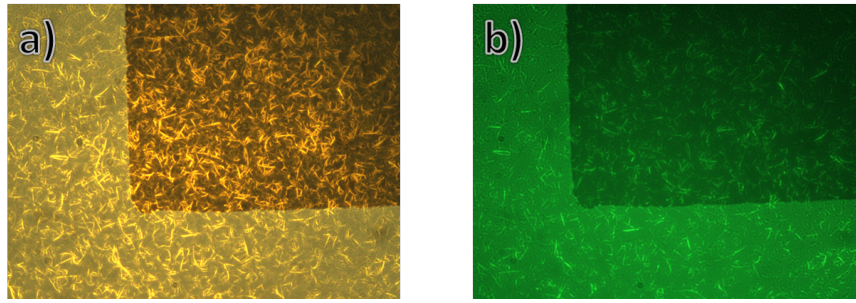


Figure 3.21: Epifluorescence micrographs of the same region of a solar cell device before a), and after b) spin coating processing. The image a) is taken with UV II filters set, while the image b) with FITC.

ished solar cell image presented in figure 3.21 b) comes from the fact, that it was taken with usage of FITC (ex:460nm-495nm, det:515nm-555nm) filtering system in contrast to UV II(ex:330nm-380nm, det:LP420nm), which was used to take the initial one (3.21 a). The change was required, as the encapsulant layer strongly fluoresces in blue color when excited by UV, which prevented clear observation of the structures underneath.

The presence of the encapsulant layer distorted the image presented in figure 3.21 b), but it is seen, that the fibers seem to remain their position and orientation. In order to visualize similarity of the structures before and after spin-coating, selected areas of both images were assigned to red and green channels of a new image presented in figure 3.22. As a result, the yellow color indicates structures identified in both images, the red

3.2. IMPLEMENTATION OF NANOSTRUCTURES

color indicates the ones identified only in figure 3.21 a) and green only the ones from figure 3.21 b). The majority of green features in top right corner, together with the red majority in bottom left may indicate differences in illumination of two samples rather than misalignment of fibers. As can be seen, the yellow features dominate the image, therefore it was concluded, that spin coating processing does not affect the positions of underlying tall structures significantly.

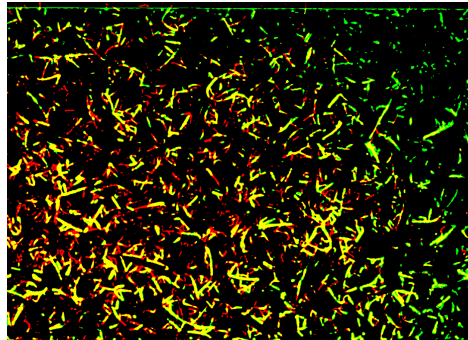


Figure 3.22: Color channel combination of selected area of images 3.21 a) (red), and 3.21 b) green.

Even though a mechanical damage during spin coating does not occur excessively, another problem has appeared during the annealing of the transparent electrode layer. In order to evaporate the solvent from the PEDOT:PSS blend it is to be baked on a hot plate at recommended temperature of about 150°C[123, 120, 141]. Unfortunately this led to peeling off and rolling of the active layers from the substrate. The image of the rolls on the substrate is presented in figure 3.23. As such defects can appear due to the mechanical strain caused by rapid solvent release and mismatching thermal expansion, the annealing procedure of PEDOT:PSS has been changed. In all proceeding experiments, the transparent electrode layer was annealed by heating up from ambient temperature to 90°C for 5 min, and then kept at 90°C for 25 min. This annealing procedure prevented the layers from rolling.

Summary

Spin coating processing was found not harmful for the underlying structures, but the annealing step parameters were altered with respect to the values found in the literature, in order to prevent the peeling off of the active layers.

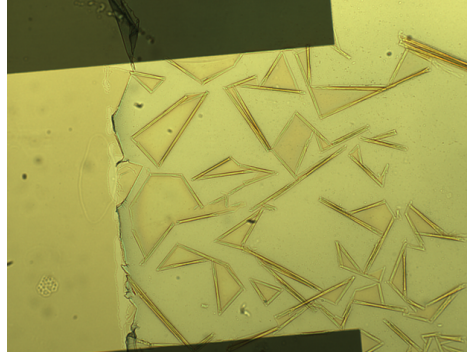


Figure 3.23: 2.6mm x 1.9mm bright field micrograph presenting the peeling off of the α -6T layer after annealing at 150°C.

3.2.2 Optimization of bilayer device

Even though the bilayer α -sexithiophene devices has been already studied in literature[111, 113, 115], lack of reports about the inverted configuration of in-house fabricated solar cells demands the optimization of layer thicknesses to be a first step in systematic study of such structures. However, the thicknesses reported in those publications can serve as a good initial guess for starting point of the optimization procedure. The optimization was conducted with the device fabricated at room temperature of the substrate during the deposition of electron donor layer.

C_{60} layer

At first, the C_{60} layer was investigated. The examined thicknesses were 15nm, 20nm, 30nm, 40nm, and 50nm, while the thickness of α -6T was kept constant at 20nm. The derived parameters, which were obtained from photo-electrical characterization of the devices fabricated at various temperatures are presented in figure 3.24. Top left graph in figure 3.24 presents the open circuit voltage of fabricated devices versus the thickness of C_{60} layer. It can be noted, that most of the values are close to 390mV which is expected value for this system[142], while the open circuit voltage of the device with thinnest C_{60} layer is definitely lower than others.

All the other parameters (see figure 3.24 top right, and bottom row) i.e. short circuit current density, fill factor, and power conversion efficiency follow similarly shaped

3.2. IMPLEMENTATION OF NANOSTRUCTURES

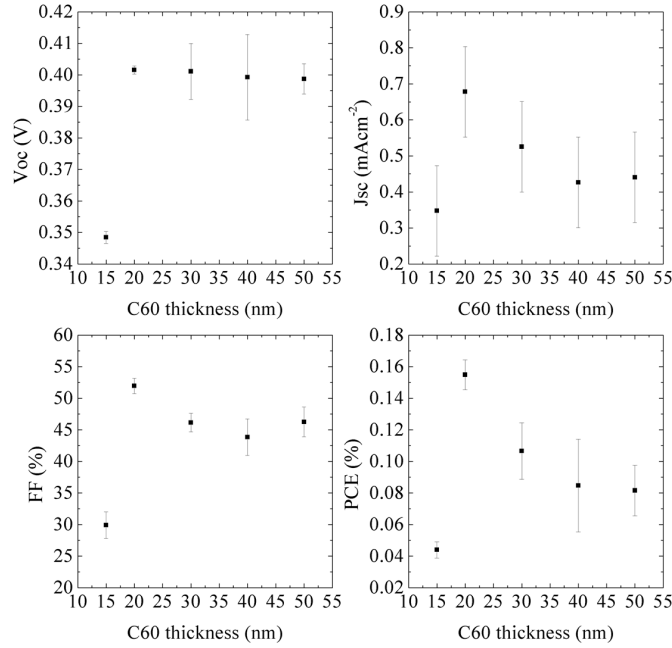


Figure 3.24: Solar cell performance parameters for varying thickness of C_{60} .

curves, with outstanding low values at 15nm C_{60} thickness, peaking the maximum at 20nm and decaying with increase in thickness.

Such a behavior is expected, since the C_{60} layer serves just as electron transport layer and the photons absorbed in C_{60} do not take part in photogeneration of current. Therefore, with increase in thickness, the series resistance, which increase results in smaller fill factor, and bigger chance of recombination affects the short circuit current density. Nevertheless, below 20 nm, the C_{60} film is can be discontinuous (as peak-peak height values of C_{60} layer is in order of 15 nm - see 3.1), hence pinhole short circuits will degrade the solar cell performance.

α -sexithiophene layer

Setting the C_{60} layer thickness to 20 nm, number of devices with the thickness of α -sexithiophene layer equal to 20nm, 30nm, 40nm, 50nm, 60m, and 70nm were fabricated at room temperature. The derived solar cell characteristics of those devices are presented in figure 3.25. Open circuit voltages presented in top left graph in figure 3.25 are rather uniform over whole domain. The fill factor and power conversion effi-

ciency exhibit initial increase until about 40nm of layer thickness, followed by decrease above 60nm with a plateau between those values, while the short circuit current density reaches its maximal value for 30nm followed by slow decay.

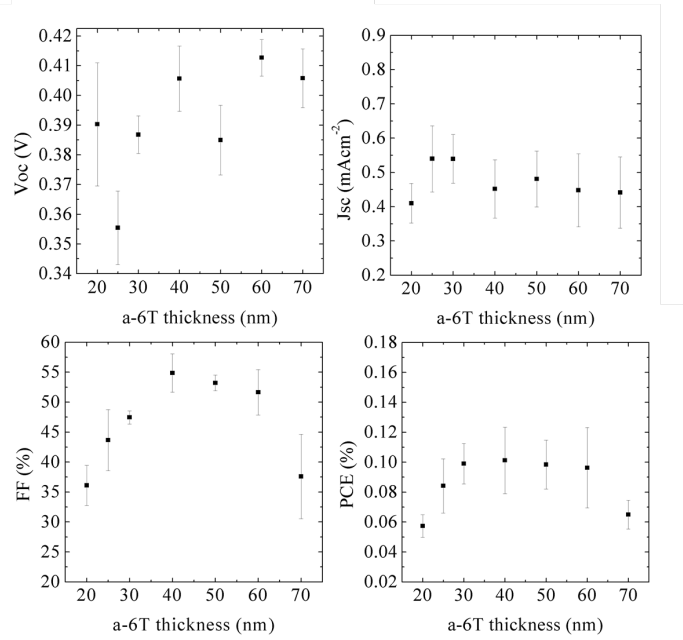


Figure 3.25: Solar cell performance parameters for varying thickness of α -6T.

For low thicknesses, increase of the active volume, from which the excitons could reach the interface, is responsible for raise in the solar cell performance - especially the short circuit current, while for thicknesses way thicker than exciton diffusion length, further increase resulted in higher equivalent series resistance for separated charges traversing the material.

Summary

From above mentioned experiments, the conclusion was drawn, that optimal active layers for the device should be 20nm for the buckminsterfullerene and 30nm for α -sexithiophene. All the further devices were fabricated according to this assumption. The two series of experiments were conducted in two weeks time interval, therefore the discrepancy between the values was seen. Different batches of α -6T material used, as well as changes in glove box atmosphere and in characterization setup can be an

3.2. IMPLEMENTATION OF NANOSTRUCTURES

explanation here. Nevertheless, the repeated experiments within the same series have result in coherent values.

3.2.3 TiO_x photo conductivity

Using TiO_x layer in solar cell devices is known to introduce the effect of so called “S-shaped J-V curve”[143, 125]. Example of such characteristics is shown in figure 3.26 (blue and red curve). The investigation conducted by Ecker et al. have revealed that such effect caused by titanium oxide exhibiting p-type semiconductivity can be overcome by light soaking of the device which results in resistivity drop of TiO_x layer. The S-shape recovery is presented in 3.26.

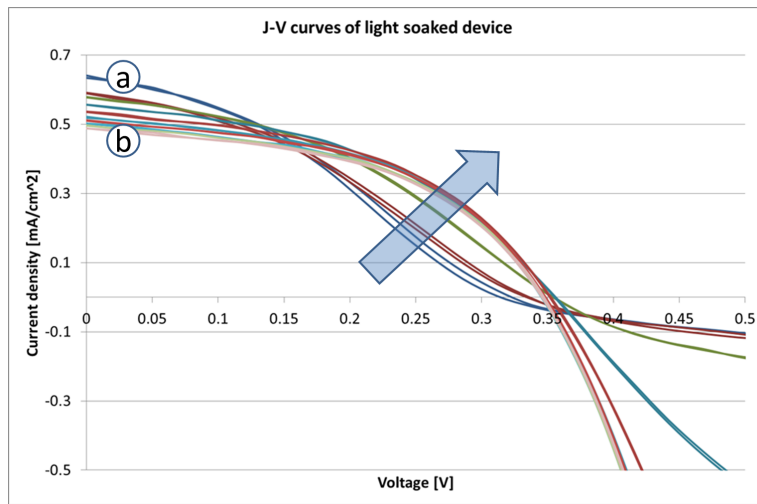


Figure 3.26: J-V curves of light soaked device taken at 2 min intervals showing the change of the characteristics from S-shaped low fill factor curve of initial measurement (curve a), to the desired high fill factor curve after 14 min (curve b)

In order to investigate how long the devices need to be illuminated before the effect vanishes, number of devices were illuminated with 1.5AM 1sun source, and the J-V measurements were taken each 30s. Nevertheless, due to the encapsulant, prolonged illumination of the devices resulted in progressive deterioration of devices. Therefore the power conversion efficiency of the device was chosen as figure of merit to determine the optimal light soaking time, after which the valid measurement of the solar cell performance will be taken.

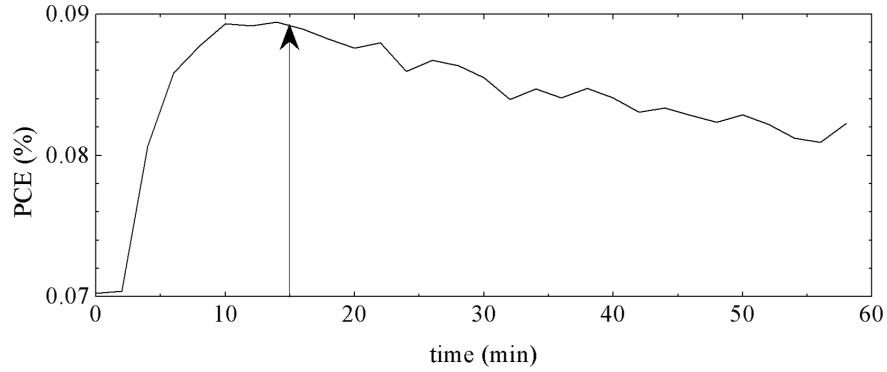


Figure 3.27: Power conversion efficiency versus time during light soaking of the exemplary device under 1.5AM 1Sun illumination. The arrow indicates the maximum efficiency point.

Number of experiments have been performed, where the power conversion efficiency was measured during the light soaking period, exemplary of which is presented in figure 3.27. The result of 10 experiments was that the time needed in order to obtain maximum efficiency was equal to 15 ± 1.5 min.

Summary

All the devices were light soaked with 1.5AM 1Sun illumination for 15 minutes, before the valid measurement was taken.

3.2.4 Impact of the substrate temperature during α -6T deposition on performance of solar cell

The culmination work of this thesis, are the results of the experiment where the performance parameters of solar cells, which donor layer was fabricated at different substrate holder temperatures during deposition, are compared. The substrate temperatures during α -sexithiophene deposition at which the devices were fabricated were 30°C, 50°C, 60°C, 70°C, 80°C, 90°C, 100°C, and 120°C.

Open circuit voltages of fabricated devices is presented in left hand side of figure 3.28. The measured values are consistently located in close vicinity of 350 mV, which agrees

3.2. IMPLEMENTATION OF NANOSTRUCTURES

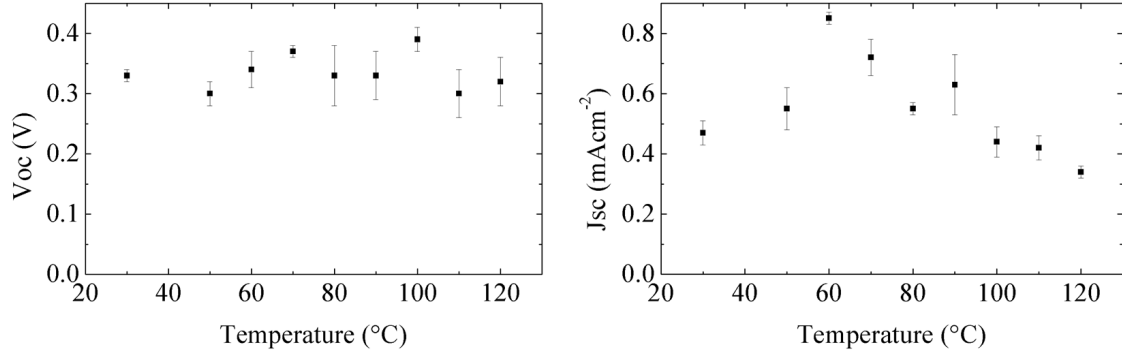


Figure 3.28: Open circuit voltage versus the temperature of the substrate during donor layer deposition.

with reported V_{OC} dependencies, which rely on the energetic characteristics of used materials rather than material geometrical properties like thickness or arrangement[142].

Short circuit current density dependence on the substrate temperature is presented in right hand side of figure 3.28. It clearly exhibits the maximum at about 60°C, when larger regions consisting fiber like structures start to appear in devices. The drop at higher temperatures can be explained by occurrence of material depletion zones around the fiber like structures, which can lead to low equivalent shunt resistance or internal short circuits.

The fill factor of fabricated solar cells is presented in left hand side of figure 3.29. It

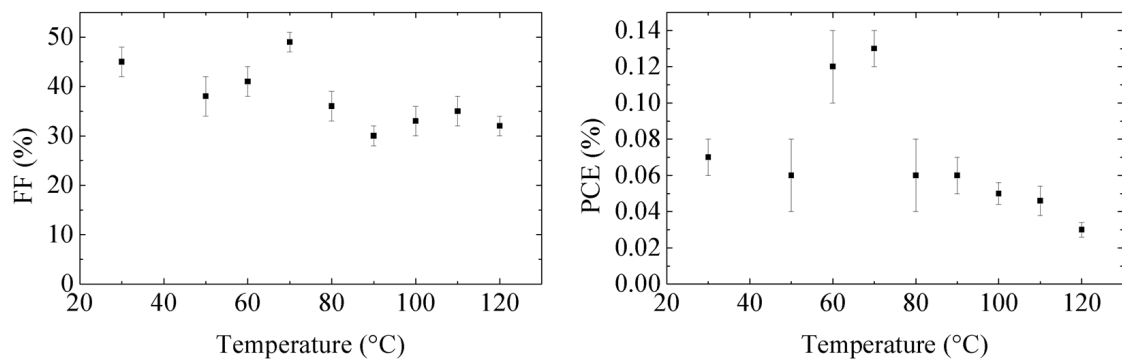


Figure 3.29: Fill factor versus the temperature of the substrate during donor layer deposition.

is in general decreasing in value together with increasing temperatures, with distinct peak occurring at 70°C. At this temperature the crystalline structures saturate the surface, which can improve the series resistance of solar cell. As previously explained in section 1.5, fill factor is strongly bound to the parasitic resistances in solar cell. Further decrease in fill factor value with the temperature can be explained similarly to short circuit current density, by appearance of depletion zones, which significantly reduce equivalent shunt resistance of solar cell, as well as to reduction of junction area.

The power conversion efficiency dependence on the temperature of substrate during deposition of electron donor layer is presented in right hand side of figure 3.29. It exhibits strong peak between the values of 60°C and 70°C, where it rises in value more than 100% compared to room temperature. Beyond this domain, the power conversion efficiency drops with increasing temperature.

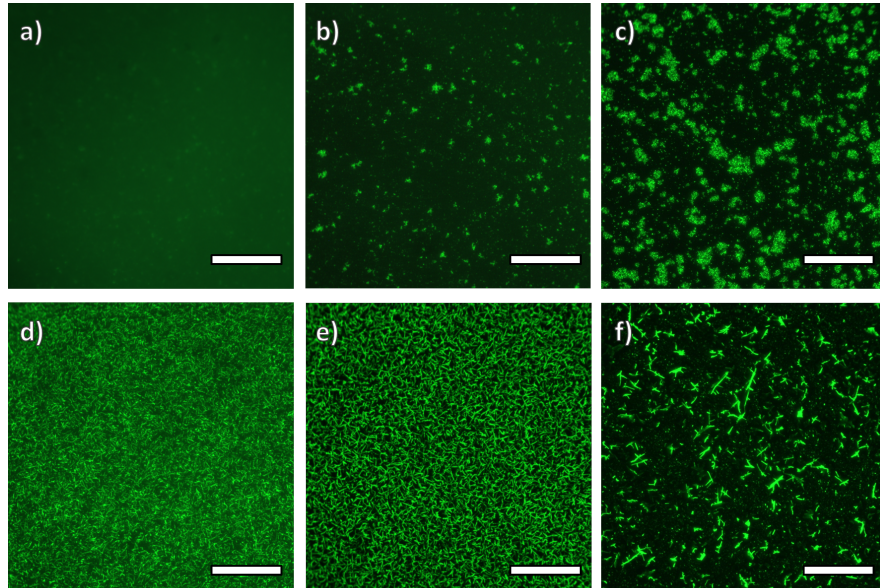


Figure 3.30: Epifluorescence micrographs of the measured solar cell devices fabricated at different substrate temperatures during deposition: room temperature, 50°, 60°C, 70°C 90°C, 120°C, a) to f), respectively. FITC filter bank was used in order to remove excessive blue fluorescence from UV exposed encapsulant. The scale bar is 20 μ m.

The epifluorescence images of few of the measured devices are presented in figure 3.30. At room temperature, a rough continuous film is observed, while at 50°C, small

3.2. IMPLEMENTATION OF NANOSTRUCTURES

($<3\mu\text{m}$) clusters are formed at individual nucleation points (figure 3.30 a and b). At 60°C , we observe a mesh of fiber like structures formed in randomly distributed domains of various size, while at 70°C such structures fully cover the surface area (figure 3.30 c and d). At an increased substrate temperature of 90°C , the formation of fiber like structures persists, but contrary to the sample prepared at 70°C , the structures are clearly separated by the areas where virtually no fluorescence is observed (figure 3.30 e). At 120°C , $10\text{-}20\mu\text{m}$ long, straight, and branching fibers are formed, which are surrounded by a mesh of shorter ones – $2\text{-}5\mu\text{m}$ (figure 3.30 f). It is important to note, that the observed morphology variations occur here at lower temperatures than those stated in section 3.1.3. It is ascribed to a different substrate holder employed for these devices compared to the morphology studies, and thus the reported substrate holder temperatures are not the absolute surface temperatures. Potential effect of annealing during PEDOT:PSS solvent evaporation should be also taken into consideration, but it was not studied further in this work.

Summary

Over 100% power conversion efficiency increase has been identified for the devices, which electron donor layer was deposited at substrate temperature between 60°C and 70°C , which coincides with temperature, where the first monocrystalline sites start to appear in deposited films. This range is characterized by a maximum density of fiber like structures. At higher temperatures, the lower density of larger fibers leads to a reduced junction area and thus device performance. The fluorescence polarimetry measurements performed on corresponding structures have strongly indicated the presence of lying molecules, which enhance the vertical charge transport favored in solar cell applications. Moreover, the formations constituent of standing molecules revealed by XRD measurements could also enhance the performance of the devices in this configuration, as they facilitate efficient horizontal charge transport from the $\alpha\text{-6T}$ nanostructures to the transparent electrode.

4 Conclusions

The major topic of the present thesis is the investigation of the α -sexithiophene crystalline formations on C_{60} thin films, their internal structure, and the influence of those structures on organic solar cell performance. The preliminary driver for this research was the strong carrier mobility anisotropy observed in α -6T molecules, which could lead to an improvement in the electronic and optical properties of crystalline structures in contrast to amorphous thin-films. In crystalline α -6T, the direction of high carrier mobility is defined the $\pi - \pi$ stacking, which, for solar cell applications, favors molecules lying on the substrate due to charge transport perpendicular to the surface. Furthermore, laying molecules infer the optimal orientation of the transition dipole for the maximal light absorption.

Having a big collection of knowledge, know-how, and expertise in the field of crystalline nanostructures growth from conjugated oligomers at NanoSYD, the challenge of this project was undertaken.

4.1 Hardware

A dedicated, one chamber, 3-source, high vacuum system has been designed and built in order to perform the organic molecular beam depositions. A SCADA system was developed in LabVIEW environment in order to monitor and control process parameters and store them for later inspection.

A photovoltaic characterization station has been established. It involved the establishment of in-house standard for organic solar cell substrates, fixtures, and connections to the measurement equipment. In order to assert equal illumination conditions for the measured devices, a translational stage was integrated into system, which positions the device under test with respect to the illumination beam. The software controlling

the characterization station was developed in a way to also allow for the measurements of transistors and other thin-film photosensitive devices.

4.2 Growth of α -sexithiophene structures on C_{60}

Four temperature domains have been identified, where various crystalline structures have been obtained from α -sexithiophene thin-films of 30nm and 100nm thicknesses over thin-films of buckminsterfullerene.

The resulting structures varied a lot in morphology and internal structure. At substrate temperatures during the α -6T deposition lower than 50°C, a rough film of strongly polycrystalline nature was obtained. At higher temperatures, regions with a dense mesh of coexisting needle like, and dendritic structures were formed. At 70°C the regions were separated and did not exceed 20 μm , while at 120°C the sample surface was saturated with the mesh. A further temperature increase lead to an abrupt change of the structure type, which formed sparse, tall, crystallite sites of potentially lamellar nature. After crossing the next critical temperature of 150°C, long, curly fibers were obtained for thin films, while thick depositions result in formation of dense uniform crystalline sites of low mosaicity.

The XRD studies have shown the increasing amount of (200) oriented crystalline sites and decrease in mosaicity with increasing the substrate temperature during the α -6T deposition, while the Epifluorescence polarimetry investigations strongly indicate that the observed needle like structures consist of lying molecules.

4.3 Crystal enhanced organic solar cells

A significant influence from the crystalline structures in the donor material on the performance of the α -sexithiophene – C_{60} bilayer solar cell has been observed. An increase over 100% in the power conversion efficiency has been reported at substrate temperature ranging between 60°C and 70°C. It is addressed to the formation of a crystalline nanofibers within the α -sexithiophene thin film. As the fibers has been identified as constituent of lying molecules, an increase in the light absorption as well

as improved charge transport properties are expected. Moreover, the crystalline α -6T layer can lead to more efficient exciton diffusion.

At higher temperatures, the power conversion efficiency drops rapidly. This phenomenon is explained to be a result of thinning of the α -6T film between the crystalline fibers. Increased molecular kinetics on the surface leads to more efficient transfer of the material from the inter-fiber film to the fibers, which forms a depletion zone around them. As the equivalent shunt resistance is significantly lowered in the zone, leakage path for photogenerated current is created. Additionally, a reduced junction area also suppress the performance of solar cell.

5 Outlook

This comprehensive study has addressed mainly one aspect of one particular configuration of α -sexithiophene – C₆₀ bilayer solar cell. In order to improve further the understanding of this system, several improvements should be introduced.

5.1 Improvements

5.1.1 Optimization of device at elevated temperature

Even though, the optimization procedure has been performed, it considered only the device fabricated at the room temperature. As the devices of maximal power conversion efficiency has been found to be fabricated at elevated temperature of the substrate during the deposition of electron donor layer, it is strongly recommended to repeat the optimization procedure for the optimal temperature.

5.1.2 OMBD system

The OMBD system used for experiments presented in present work was designed with special care, but the in-house design of Knudsen cell could still be improved. One of the major difficulties was the maintenance of constant deposition rate and avoidance of flash depositions. Material vessel, being heated by thermocoax wire, lacked sufficient heating of the cap, which is suspected to have significantly lower temperature than the vessel walls. This fact can easily lead to the condensation of the material at the cap and around the orifice, hence reducing its diameter and ultimately closing it completely. Decrease in deposition rate was compensated by increased heating, which - in case of closed orifice - led to sudden opening of it due to the pressure build up and the flash deposition of the material occurs. Another problem connected with the change

of orifice diameter is unknown change in the deposition profile - leading to potentially invalid tooling factor for the time the orifice is altered.

Proposed solutions would incorporate usage of alumina insulator, which could reduce the thermal gradients within the evaporator. Moreover inductive heating could be applied, where the coil surrounding the vessel will induce eddy currents in the vessel shell, which will cause its resistive heating.

5.1.3 Encapsulation

As the long term stability was not in the scope of the present work, there was lack of strong emphasis on the encapsulant choice for fabricated devices, and it was selected on purely pragmatic basis like short delivery of suitable amounts and fast curing time. Nevertheless, it has been found, that devices were still significantly degrading during prolonged measurements (even though less than without encapsulation). One of the solutions to improve the encapsulation is application of SiO_2 / PMMA bilayers[144]. Both however require significantly longer fabrication processes.

5.2 Further research

There is a number of experiments branching from the presented research, which could lead to new discoveries in organic solar cells.

5.2.1 Multistage deposition

The main identified reason for the performance drop with the presence of larger crystalline sites is the appearance of material depletion zones between the structures. However, those areas could be potentially filled with the same material, but deposited subsequently at lower temperature of the substrate, which will suppress the surface kinetics of the molecules. It can be foreseen, that such deposition pattern could overcome the drawbacks of the material depletion zones, while it will allow for studying the influence of larger crystals on the performance of solar cell.

5.2.2 lamellar growth of α -sexithiophene

As the presence of lamellar structures is suspected in the fabricated samples, it opens a possibility to study it in detail. Being able to grow the arrays of tilted plates could be very interesting for application in standard configuration solar cell, for example with the electron acceptor applied from the liquid phase like PCBM. The preliminary experiments of growing the structures directly on Au anode have been already made within this project, nevertheless due to excessive short circuits due to lack of electron blocking layer it was temporally suspended.

5.2.3 In-situ growth monitoring

considering the identification of deposited a variety of different structures which can be obtained from α -sexithiophene on thin film of C_{60} , it would be tempting to monitor the morphology *in-situ* during growth. Using the photo luminescence properties of, α -6T one could use a UV lamp, or scanning laser to excite the sample while the sample could be observed by a long working distance microscope objective for *in-situ* detection of the grown crystallites.

Publications

Reviewed publications

- **Growth of α -sexithiophene nanostructures on C60 thin film layers.** Radziwon, Michał Jędrzej; Madsen, Morten; Balzer, Frank; Resel, Roland; Rubahn, Horst-Günter. In: Nanotechnology (submitted, Article reference: NANO-100649) 2013
- **Crystallites of α -sexithiophene in bilayer small molecule organic solar cells double efficiency.** Radziwon, Michał Jędrzej; Madsen, Morten; Rubahn, Horst-Günter. In: Renewable energy and the environment / Optical Nanostructures and Advanced Materials for Photovoltaics (PV) / OSA Optics and Photonics Congress/ (submitted, Control ID: 1780211) 2013
- **Nanotag luminescent fingerprint anti-counterfeiting technology.** Radziwon, Michał Jędrzej; Rubahn, Horst-Günter; Johansen, Stefan ; Tavares, Luciana . In: Nanoscale Research Letters, Vol. 7, No. 1, 2012, p. 262.
- **A nanofibre tag.** Radziwon, Michał Jędrzej (Inventor); Rubahn, Horst-Günter (Inventor); Johansen, Stefan (Inventor). IPC No.: 11156560.2 - 2210. Mar 02, 2011.

Oral presentations

- **Inverted C60: α -6T small molecule organic solar cells: Correlation between morphology and device performance.** Radziwon, Michał Jędrzej; Madsen, Morten; Rubahn, Horst-Günter. 8.07.2013. ISFOE 2013, Thessaloniki, Greece.

- **Nanotechnology and Organic Solar Cells.** Radziwon, Michał Jędrzej. 30.07.2011. Lecture at PHYSiCsiw lang 'yan, Manila, The Philippines.
- **A Nanofibre Tag.** Radziwon, Michal Jędrzej; Johansen, Stefan ; Rubahn, Horst-Günter. 8.10.2011. Oral presentation at KNS - 9th. Students' Scientific Conference Man-civilization-future, Będlewo, Poland.

Conference abstracts

- **Inverted C60:α-6T small molecule organic solar cells: Correlation between morphology and device performance.** Radziwon, Michał Jędrzej; Madsen, Morten; Rubahn, Horst-Günter. 2013. ISFOE 2013, Thessaloniki, Greece.
- **Oil contamination photoacoustic sensor system.** Radziwon, Michał Jędrzej; Albu, Mihaela; Duggen, Lars; Willatzen, Morten; Zweg, Thomas; Rubahn, Horst-Günter. 2011. The 19 th. International Conference on Advanced Laser Technologies, Golden Sands, Bulgaria.
- **Detection of n-heptane by photoacoustic spectroscopy using a 1725 nm DFB laser diode.** Radziwon, Michał Jędrzej; Albu, Mihaela; Frese, Ralf; Lopes, Natasha; Rubahn, Horst-Günter. 2011. The 18th International Conference on Advanced Laser Technologies, Egmond aan Zee, Netherlands.
- **A Nanofibre Tag.** Radziwon, Michal Jędrzej; Johansen, Stefan ; Rubahn, Horst-Günter. 2011. KNS - 9th. Students' Scientific Conference Man-civilization-future, Będlewo, Poland.

Conference posters

- **Inverted C60:α-6T small molecule organic solar cells: Correlation between morphology and device performance.** Radziwon, Michał Jędrzej; Madsen, Morten; Rubahn, Horst-Günter. 2013. Poster session presented at E-MRS 2013 SPRING MEETING, Strasbourg, France.

- **In-flow formation of parallel PTDCI nano fibres.** Radziwon, Michał Jędrzej; Gazal, Aghiad; Rubahn, Horst-Günter; Hoyland, James. 2012. LancerIngen af årbog 2012 : forsknIng for enhver , Sønderborg, Denmark.
- **Oil contamination photoacoustic sensor system.** Radziwon, Michał Jędrzej; Albu, Mihaela; Duggen, Lars; Willatzen, Morten; Zwiig, Thomas; Rubahn, Horst-Günter. 2011. Poster session presented at The 19 th. International Conference on Advanced Laser Technologies, Golden Sands, Bulgaria.
- **Nanostructured Organic Solar Cells.** Radziwon, Michał Jędrzej; Rubahn, Horst-Günter; Madsen, Morten. 2011. Poster session presented at årbog forsknIng for enhver, Sønderborg, Denmark.
- **Efficiency enhancement in organic solar cells by controlled nanostructuring.** Radziwon, Michał Jędrzej; Oliveira Hansen, Roana Melina de ; Madsen, Morten; Rubahn, Horst-Günter. 2011. Poster session presented at DOPS Årsmøde 2011, Aarhus, Denmark.
- **Detection of n-heptane by photoacoustic spectroscopy using a 1725 nm DFB laser diode.** Radziwon, Michał Jędrzej; Albu, Mihaela; Frese, Ralf; Lopes, Natasha; Rubahn, Horst-Günter. 2011. Poster session presented at The 18th International Conference on Advanced Laser Technologies, Egmond aan Zee, Netherlands.
- **Lab-On-Chip Flow Cytometry.** Radziwon, Michał Jędrzej; Hoyland, James; Kunstmann-Olsen, Casper ; Rubahn, Horst-Günter. 2010. Poster session presented at Advanced Materials and Technologies, Palanga, Lithuania.

Authorship Agreement

This authorship agreement concerns the published research work conducted by PhD student Michal Radziwon.


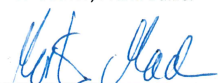
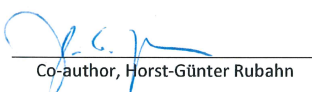
The research work includes the following article:

Growth of α -sexithiophene nanostructures on C60 thin film layers

In accordance with the criteria put forward at the Vancouver Convention for authorship (www.icmje.org), the undersigned Michal Radziwon hereby confirms that he as the first author is responsible for:

- Design the investigated structures
- Fabrication the investigated samples
- Together with M.Madsen: characterization of the samples with AFM
- Characterization of the samples with epifluorescence microscopy
- Together with R.Resel: X-Ray diffractometry
- Interpretation of the presented data
- The initial drafting (all sections)
- A substantial contribution of the intellectual content, and the finalization of the version to be published.

Similarly, the undersigned Frank Balzer, Roland Resel, Morten Madsen and Horst-Günter Rubahn, confirm that they have contributed quantitatively to the conception and design, the critical revision, the interpretation of experimental evidence, and the final approval of the version to be published.


First author, Michal Radziwon
Co-author, Frank Balzer
Co-author, Roland Resel
Co-author, Morten Madsen
Co-author, Horst-Günter Rubahn

Authorship Agreement

This authorship agreement concerns the published research work conducted by PhD student Michał Radziwon.

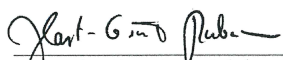
The research work includes the following article:

Crystallites of α -sexithiophene in bilayer small molecule organic solar cells double efficiency.

In accordance with the criteria put forward at the Vancouver Convention for authorship (www.icmje.org), the undersigned Michał Radziwon hereby confirms that he as the first author is responsible for:

- Design the investigated structures
- Fabrication of the investigated devices
- Characterization of the devices with epifluorescence microscopy
- Characterization of the devices with photo-electrometric setup
- Interpretation of the presented data
- The initial drafting (all sections)
- A substantial contribution of the intellectual content, and the finalization of the version to be published.

Similarly, the undersigned Morten Madsen and Horst-Günter Rubahn, confirm that they have contributed quantitatively to the conception and design, the critical revision, the interpretation of experimental evidence, and the final approval of the version to be published.


First author, Michał Radziwon
Co-author, Morten Madsen
Co-author, Horst-Günter Rubahn

Athorship Agreement

This authorship agreement concerns the published research work conducted by PhD student Michał Radziwon.

The research work includes the following article:

Nanotag luminescent fingerprint anti-counterfeiting technology

In accordance with the criteria put forward at the Vancouver Convention for authorship (www.icmje.org), the undersigned Michał Radziwon hereby confirms that he, as co-author is responsible for:

- Design of image processing routines
- Software implementation of image processing routines
- Cryptography strength analysis
- Interpretation of the presented data
- The initial drafting (all sections)
- A substantial contribution of the intellectual content, and the finalization of the version to be published.

Similarly, the undersigned Stefan Johansen, Luciana Tavares, and Horst-Günter Rubahn, confirm that they have contributed quantitatively to the conception and design, the critical revision, the interpretation of experimental evidence, and the final approval of the version to be published.



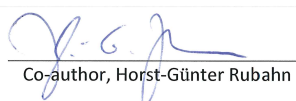
First author, Stefan Johansen



Co-author, Radziwon Michał



Co-author, Luciana Tavares



Co-author, Horst-Günter Rubahn

Athorship Agreement

This authorship agreement concerns the published research work conducted by PhD student Michał Radziwon.

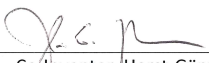
The research work includes the following patent application:

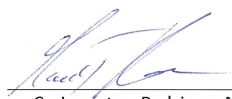
Nano-tags with luminescent fingerprints

In accordance with the criteria put forward at the Vancouver Convention for authorship (www.icmje.org), the undersigned Michał Radziwon hereby confirms that he, as co-inventor is responsible for:

- Design of image processing routines
- Software implementation of image processing routines
- Cryptography strength analysis
- Interpretation of the presented data
- A substantial contribution of the intellectual content, and the finalization of the version to be published.

Similarly, the undersigned Stefan Johansen, and Horst-Günter Rubahn, confirm that they have contributed quantitatively to the conception and design, the critical revision, the interpretation of experimental evidence, and the final approval of the version to be published.


Co-Inventor, Horst-Günter Rubahn


Co-Inventor, Radziwon Michał


Co-Inventor, Stefan Johansen

Manuscripts of submitted publications

Bibliography

- [1] S. Moosavian, N. Rahim, J. Selvaraj, and K. Solangi, “Energy policy to promote photovoltaic generation,” *Renewable and Sustainable Energy Reviews*, vol. 25, pp. 44–58, 2013.
- [2] W. Hoffmann, “Pv solar electricity industry: Market growth and perspective,” *Solar energy materials and solar cells*, vol. 90, no. 18, pp. 3285–3311, 2006.
- [3] V. Parra, T. Carballo, D. Cancillo, J. Bullon, J. Miguez, R. Ordas, B. Moralejo, O. Martinez, and J. Jimenez, “Trends in crystalline silicon growth for low cost and efficient photovoltaic cells,” in *Electron Devices (CDE), 2013 Spanish Conference on*. IEEE, 2013, pp. 305–308.
- [4] H.-T. Pao and C.-M. Tsai, “Co₂ emissions, energy consumption and economic growth in bric countries,” *Energy Policy*, vol. 38, no. 12, pp. 7850–7860, 2010.
- [5] P. Crompton and Y. Wu, “Energy consumption in china: past trends and future directions,” *Energy Economics*, vol. 27, no. 1, pp. 195–208, 2005.
- [6] P. Meakin, “Energy transitions in the early 21st century,” *Journal of Sustainable Energy Engineering*, vol. 1, no. 1, pp. 3–29, 2013.
- [7] G. M. Crawley, *The World Scientific Handbook of Energy*, 2013.
- [8] C. Green, S. Baksi, and M. Dilmaghani, “Challenges to a climate stabilizing energy future,” *Energy Policy*, vol. 35, no. 1, pp. 616–626, 2007.
- [9] U. E. U. E. P. Agency), “Inventory of us greenhouse gas emissions and sinks: 1990-2009,” 2011.

- [10] M. I. Hoffert, K. Caldeira, A. K. Jain, E. F. Haites, L. D. Harvey, S. D. Potter, M. E. Schlesinger, S. H. Schneider, R. G. Watts, T. M. Wigley *et al.*, “Energy implications of future stabilization of atmospheric co2 content,” *Nature*, vol. 395, no. 6705, pp. 881–884, 1998.
- [11] P. Tans, “Noaa,” *ESRL report www.esrl.noaa.gov/gmd/cgg/trends*, 2013.
- [12] C. Winneker, “World’s solar photovoltaic capacity passes 100-gigawatt landmark after strong year,” EPIA, <http://www.epia.org>, press release, February 2013.
- [13] N. Espinosa, M. Hösel, D. Angmo, and F. C. Krebs, “Solar cells with one-day energy payback for the factories of the future,” *Energy & Environmental Science*, vol. 5, no. 1, pp. 5117–5132, 2012.
- [14] Heliatek. (2013) Heliatek consolidates its technology leadership by establishing a new world record for organic solar technology with a cell efficiency of 12%
http://www.heliatek.com/newscenter/latest_news/
- [15] M. Scharber and N. Sariciftci, “Efficiency of bulk-heterojunction organic solar cells,” *Progress in Polymer Science*, 2013.
- [16] F. Krebs, “Polymer photovoltaics a practical approach,” 2008.
- [17] M. Riede, T. Mueller, W. Tress, R. Schueppel, and K. Leo, “Small-molecule solar cells - status and perspectives,” *Nanotechnology*, vol. 19, no. 42, p. 424001, 2008.
- [18] S. Abermann, “Non-vacuum processed next generation thin film photovoltaics: Towards marketable efficiency and production of czts based solar cells,” *Solar Energy*, vol. 94, pp. 37–70, 2013.
- [19] M. Madsen, J. Kjelstrup-Hansen, and H.-G. Rubahn, “The surface microstructure controlled growth of organic nanofibres,” *Nanotechnology*, vol. 20, no. 11, p. 115601, 2009.
- [20] L. Kankate, F. Balzer, H. Niehus, and H.-G. Rubahn, “Organic nanofibers from thiophene oligomers,” *Thin Solid Films*, vol. 518, no. 1, pp. 130–137, 2009.

- [21] F. Balzer, M. Schiek, H. Rubahn, K. Al-Shamery, and A. Lutzen, "Surface bound organic nanowires," *Journal of Vacuum Science & Technology B: Microelectronics and Nanometer Structures*, vol. 26, no. 4, pp. 1619–1623, 2008.
- [22] F. Balzer, L. Kankate, H. Niehus, R. Frese, C. Maibohm, and H.-G. Rubahn, "Tailoring the growth of p-6p nanofibres using ultrathin au layers: an organic–metal–dielectric model system," *Nanotechnology*, vol. 17, no. 4, p. 984, 2006.
- [23] F. Balzer and H.-G. Rubahn, "Dipole-assisted self-assembly of light-emitting< equation> p</equation>-np needles on mica," *Applied Physics Letters*, vol. 79, no. 23, pp. 3860–3862, 2001.
- [24] K. H. Al-Shamery, H.-G. Rubahn, and H. Sitter, *Organic nanostructures for next generation devices*. Springer, 2008, vol. 101.
- [25] A.-E. Becquerel, "Mémoire sur les effets électriques produits sous l'influence des rayons solaires," *Comptes Rendus*, vol. 9, no. 567, p. 1839, 1839.
- [26] A. Einstein, "Über einen die erzeugung und verwandlung des lichtes betreffenden heuristischen gesichtspunkt," *Annalen der Physik*, vol. 322, no. 6, pp. 132–148, 1905.
- [27] Sharp develops concentrator solar cell with world's highest conversion efficiency of 44.4<http://sharp-world.com/corporate/news/130614.html>
- [28] D. Wöhrle and D. Meissner, "Organic solar cells," *Advanced Materials*, vol. 3, no. 3, pp. 129–138, 1991.
- [29] T. Svanije, "Organic solar cells," 2009.
- [30] B. A. Gregg and M. C. Hanna, "Comparing organic to inorganic photovoltaic cells: Theory, experiment, and simulation," *Journal of Applied Physics*, vol. 93, no. 6, pp. 3605–3614, 2003.
- [31] H. Spanggaard and F. C. Krebs, "A brief history of the development of organic and polymeric photovoltaics," *Solar Energy Materials and Solar Cells*, vol. 83, no. 2, pp. 125–146, 2004.

-
- [32] C. Tang and A. Albrecht, "Photovoltaic effects of metal–chlorophyll-a–metal sandwich cells," *The Journal of Chemical Physics*, vol. 62, p. 2139, 1975.
- [33] S. R. Forrest, "Ultrathin organic films grown by organic molecular beam deposition and related techniques," *Growth*, vol. 3, no. 2, 1816.
- [34] M. Shtein, H. F. Gossenberger, J. B. Benziger, and S. R. Forrest, "Material transport regimes and mechanisms for growth of molecular organic thin films using low-pressure organic vapor phase deposition," *Journal of Applied Physics*, vol. 89, no. 2, pp. 1470–1476, 2001.
- [35] K. W. Chou, B. Yan, R. Li, E. Q. Li, K. Zhao, D. H. Anjum, S. Alvarez, R. Gasaway, A. Biocca, S. T. Thoroddsen *et al.*, "Solar cells: Spin-cast bulk heterojunction solar cells: A dynamical investigation (adv. mater. 13/2013)," *Advanced Materials*, vol. 25, no. 13, pp. 1805–1805, 2013.
- [36] D. Angmo, S. A. Gevorgyan, T. T. Larsen-Olsen, R. Søndergaard, M. Hösel, M. Jørgensen, R. Gupta, G. U. Kulkarni, and F. C. Krebs, "Scalability and stability of very thin, roll-to-roll processed, large area, indium-tin-oxide free polymer solar cell modules," *Organic Electronics*, 2013.
- [37] M. Hösel, R. R. Søndergaard, D. Angmo, and F. C. Krebs, "Comparison of fast roll-to-roll flexographic, inkjet, flatbed, and rotary screen printing of metal back electrodes for polymer solar cells," *Advanced Engineering Materials*, 2013.
- [38] S. E. Shaheen, R. Radspinner, N. Peyghambarian, and G. E. Jabbour, "Fabrication of bulk heterojunction plastic solar cells by screen printing," *Applied Physics Letters*, vol. 79, no. 18, pp. 2996–2998, 2001.
- [39] N. Sivaraman, R. Dhamodaran, I. Kaliappan, T. Srinivasan, P. V. Rao, and C. Mathews, "Solubility of c60 in organic solvents," *The Journal of Organic Chemistry*, vol. 57, no. 22, pp. 6077–6079, 1992.
- [40] R. Schinazi, R. Sijbesma, G. Srdanov, C. Hill, and F. Wudl, "Synthesis and virucidal activity of a water-soluble, configurationally stable, derivatized c60 fullerene." *Antimicrobial agents and chemotherapy*, vol. 37, no. 8, pp. 1707–1710, 1993.

- [41] S. Gunes, H. Neugebauer, and N. S. Sariciftci, "Conjugated polymer-based organic solar cells," *Chemical Reviews-Columbus*, vol. 107, no. 4, pp. 1324–1338, 2007.
- [42] H. Frohne, S. E. Shaheen, C. J. Brabec, D. C. Müller, N. S. Sariciftci, and K. Meerholz, "Influence of the anodic work function on the performance of organic solar cells," *ChemPhysChem*, vol. 3, no. 9, pp. 795–799, 2002.
- [43] A. Pizzirusso, M. Savini, L. Muccioli, and C. Zannoni, "An atomistic simulation of the liquid-crystalline phases of sexithiophene," *Journal of Materials Chemistry*, vol. 21, no. 1, pp. 125–133, 2011.
- [44] E. Da Como, M. A. Loi, M. Murgia, R. Zamboni, and M. Muccini, "J-aggregation in r-sexithiophene submonolayer films on silicon dioxide," *Phys. Lett*, vol. 80, p. 2254, 2002.
- [45] M. A. Loi, E. da Como, F. Dinelli, M. Murgia, R. Zamboni, F. Biscarini, and M. Muccini, "Supramolecular organization in ultra-thin films of α -sexithiophene on silicon dioxide," *Nature Materials*, vol. 4, no. 1, pp. 81–85, 2004.
- [46] G. Hlawacek, P. Puschnig, P. Frank, A. Winkler, C. Ambrosch-Draxl, and C. Teichert, "Characterization of step-edge barriers in organic thin-film growth," *Science*, vol. 321, no. 5885, pp. 108–111, 2008.
- [47] G. Koller, S. Berkebile, J. R. Krenn, F. P. Netzer, M. Oehzelt, T. Haber, R. Resel, and M. G. Ramsey, "Heteroepitaxy of organic-organic nanostructures," *Nano letters*, vol. 6, no. 6, pp. 1207–1212, 2006.
- [48] G. Koller, R. Blyth, S. Sardar, F. Netzer, and M. Ramsey, "Growth of ordered bithiophene layers on the p (2 \times 1) o reconstructed cu (110) surface," *Surface science*, vol. 536, no. 1, pp. 155–165, 2003.
- [49] G. Horowitz, B. Bachet, A. Yassar, P. Lang, F. Demanze, J.-L. Fave, and F. Garnier, "Growth and characterization of sexithiophene single crystals," *Chemistry of materials*, vol. 7, no. 7, pp. 1337–1341, 1995.

-
- [50] W. Porzio, S. Destri, M. Mascherpa, S. Rossini, and S. Brückner, “Structural aspects of oligothiényls from x-ray powder diffraction data,” *Synthetic metals*, vol. 55, no. 1, pp. 408–413, 1993.
- [51] C. Simbrunner, “Epitaxial growth of sexi-thiophene and para-hexaphenyl and its implications for the fabrication of self-assembled lasing nano-fibres,” *Semiconductor Science and Technology*, vol. 28, no. 5, p. 053001, 2013.
- [52] P. Hermet, J.-L. Bantignies, A. Rahmani, J.-L. Sauvajol, and M. Johnson, “Polymorphism of crystalline α -quaterthiophene and α -sexithiophene: ab initio analysis and comparison with inelastic neutron scattering response,” *The Journal of Physical Chemistry A*, vol. 109, no. 18, pp. 4202–4207, 2005.
- [53] R. E. Smalley, H. Kroto, and J. Heath, “C60 buckminsterfullerène,” *Nature*, vol. 318, no. 6042, pp. 162–163, 1985.
- [54] N. Sariciftci, L. Smilowitz, A. Heeger, F. Wudl *et al.*, “Photoinduced electron transfer from a conducting polymer to buckminsterfullerene,” *Science*, vol. 258, no. 5087, pp. 1474–1476, 1992.
- [55] C. Brabec, N. Sariciftci, J. Hummelen *et al.*, “Plastic solar cells,” *Advanced Functional Materials*, vol. 11, no. 1, pp. 15–26, 2001.
- [56] B. P. Rand, J. Genoe, P. Heremans, and J. Poortmans, “Solar cells utilizing small molecular weight organic semiconductors,” *Progress in Photovoltaics: Research and Applications*, vol. 15, no. 8, pp. 659–676, 2007.
- [57] P. Heremans, D. Cheyns, and B. P. Rand, “Strategies for increasing the efficiency of heterojunction organic solar cells: material selection and device architecture,” *Accounts of chemical research*, vol. 42, no. 11, pp. 1740–1747, 2009.
- [58] F. Guo, X. Zhu, K. Forberich, J. Krantz, T. Stubhan, M. Salinas, M. Halik, S. Spallek, B. Butz, E. Spiecker *et al.*, “Ito-free and fully solution-processed semi-transparent organic solar cells with high fill factors,” *Advanced Energy Materials*, 2013.

- [59] H. Schmidt, H. Flügge, T. Winkler, T. Bülow, T. Riedl, and W. Kowalsky, “Efficient semitransparent inverted organic solar cells with indium tin oxide top electrode,” *Applied Physics Letters*, vol. 94, p. 243302, 2009.
- [60] A. Seemann, H.-J. Egelhaaf, C. J. Brabec, and J. A. Hauch, “Influence of oxygen on semi-transparent organic solar cells with gas permeable electrodes,” *Organic Electronics*, vol. 10, no. 8, pp. 1424–1428, 2009.
- [61] E. Centurioni, “Generalized matrix method for calculation of internal light energy flux in mixed coherent and incoherent multilayers,” *Applied optics*, vol. 44, no. 35, pp. 7532–7539, 2005.
- [62] B. Verreet, P. E. Malinowski, B. Niesen, D. Cheyns, P. Heremans, A. Stesmans, and B. P. Rand, “Improved cathode buffer layer to decrease exciton recombination in organic planar heterojunction solar cells,” *Applied Physics Letters*, vol. 102, no. 4, pp. 043 301–043 301, 2013.
- [63] H. Woo Lee, J. Young Oh, T. Il Lee, W. Soon Jang, Y. Bum Yoo, S. Sang Chae, J. Ho Park, J. Min Myoung, K. Moon Song, and H. Koo Baik, “Highly efficient inverted polymer solar cells with reduced graphene-oxide-zinc-oxide nanocomposites buffer layer,” *Applied Physics Letters*, vol. 102, no. 19, pp. 193 903–193 903, 2013.
- [64] H. Gommans, B. Verreet, B. Rand, R. Muller, J. Poortmans, P. Heremans, and J. Genoe, “On the role of bathocuproine in organic photovoltaic cells,” *Advanced Functional Materials*, vol. 18, no. 22, pp. 3686–3691, 2008.
- [65] T. Stubinger and W. Brütting, “Exciton diffusion and optical interference in organic donor–acceptor photovoltaic cells,” *Journal of Applied Physics*, vol. 90, no. 7, pp. 3632–3641, 2001.
- [66] M. Muntwiler, Q. Yang, W. A. Tisdale, and X.-Y. Zhu, “Coulomb barrier for charge separation at an organic semiconductor interface,” *Physical review letters*, vol. 101, no. 19, p. 196403, 2008.
- [67] C. W. Tang, “Two-layer organic photovoltaic cell,” *Applied Physics Letters*, vol. 48, p. 183, 1986.

-
- [68] Y. Wang and A. Suna, "Fullerenes in photoconductive polymers. charge generation and charge transport," *The Journal of Physical Chemistry B*, vol. 101, no. 29, pp. 5627–5638, 1997.
- [69] H. Ohkita, S. Cook, Y. Astuti, W. Duffy, S. Tierney, W. Zhang, M. Heeney, I. McCulloch, J. Nelson, D. D. Bradley *et al.*, "Charge carrier formation in polythiophene/fullerene blend films studied by transient absorption spectroscopy," *Journal of the American Chemical Society*, vol. 130, no. 10, pp. 3030–3042, 2008.
- [70] P. W. Blom, V. D. Mihailetschi, L. J. A. Koster, and D. E. Markov, "Device physics of polymer: fullerene bulk heterojunction solar cells," *Advanced Materials*, vol. 19, no. 12, pp. 1551–1566, 2007.
- [71] J. Barker, C. Ramsdale, and N. Greenham, "Modeling the current-voltage characteristics of bilayer polymer photovoltaic devices," *Physical Review B*, vol. 67, no. 7, p. 075205, 2003.
- [72] D. Cheyns, J. Poortmans, P. Heremans, C. Deibel, S. Verlaak, B. Rand, and J. Genoe, "Analytical model for the open-circuit voltage and its associated resistance in organic planar heterojunction solar cells," *Physical Review B*, vol. 77, no. 16, p. 165332, 2008.
- [73] V. Coropceanu, J. Cornil, D. A. da Silva Filho, Y. Olivier, R. Silbey, J.-L. Brédas *et al.*, "Charge transport in organic semiconductors," *Chemical Reviews-Columbus*, vol. 107, no. 4, pp. 926–952, 2007.
- [74] V. D. Mihailetschi, H. Xie, B. de Boer, L. J. A. Koster, and P. W. Blom, "Charge transport and photocurrent generation in poly (3-hexylthiophene): methanofullerene bulk-heterojunction solar cells," *Advanced Functional Materials*, vol. 16, no. 5, pp. 699–708, 2006.
- [75] P. Peumans, A. Yakimov, and S. R. Forrest, "Small molecular weight organic thin-film photodetectors and solar cells," *Journal of Applied Physics*, vol. 93, no. 7, pp. 3693–3723, 2003.
- [76] M. Glatthaar, M. Riede, N. Keegan, K. Sylvester-Hvid, B. Zimmermann, M. Niggemann, A. Hinsch, and A. Gombert, "Efficiency limiting factors of organic

- bulk heterojunction solar cells identified by electrical impedance spectroscopy,” *Solar energy materials and solar cells*, vol. 91, no. 5, pp. 390–393, 2007.
- [77] M. Vogel, S. Doka, C. Breyer, M. C. Lux-Steiner, and K. Fostiropoulos, “On the function of a bathocuproine buffer layer in organic photovoltaic cells,” *Applied physics letters*, vol. 89, no. 16, pp. 163 501–163 501, 2006.
- [78] S. Yoo, W. J. Potscavage Jr, B. Domercq, S.-H. Han, T.-D. Li, S. C. Jones, R. Szoszkiewicz, D. Levi, E. Riedo, S. R. Marder *et al.*, “Analysis of improved photovoltaic properties of pentacene/c< sub>60</sub> organic solar cells: Effects of exciton blocking layer thickness and thermal annealing,” *Solid-State Electronics*, vol. 51, no. 10, pp. 1367–1375, 2007.
- [79] P. Peumans and S. R. Forrest, “Separation of geminate charge-pairs at donor–acceptor interfaces in disordered solids,” *Chemical Physics Letters*, vol. 398, no. 1, pp. 27–31, 2004.
- [80] W. J. Beek, M. M. Wienk, and R. A. Janssen, “Efficient hybrid solar cells from zinc oxide nanoparticles and a conjugated polymer,” *Advanced Materials*, vol. 16, no. 12, pp. 1009–1013, 2004.
- [81] M. Grobosch and M. Knupfer, “Electronic properties of organic semiconductor/electrode interfaces: The influence of contact contaminations on the interface energetic,” *Open Applied Physics Journal*, vol. 4, pp. 8–18, 2011.
- [82] K. Norrman and F. C. Krebs, “Lifetimes of organic photovoltaics: Using tof-sims and< sup> 18</sup> o< sub> 2</sub> isotopic labelling to characterise chemical degradation mechanisms,” *Solar energy materials and solar cells*, vol. 90, no. 2, pp. 213–227, 2006.
- [83] T. Ishida, H. Kobayashi, and Y. Nakato, “Structures and properties of electron-beam-evaporated indium tin oxide films as studied by x-ray photoelectron spectroscopy and work-function measurements,” *Journal of applied physics*, vol. 73, no. 9, pp. 4344–4350, 1993.
- [84] G. Chamberlain, “Organic solar cells: a review,” *Solar Cells*, vol. 8, no. 1, pp. 47–83, 1983.

-
- [85] B. O'regan and M. Grfitzeli, "A low-cost, high-efficiency solar cell based on dye-sensitized," *nature*, vol. 353, p. 24, 1991.
- [86] I. D. Parker, "Carrier tunneling and device characteristics in polymer light-emitting diodes," *Journal of Applied Physics*, vol. 75, p. 1656, 1994.
- [87] A. K. Ghosh, D. L. Morel, T. Feng, R. F. Shaw, and C. A. Rowe, "Photovoltaic and rectification properties of al/mg phthalocyanine/ag schottky-barrier cells," *Journal of Applied Physics*, vol. 45, no. 1, pp. 230–236, 1974.
- [88] D. Morel, A. Ghosh, T. Feng, E. Stogryn, P. Purwin, R. Shaw, and C. Fishman, "High-efficiency organic solar cells," *Applied Physics Letters*, vol. 32, no. 8, pp. 495–497, 1978.
- [89] I. Yahia, H. Hafez, F. Yakuphanoglu, B. Senkal, and M. Mottaleb, "Photovoltaic and impedance spectroscopy analysis of p–n like junction for dye sensitized solar cell," *Synthetic Metals*, vol. 161, no. 13, pp. 1299–1305, 2011.
- [90] J. Halls, K. Pichler, R. Friend, S. Moratti, and A. Holmes, "Exciton diffusion and dissociation in a poly (p-phenylenevinylene)/c 60 heterojunction photovoltaic cell," *Applied Physics Letters*, vol. 68, no. 22, pp. 3120–3122, 1996.
- [91] G. Yu, J. Gao, J. Hummelen, F. Wudl, and A. Heeger, "Polymer photovoltaic cells: enhanced efficiencies via a network of internal donor-acceptor heterojunctions," *SCIENCE-NEW YORK THEN WASHINGTON*-, pp. 1789–1790, 1995.
- [92] M. Hiramoto, H. Fujiwara, and M. Yokoyama, "Three-layered organic solar cell with a photoactive interlayer of codeposited pigments," *Applied physics letters*, vol. 58, no. 10, pp. 1062–1064, 1991.
- [93] R. M. de Oliveira Hansen, Y. Liu, M. Madsen, and H.-G. Rubahn, "Flexible organic solar cells including efficiency enhancing grating structures," *Nanotechnology*, vol. 24, no. 14, p. 145301, 2013.
- [94] D. Cheyns, K. Vasseur, C. Rolin, J. Genoe, J. Poortmans, and P. Heremans, "Nanoimprinted semiconducting polymer films with 50 nm features and their application to organic heterojunction solar cells," *Nanotechnology*, vol. 19, no. 42, p. 424016, 2008.

- [95] S.-S. Sun and L. R. Dalton, *Introduction to Organic Electronic and Optoelectronic Materials and Devices (Optical Science and Engineering Series)*. CRC Press, Inc., 2008.
- [96] H. Hoppea and N. Sariciftci, “Organic solar cells: An overview,” *J. Mater. Res*, vol. 19, no. 7, p. 1925, 2004.
- [97] J. Lee, S. Roth, and Y. Park, “Anisotropic field effect mobility in single crystal pentacene,” *Applied physics letters*, vol. 88, no. 25, pp. 252 106–252 106, 2006.
- [98] O. Pellegrino, M. Rei Vilar, G. Horowitz, and A. Botelho do Rego, “Oligothiophene films under electron irradiation: electron mobility and contact potentials,” *Materials Science and Engineering: C*, vol. 22, no. 2, pp. 367–372, 2002.
- [99] C. Simbrunner, G. Hernandez-Sosa, M. Oehzelt, T. Djuric, I. Salzmann, M. Brinkmann, G. Schwabegger, I. Watzinger, H. Sitter, and R. Resel, “Epitaxial growth of sexithiophene on mica surfaces,” *Physical Review B*, vol. 83, no. 11, p. 115443, 2011.
- [100] J. Mu, Z. Chen, and T. Luong, “X-ray diffraction investigations of well-ordered sexithiophene films deposited on flexible substrates,” *Journal of Materials Processing Technology*, vol. 209, no. 3, pp. 1491–1494, 2009.
- [101] J. Wittmann, C. Straupe, S. Meyer, B. Lotz, P. Lang, G. Horowitz, and F. Garnier, “Sexithiophene thin films epitaxially oriented on polytetrafluoroethylene substrates: Structure and morphology,” *Thin solid films*, vol. 303, no. 1, pp. 207–212, 1997.
- [102] A. Goszczak, “Improved solar cells by integration of crystalline organic nanostructures,” Master’s thesis, University of Southern Denmark, 2012.
- [103] C. Heiner, “Order and symmetries of sexithiophene within thin films studied by angle-resolved photoemission,” Ph.D. dissertation, Diplomarbeit, 2004.
- [104] K. Thilsing-Hansen, “Growth and integration of organic nanofibers in devices,” Ph.D. dissertation, Syddansk Universitet, 2010.

-
- [105] A. J. Mäkinen, J. P. Long, N. J. Watkins, and Z. H. Kafafi, "Sexithiophene adlayer growth on vicinal gold surfaces," *The Journal of Physical Chemistry B*, vol. 109, no. 12, pp. 5790–5795, 2005.
- [106] F. Spano, "Excitons in conjugated oligomer aggregates, films, and crystals," *Annu. Rev. Phys. Chem.*, vol. 57, pp. 217–243, 2006.
- [107] Z. Chen, S. Ikeda, and K. Saiki, "Sexithiophene films on cleaved kbr (100) towards well-ordered semiconducting films," *Materials Science and Engineering: B*, vol. 133, no. 1, pp. 195–199, 2006.
- [108] J. Ivanco, T. Haber, J. Krenn, F. Netzer, R. Resel, and M. Ramsey, "Sexithiophene films on ordered and disordered $\text{TiO}_2(110)$ surfaces: Electronic, structural and morphological properties," *Surface science*, vol. 601, no. 1, pp. 178–187, 2007.
- [109] K. Itaka, M. Yamashiro, J. Yamaguchi, M. Haemori, S. Yaginuma, Y. Matsumoto, M. Kondo, and H. Koinuma, "High-mobility c60 field-effect transistors fabricated on molecular-wetting controlled substrates," *Advanced Materials*, vol. 18, no. 13, pp. 1713–1716, 2006.
- [110] S. Veenstra, G. Malliaras, H. Brouwer, F. Esselink, V. Krasnikov, P. van Hutten, J. Wildeman, H. Jonkman, G. Sawatzky, and G. Hadziioannou, "Preparation of photovoltaic cells from sexithiophene-c 60 blends," in *Society of Photo-Optical Instrumentation Engineers (SPIE) Conference Series*, vol. 2852, 1996, pp. 277–285.
- [111] Y. Ge and J. Whitten, "Energy level alignment between sexithiophene and buckminsterfullerene films," *Chemical Physics Letters*, vol. 448, no. 1, pp. 65–69, 2007.
- [112] J. Sakai, T. Taima, and K. Saito, "Efficient oligothiophene: fullerene bulk heterojunction organic photovoltaic cells," *Organic Electronics*, vol. 9, no. 5, pp. 582–590, 2008.
- [113] S. Veenstra, G. Malliaras, H. Brouwer, F. Esselink, V. Krasnikov, P. Van Hutten, J. Wildeman, H. Jonkman, G. Sawatzky, and G. Hadziioannou, "Sexithiophene-

- c₆₀ blends as model systems for photovoltaic devices,” *Synthetic metals*, vol. 84, no. 1, pp. 971–972, 1997.
- [114] H. Zhang, W. Chen, L. Chen, H. Huang, X. Wang, J. Yuhara, and A. Wee, “C₆₀ molecular chains on α -sexithiophene nanostripes,” *Small*, vol. 3, no. 12, pp. 2015–2018, 2007.
- [115] J. Sakai, T. Taima, T. Yamanari, and K. Saito, “Annealing effect in the sexithiophene: C₇₀ small molecule bulk heterojunction organic photovoltaic cells,” *Solar Energy Materials and Solar Cells*, vol. 93, no. 6, pp. 1149–1153, 2009.
- [116] F. Lindholm, J. Fossum, and E. Burgess, “Application of the superposition principle to solar-cell analysis,” *Electron Devices, IEEE Transactions on*, vol. 26, no. 3, pp. 165–171, 1979.
- [117] M. Radziwon, M. Madsen, and H.-G. Rubahn, “Crystallites of a-sexithiophene in bilayer small molecule organic solar cells double efficiency,” *Renewable energy*, submitted.
- [118] K. Kawano, R. Pacios, D. Poplavskyy, J. Nelson, D. D. Bradley, and J. R. Durrant, “Degradation of organic solar cells due to air exposure,” *Solar Energy Materials and Solar Cells*, vol. 90, no. 20, pp. 3520–3530, 2006.
- [119] B. S. Pons, J. S. Mattson, L. O. Winstrom, and H. B. Mark Jr, “Application of deposited thin metal films as optically transparent electrodes for internal reflection spectrometric observation of electrode solution interfaces,” *Analytical Chemistry*, vol. 39, no. 6, pp. 685–688, 1967.
- [120] Y. H. Kim, C. Sachse, M. L. Machala, C. May, L. Müller-Meskamp, and K. Leo, “Highly conductive pedot: Pss electrode with optimized solvent and thermal post-treatment for ito-free organic solar cells,” *Advanced Functional Materials*, vol. 21, no. 6, pp. 1076–1081, 2011.
- [121] D. Wakizaka, T. Fushimi, H. Ohkita, and S. Ito, “Hole transport in conducting ultrathin films of pedot/pss prepared by layer-by-layer deposition technique,” *Polymer*, vol. 45, no. 25, pp. 8561–8565, 2004.

-
- [122] G. Dennler, C. Lungenschmied, H. Neugebauer, N. Sariciftci, M. Latreche, G. Czermuszkin, and M. Wertheimer, “A new encapsulation solution for flexible organic solar cells,” *Thin Solid Films*, vol. 511, pp. 349–353, 2006.
- [123] N. Kim, W. Potscavage, B. Domercq, B. Kippelen, and S. Graham, “A hybrid encapsulation method for organic electronics,” *Applied Physics Letters*, vol. 94, no. 16, pp. 163 308–163 308, 2009.
- [124] W. Potscavage, S. Yoo, B. Domercq, and B. Kippelen, “Encapsulation of pentacene/c organic solar cells with also deposited by atomic layer deposition,” *Applied physics letters*, vol. 90, p. 253511, 2007.
- [125] S. Sista, M.-H. Park, Z. Hong, Y. Wu, J. Hou, W. L. Kwan, G. Li, and Y. Yang, “Highly efficient tandem polymer photovoltaic cells,” *Advanced materials*, vol. 22, no. 3, pp. 380–383, 2010.
- [126] J. C. Costa, C. F. Lima, L. R. Gomes, B. Schroeder, and L. M. Santos, “Phase stability trend in linear α -polythiophene oligomers,” *The Journal of Physical Chemistry C*, vol. 115, no. 47, pp. 23 543–23 551, 2011.
- [127] C. Pan, M. Sampson, Y. Chai, R. Hauge, and J. Margrave, “Heats of sublimation from a polycrystalline mixture of carbon clusters (c60 and c70),” *The Journal of Physical Chemistry*, vol. 95, no. 8, pp. 2944–2946, 1991.
- [128] M. Sezgin *et al.*, “Survey over image thresholding techniques and quantitative performance evaluation,” *Journal of Electronic imaging*, vol. 13, no. 1, pp. 146–168, 2004.
- [129] H. Ewers, “Septin pairs, a complex choreography,” *The Journal of cell biology*, vol. 193, no. 6, pp. 959–961, 2011.
- [130] R. Rezakhaniha, A. Agianniotis, J. T. C. Schrauwen, A. Griffa, D. Sage, C. Bouten, F. van de Vosse, M. Unser, and N. Stergiopulos, “Experimental investigation of collagen waviness and orientation in the arterial adventitia using confocal laser scanning microscopy,” *Biomechanics and modeling in mechanobiology*, vol. 11, no. 3-4, pp. 461–473, 2012.

- [131] H. Sun, Z. Zhao, F. C. Spano, D. Beljonne, J. Cornil, Z. Shuai, and J.-L. Brédas, “Absorption and emission in quaterthienyl thin films,” *Advanced Materials*, vol. 15, no. 10, pp. 818–822, 2003.
- [132] A. Richter and J. Sturm, “Dielectric and optical properties of c 60 material studied by ellipsometry and quantitative ir and uv/vis spectroscopy,” *Applied Physics A: Materials Science & Processing*, vol. 61, no. 2, pp. 163–170, 1995.
- [133] M. Gobbi, F. Golmar, R. Llopis, F. Casanova, and L. E. Hueso, “Room-temperature spin transport in c60-based spin valves,” *Advanced Materials*, vol. 23, no. 14, pp. 1609–1613, 2011.
- [134] W. Krakow, N. Rivera, R. Roy, R. Ruoff, and J. Cuomo, “Epitaxial growth of c60 thin films on mica,” *J. Mater. Res*, vol. 7, no. 4, p. 785, 1992.
- [135] —, “The growth of crystalline vapor deposited carbon-60 thin films,” *Applied Physics A: Materials Science & Processing*, vol. 56, no. 3, pp. 185–192, 1993.
- [136] G. Horowitz, P. Valat, F. Garnier, F. Kouki, and V. Wintgens, “Photoinduced spontaneous and stimulated emission in sexithiophene single crystals,” *Optical Materials*, vol. 9, no. 1, pp. 46–52, 1998.
- [137] M. Muccini, E. Lunedei, C. Taliani, F. Gamier, and H. Baessler, “Defect state emission in α -sexithiophene single crystal,” *Synthetic metals*, vol. 84, no. 1, pp. 599–600, 1997.
- [138] S. J. Bonafede and M. D. Ward, “Selective nucleation and growth of an organic polymorph by ledge-directed epitaxy on a molecular crystal substrate,” *Journal of the American Chemical Society*, vol. 117, no. 30, pp. 7853–7861, 1995.
- [139] G. Horowitz, M. E. Hajlaoui, and R. Hajlaoui, “Temperature and gate voltage dependence of hole mobility in polycrystalline oligothiophene thin film transistors,” *Journal of Applied Physics*, vol. 87, no. 9, pp. 4456–4463, 2000.
- [140] T. Itoh, S. Nitta, and S. Nonomura, “X-ray diffraction patterns of c60 films by the thin film method and the intercalation of o2,” *Applied surface science*, vol. 113, pp. 282–285, 1997.

- [141] Y. Kim, A. M. Ballantyne, J. Nelson, and D. D. Bradley, “Effects of thickness and thermal annealing of the PEDOT:PSS layer on the performance of polymer solar cells,” *Organic Electronics*, vol. 10, no. 1, pp. 205–209, 2009.
- [142] C. J. Brabec, A. Cravino, D. Meissner, N. S. Sariciftci, T. Fromherz, M. T. Rispens, L. Sanchez, and J. C. Hummelen, “Origin of the open circuit voltage of plastic solar cells,” *Advanced Functional Materials*, vol. 11, no. 5, pp. 374–380, 2001.
- [143] B. Ecker, H. Egelhaaf, R. Steim, J. Parisi, and E. von Hauff, “Understanding s-shaped current-voltage characteristics in organic solar cells containing a TiO₂ interlayer with impedance spectroscopy and equivalent circuit analysis,” 2012.
- [144] L. Tavares, J. Kjelstrup-Hansen, H.-G. Rubahn, and H. Sturm, “Reduced bleaching in organic nanofibers by bilayer polymer/oxide coating,” *Journal of Applied Physics*, vol. 107, no. 10, pp. 103 521–103 521, 2010.